Noisy Spectra of Dust particles: What, where and how?

A Dissertation
Presented in Partial Fulfillment of the Requirements for the

Degree of Doctor of Philosophy

with a

Major in Physics

in the

College of Graduate Studies

University of Idaho

by

Himanshi Sharma

Major Professor
Matthew M. Hedman, Ph.D.

Committee
Jason Barnes, Ph.D.
Gwendolyn D. Barnes, Ph.D.
Erika Rader, Ph.D.

Department Chair
John Hiller, Ph.D.

December 2023

Abstract

Studying the spectra of dust in different planetary environments is important as it provides valuable insights into the processes occurring in various astronomical environments. This knowledge not only advances our understanding of other worlds but also has practical implications for future space missions and our broader understanding of planetary systems. Spectral data often contains noise and one of the challenges is to reduce this noise and improve the signal-to-noise ratio in order to extract reliable information from the data. We explore and apply several background removal and noise reduction techniques in this study. These techniques are applied on the spectral data of two different dust populations, one on the Earth's Moon and the second emerging from the south pole of Saturn's moon Enceladus. First, the dust population on Earth's Moon is constrained by obtaining an upper limit on the number density of dust particles at the Moon's surface. Lunar dust, due to its abrasive properties, poses a risk to astronomical observations and the dust densities limits obtained in this analysis will help plan safer and more reliable future missions to the Moon. These constraints on dust population in the terminator region of the Moon can also be used to constrain the Moon's near-surface environment. Next, we study the properties of ice-grain particles in Enceladus's south polar plume by deriving typical launch velocities and size distribution parameters for the particles present in the plume. These plume particle properties provide new insights into vent dynamics, suggesting that particle-particle interactions are more relevant than previously expected by established models. We also develop a new Machine Learning algorithm that allows robust constraints on particle size distribution parameters to be extracted from noisy spectral data. These tools reveal that the plume's particle properties can vary in complex ways over multiple timescales. These findings should constrain the physical processes underlying Enceladus' plume particle dynamics.

Acknowledgements

I want to start by thanking my advisor Dr. Hedman for his constant guidance and support. I got into this PhD program and continued because of my conversations with Dr. Hedman. His patience and invaluable feedback drove this research and brought it to this stage of completion. Every interaction with my advisor left me feeling confident and driven, filled with the thought: "I can do this". I am immensely grateful to Dr. Hedman for giving me this opportunity and believing in me. I would also like to thank my committee members: Dr. Jason Barnes, Dr. Gwen Barnes and Dr. Erika Rader for the trust they placed in me by joining this committee in the first place. I appreciate your time, feedback and suggestions that helped me improve my work. I am grateful to all the teachers in the Physics department at University of Idaho who gave me the best learning experience through their classes. I am especially grateful to my co-authors and reviewers for their inputs and recommendations. The papers only got better with their feedback.

I could not have continued this journey without the help and support from Dr. Rajani who was there for me on every step of the way. I am also grateful to my colleagues and friends, Danielle Kreyche, Dr. Steven Kreyche, Dr. Sanjoy Saha, Dr. Joseph A'Hearn, Michael Heslar, Samiksha Gupta, and Dr. Himanshi Singh for their feedback and moral support. Thank you keeping my spirits high.

Lastly, I want to thank my family who believed in me, most importantly my mom, dad and brother. Their support and encouragement kept me motivated.

Dedication

I dedicate this work to my family, who believed in me, most importantly my mom, dad and brother. Their support and encouragement kept me going.

Table of Contents

List of Tables

List of Figures

Statement of Contribution

This work contains multi-authored papers in Chapter 2, 3, and 4. I am the corresponding author for these chapters. Matthew M. Hedman, PhD. is the second author of these papers. This work was done under the guidance of Dr. Hedman.

In Chapter 2, a combination of IDL, C++ and Python code is used. Dr. Hedman gathered the data from public databases, and wrote IDL code to digest these data into a standard format and compute relevant geometrical parameters. I wrote the C++ and Python code to clean, average and model the data. Co-authors A. Colaprete, A. M. Cook and D. H. Wooden provided comments to improve the content during the publication process.

For Chapter 3 and 4, the same data set is used to obtain two different properties of the plume particles. Dr. Hedman gathered the calibrated data from appropriate databases, and wrote IDL code to re-project the data onto a cartesian co-ordinate system. He provided the IDL save files that contained measurements unique to each observation. I wrote the Python code to clean and filter the data. Co-author Sanaz Vahidinia had multiple discussions to discuss the progress of the work and provided helpful suggestions.

In Chapter 3, I performed the data analysis to achieve altitude profiles and concluded the velocity distribution of plume particles. In Chapter 4, I wrote the Python code and designed the Machine Learning algorithm to compare observed and theoretical data. I used a Python package called PyMieScatt to calculate theoretical spectrum.

Dr. Matthew Hedman, Dr. Jason Barnes, Dr. Gwendolyn Barnes and Dr. Erika Rader provided suggestion for changes and additions to the introduction and conclusion of this work.

CHAPTER 1

Introduction

A spectrum is defined as the amount of light reflected or emitted over a range of wavelengths measured by a spectrographic equipment. The electromagnetic spectrum ranges from the very short wavelengths of gamma rays ($< 10^{-6}$ nm) to the long wavelengths of radio waves ($> 10^{6}$ nm). Studying spectra can help understand how an object produces, emits, and absorbs light; of what it is composed; and its physical properties. A spectrometer can be found on many spacecraft since the measurement of light can be highly valuable in further understanding of our universe. More specifically, UV-Vis spectroscopy uses the ultraviolet and visible regions of the electromagnetic spectrum in the wavelength range of 0.1 - 0.7 μm, and infrared spectroscopy uses the infrared part of the spectrum in the wavelength range of around 0.7 - 100 μm. In practice, there are multiple ways to obtain spectral data. For example, hyperspectral imaging combines imaging and spectroscopy to create spectral data for each pixel in an image, enabling spectral variations to be mapped across a surface.

Spectral data are highly relevant to planetary science and are a crucial tool for understanding the composition, properties, and processes occurring on planets and other celestial bodies. Spectroscopy allows us the study of the composition of planetary surface and atmospheres, by identifying the presence of specific elements, minerals, and compounds. This compositional information can provide insights into the potential habitability of planets by revealing the spectroscopic signatures of organic molecules, water, and other substances that could indicate conditions conducive to life (Hansen *et al.*, 2011; Thomas-Keprta *et al.*, 2014; Raponi *et al.*, 2021). Geological mapping using spectral data is essential for characterizing terrain and geological features like impact craters, volcanoes, and mountain ranges (Solomonidou *et al.*, 2010; Wright *et al.*, 2013). Information gathered using spectroscopy can also be used to characterize exoplanets, and understand their history and evolution (Kaltenegger *et al.*, 2010; Quanz *et al.*, 2021). Additionally,

spectral data are used to study the atmospheres of planets, revealing information about temperature, pressure, chemical composition, and atmospheric dynamics (von Paris *et al.*, 2013; Tinetti *et al.*, 2013). In this dissertation, spectral data are used for studying the dust above our own Moon and Saturn's moon Enceladus.

Studying the spectra of dust particles can provide insightful information about various astronomical environments. Dust particles ranging from nanometer to micrometer size have been observed in different parts of space, from protoplanetary discs to planetary atmospheres, and can be used to characterize their environments (Blum *et al.*, 2008). Similarly dust particles can be found around the surfaces of solid planetary bodies and in Saturn's rings. These dust particles exhibit interesting morphological, mechanical, and optical properties. Systematic investigations of these dusty environments can help understand the cosmic material cycle, the formation of the first solid bodies in the solar system, the evolution of planetary atmospheres, and the physical properties of solid bodies. In addition, constraints on the dust population and their physical properties (such as velocity and size) can help plan safer and more efficient future missions into space (Blum *et al.*, 2008).

The light-scattering properties of small particles can be modeled in a variety of ways. These models can divided into three domains based on a dimensionless size parameter, x, which is defined as:

$$x = \frac{\pi d}{\lambda} \tag{1.1}$$

where πd is the circumference of a particle and λ is the wavelength of incident radiation. Based on the value of x, these domains are: Rayleigh scattering, which is valid when $x << 1$ (the particle is small relative to the wavelength of light); Mie scattering, which is valid when $x \approx 1$ (the particle is about the same size as the wavelength of light); Geometric scattering, which is valid when $x >> 1$ (the particle is larger than the wavelength of light).

Figure 1.1 shows the scattering efficiency as a function of scattering angle for three different values of x across a range of scattering angles (the angle between the incident and scattered light ray) using polar co-ordinates on left side and a line plot

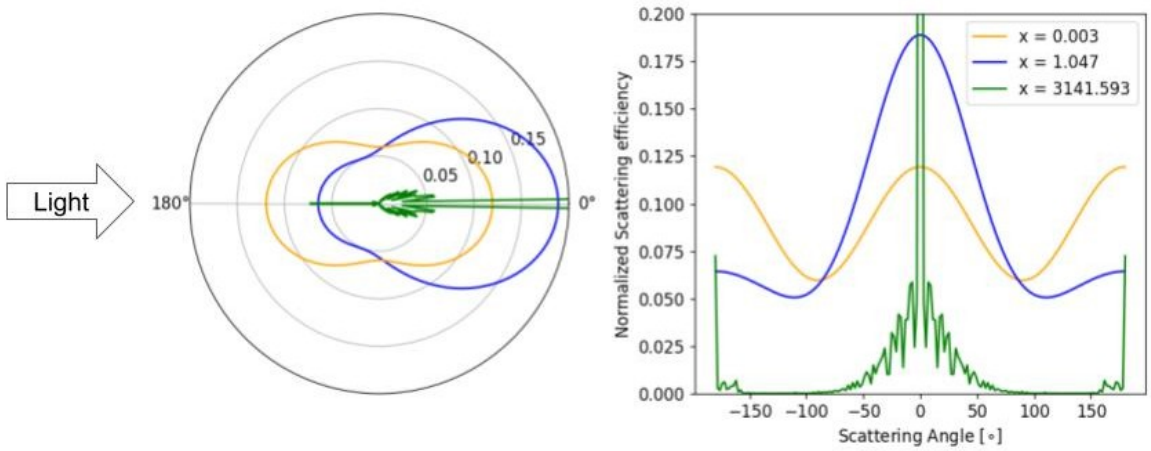

FIGURE 1.1: This figure shows the relationship between scattering efficiency and scattering angle (θ) in polar co-ordinates on the left and as a line plot on the right for a spherical particle of complex refractive index m = 1.5 - 1j (note the negative sign is convention for the miepython code). These values were obtained using Mie scattering theory code embedded in the python package "miepython". The polar co-ordinates are such that the particle is at the center of the circle and light is incident from the left. The scattering efficiency for the green curve is scaled (divided by 10) to view the curve clearly. For small particles with $x << 1$ (shown in orange) light is reflected equally in the forward and backward directions. For particle sizes roughly equivalent to the wavelength of incident light i.e., $x \approx 1$ (shown in blue) scattering is majorly in the forward direction. For large particles with $x >> 1$ (shown in green), the scattering is much narrower and concentrated in the forward direction.

on the right side. These plots were created using the python package "miepython"[1], and the curves are normalized so that when integrated over 4π steradians they yield the single scattering albedo of the particles. On the polar plot on the left hand side, the light is incident from the left and is scattered in all directions. For $x << 1$ (shown in orange) the scattering is divided equally in the forward and the backward direction, consistent with Rayleigh scattering (Jackson, 1999; Zangwill, 2013).

For particles much larger than the wavelength of incident light (shown in green in Figure 1.1) the scattered light is concentrated in the forward direction with some amount of light scattered in the backward direction. This is consistent with geometric optics and classical diffraction (Jackson, 1999; Zangwill, 2013). In classical diffraction theory, the angle of the first minimum of scattering intensity is related to the object

[1]https://miepython.readthedocs.io/en/latest/

size by $sin(\theta)_{Ist.min} = 1.22\lambda/d = 3.83/x$ and most of the scattering intensity is concentrated in a very sharp central lobe. The values for the green curve are scaled in order to visualize the plot clearly.

When $x \approx 1$ (i.e. the wavelength is of same order as the particle size) the scattering becomes more complicated due to various interference phenomena and so is only accurately described by Mie theory (Wriedt, 2012). However, as shown in Figure 1.1 the general result is that the particles are strongly forward scattering, unlike the situation when $x << 1$. As the particle size increases, the width of the forward-scattering peak gets narrower, again consistent with standard diffraction theory.

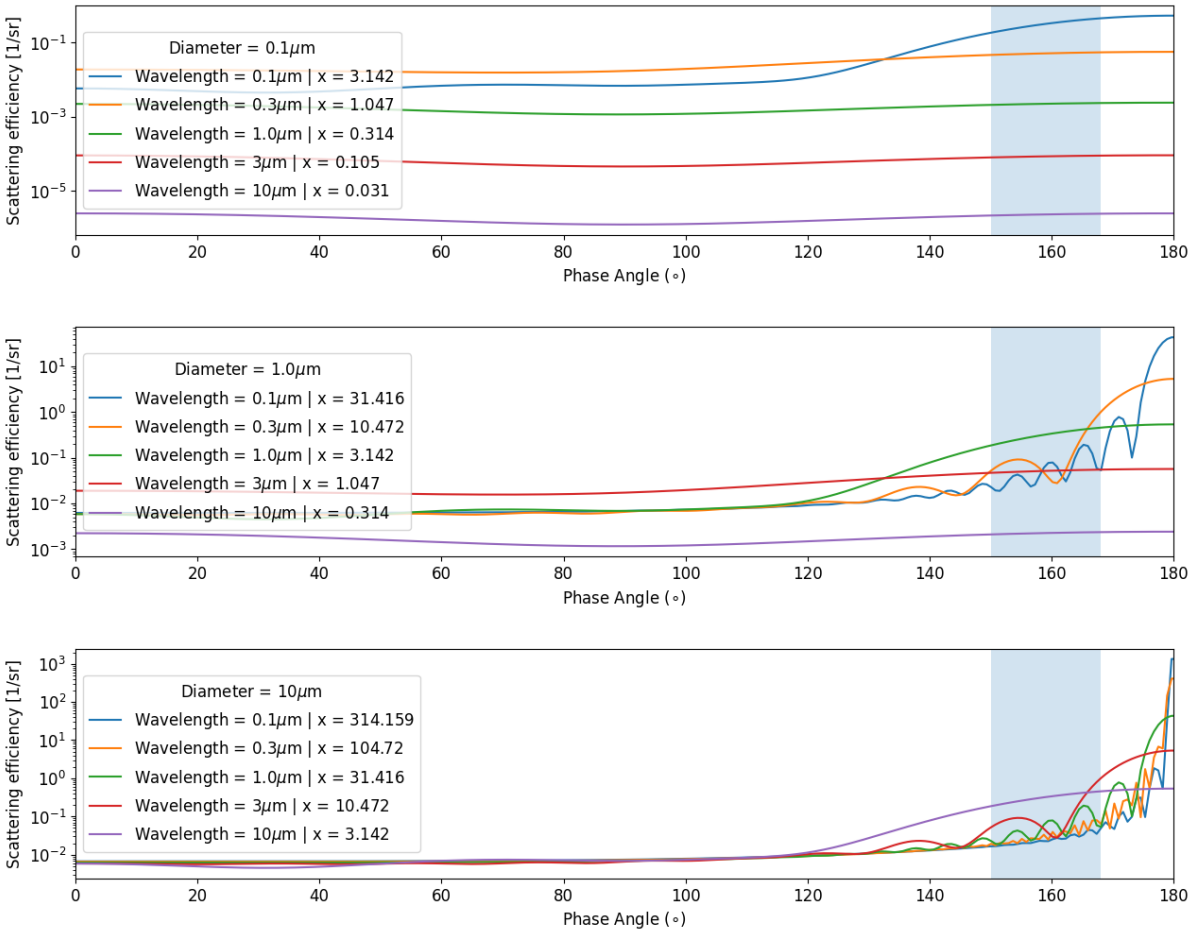

FIGURE 1.2: This figure shows the scattering efficiency on y-axis on a log scale and the phase angle on the x-axis for a sphere calculated using Mie scattering theory (python package "miepython"). Each panel shows the scattering efficiency versus phase angle for a different particle diameter at several different wavelengths. Note that the peak scattering efficiency is higher for larger particles, but these also scatter light over a smaller range of angles. The shaded region shows the phase angles of the observations studied in this dissertation. In this phase range (150° - 168°) particles scatter light most efficiently at wavelengths comparable to the particle size.

These variations in the scattering properties of particles with different values of x mean that particles of different sizes will scatter light with different efficiencies in different directions. These trends are illustrated in Figures 1.2 and 1.3, which show the scattering efficiency as a function of phase angle (180°-scattering angle) for particles of different sizes observed at different wavelengths. These efficiencies are all calculated using the code "miepython". Three common patterns can be seen in both Figures 1.2 and 1.3: 1) scattering efficiency increases with x until $x \approx 1$, then

levels off; 2) when $x > 1$, the scattering efficiency increases at higher phase angles; 3) larger particles have narrow forward-scattering peaks as compared to the smaller particles, which is consistent with standard diffraction theory.

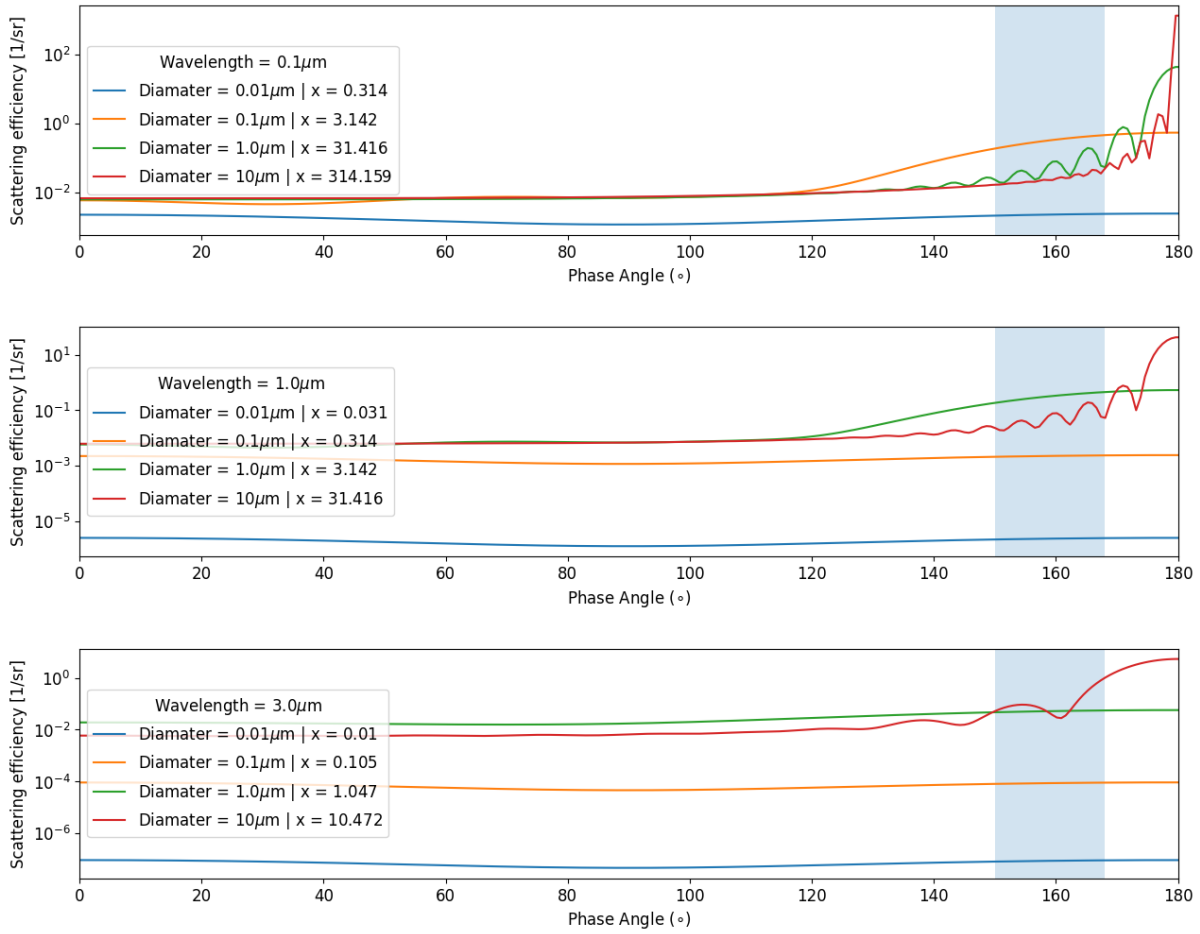

FIGURE 1.3: This figure shows the scattering efficiency of light on y-axis with a log scale and the phase angle on the x-axis for a sphere of refractive index m = 1.5 - 1j using Mie scattering theory (python package "miepython"). Each panel shows the scattering efficiency at a particular wavelength for a range of different particle sizes. The shaded region shows the phase angle range for the observations used in the current work. Note that the scattering efficiency is a roughly uniform function of phase angle in cases where $x << 1$, but peaks at high phase angles when $x \approx 1$ and $x >> 1$, with the width of the peak being narrower for larger particles. Particles with sizes similar to the wavelength of light are most efficient at scattering light in the range of phase angles 150° - 168° used in this work.

In this study, the spectral data is recorded at wavelengths of 0.2 - 5.0 μm (0.25 - 0.8 μm in Chapter 2 and 1.0 - 5.0 μm in Chapters 3 and 4) at high phase angles shown

by the shaded region in Figures 1.2 and 1.3 (168.3° in Chapter 2 and 150 - 162° in Chapters 3 and 4), and in this observation regime, particle sizes close to the incident wavelength will scatter light most efficiently. In Figure 1.3, at an incident wavelength of 1.0 μm, particles of diameter 1.0 μm (green curve) scatter light most efficiently in the phase angle range of 150 - 168° (shown by the shaded region in the middle panel). Similarly, at incident wavelengths of 0.1 μm, particles of comparable size (i.e., around 0.1 μm) will scatter light most efficiently at phase angles of 150° - 168°. Thus the relative brightness of a region at different wavelengths depends upon the relative density of particles with different sizes, and so the shape of the spectra of provides information about the particle size distributions in the region being observed. This is the basic principle used below to translate spectral data into particle properties.

The two models of light scattering used in this dissertation are Fraunhofer diffraction and Mie Scattering theory. Fraunhofer diffraction theory is an approximate solution for largely opaque objects, where transmission can be neglected (Kolokolnikov *et al.*, 2019; Jackson, 1999). We use Fraunhofer diffraction model to compute the scattering pattern in the first research paper of this dissertation where in the observations were made at such high phase angles that the observed light is predominantly due to diffraction around individual particles. In this case, the value of power scattered obtained using the Fraunhofer model differs from that derived from Mie theory by less than a factor of 2, and so is sufficiently accurate for setting limits on the dust population close to the moon's surface. Mie scattering theory is an exact theory for calculating light scattered from perfect spheres with specified optical constants, and so allows for the possibility of light passing through the particle. This is particularly important for transparent materials like ice, so we use Mie scattering theory to generate theoretical spectra for icy particle in Enceladus' plume.

One of the primary problems addressed in this work is how to study spectra that contain noise. Noise in spectral data refers to variations or fluctuations in the measured signal that are unrelated to the physical properties of the object being observed. Noise can obscure important information in the spectrum and affect the accuracy and reliability of spectral analysis. Noise can arise from various sources and can be problematic in a wide range of scientific and engineering applications.

Some common sources and and types of noise are thermal, electronic, environmental, detector, scattering and absorption, quantization and data acquisition (Colaprete *et al*., 2015). Instrument noise arises from imperfections or limitations in the sensors and instruments used to capture data including electronic noise, sensor calibration errors, and other instrumental artifacts that affect the accuracy of measurements (Sarantos *et al*., 2012). Detectors used in spectroscopy, such as photodiodes or charge-coupled devices (CCDs), may exhibit noise due to imperfections, dark current, or readout electronics (Xie *et al*., 2021). These noise sources can impact the quality of spectral data. Similarly, high-energy particles can interfere with data collection and solar radiation can affect observations and data transmission from spacecraft especially when it is closer to the sun. Thermal noise from temperature variations can affect the sensitivity and precision of instruments (Colaprete *et al*., 2015; Mccord *et al*., 2004). In imaging data, artifacts like dead pixels, lens flares, and sensor anomalies can be mistaken for actual features or objects in space.

Managing noise in spectral and planetary data is crucial to obtain accurate and meaningful results. The specific methods and techniques for noise reduction can vary depending on the type of data, the instruments used, and the nature of the noise. Understanding noise in imaging data includes the basic steps involved in calibrating these data, which include dark subtraction and flat-fielding. For imaging data, dark subtraction involves taking images with the same exposure time as the scientific data but with the camera shutter closed (Chavez Jr, 1988; Colaprete *et al*., 2015). This helps in identifying and removing electronic noise, such as dark current and readout noise. Flat-fielding corrects for variations in sensitivity across the detector or sensor. It involves dividing the data by a flat-field image that represents the instrument's response to uniform illumination (Roberts *et al*., 1986; Zhang *et al*., 2003; Colaprete *et al*., 2015). This process corrects for pixel-to-pixel variations in sensitivity. Signal processing techniques such as low-pass filtering can be applied to suppress high-frequency noise. Averaging multiple measurements can help reduce random noise, with the signal-to-noise ratio steadily improving as more and more measurements are averaged together. However, this statement might not be applicable to all situations, as it can affect temporal or spatial resolution. For spectral data, smoothing

techniques can be applied to reduce noise while preserving important spectral features. Subtracting a background spectrum (obtained without the sample) can remove unwanted noise and baseline variations. We use a combination of these techniques and use an iterative approach to fine-tune the data processing.

There are two different dust populations that were explored in this dissertation: (1) the dust found on our own Moon and (2) the dust found in the plume of Saturn's moon Enceladus. In Chapter 2, we focus on the dust population above the Moon's surface. Airless planetary bodies like the Moon constantly experience micrometeorite bombardment as well as the influence of solar radiation, solar wind, and other factors of outer space. Most of the lunar surface is covered with regolith, a mixture of fine dust and rocky debris composed mostly of oxygen, silicon, and iron, produced by the impacts of high-velocity micrometeorites over billions of years (Shoemaker and Morris, 1970; McKay *et al.*, 1991; Pohlen *et al.*, 2022). The side of the Moon that faces the Sun experiences solar radiation in the form of UV light that charges the regolith surface of the Moon. These photoelectrons form an electric field over the regolith that can exceed the gravitational forces and loft particles above the Moon's surface (Zakharov *et al.*, 2020).

Lunar dust carries information about the Moon's surface (Postberg *et al.*, 2011a). The moon's regolith is composed of small particles ground down by perpetual meteoroid bombardment and includes a significant number of micron and sub-micron particles (McKay *et al.*, 1991). Surveyor-7 photographed a bright glow along the western lunar horizon one hour after local sunset. Criswell (1973) reasoned that this horizon-glow (HG) must result from the forward scattering of sunlight by electrically charged dust grains [a (grain radius) = 5×10^{-4} cm], which are electrostatically levitated 3 to 30 cm above rocks. Dust is ejected from the lunar regolith by some combination of impacts and electrostatic lofting (Grün *et al.*, 2011; Zakharov *et al.*, 2020) and so the distribution of lunar dust can clarify these processes, as well as provide insights into the properties of the lunar regolith. Studying lunar dust can therefore help us to understand space weathering processes, such as micro-meteoroid impacts and solar wind interactions, which affect the surfaces of all rocky bodies in space.

At the same time, dust has practical effects that were first uncovered by the Apollo astronauts, who discovered manifestations of lunar dust (Zakharov *et al.*, 2020). The effects of lunar dust on Extra-Vehicular Activity (EVA) systems could be sorted into nine categories: vision obscuration, false instrument readings, dust coating and contamination, loss of traction, clogging of mechanisms, abrasion, thermal control problems, seal failures, and inhalation and irritation (Gaier, 2007). Understanding dust's behavior is crucial for designing protective measures for future lunar missions, including spacesuits, habitats and dust-resistant equipment for lunar missions.

In Chapter 3 and 4 of this dissertation, Saturn's moon Enceladus' plume is studied. Enceladus is the sixth largest moon of Saturn and was discovered by William Herschel in 1789. Enceladus orbits the planet within the extended E-ring with a semi-major axis of 238,020 km. Voyager images gave a reliable (equatorial) diameter of 513 km (Smith *et al.*, 1982) and showed the surface to be a composite of moderately cratered terrain and large expanses with no craters. Cassini, a spacecraft by NASA, was a space probe sent to study the planet Saturn and its system, including its rings and natural satellites. In 2005, multiple instruments onboard Cassini obtained definitive evidence for active ejections of water vapor and ice particles in a plume emerging from a series of fissures known as "tiger stripes" near the south pole of Enceladus (Porco *et al.*, 2006; Spencer *et al.*, 2006; Spahn *et al.*, 2006; Dougherty *et al.*, 2006; Khurana *et al.*, 2007; Schenk *et al.*, 2018; Brown *et al.*, 2006). The plumes of Enceladus make it interesting because no other icy body in the solar system is known to to exhibit such continuous and large-scale activity. The interior of Enceladus is of particular interest because various Cassini measurements suggest the existence of a global subsurface ocean (Collins and Goodman, 2007; Nimmo *et al.*, 2011; Iess *et al.*, 2014; Thomas *et al.*, 2016). The icy shell that covers the ocean may be tens of kilometers thick near the moon's equator, but could be extremely thin (1 - 5 km km) at the south pole (Nimmo *et al.*, 2011).

The Enceladus plume is composed of three different phases: gas, solids and ions, with neutral gas being the most abundant (Hansen *et al.*, 2017; Hedman *et al.*, 2013; Nimmo *et al.*, 2014). All three components are primarily composed of water with the solid phase being primarily in a crystalline state (Dhingra *et al.*, 2017). Other

constituents are sodium salts and organic materials (Postberg *et al.*, 2009, 2011b). These composition of ice grains are often referred to using the following distinction: Type I is nearly all water ice, Type II contains organic compounds, and Type III is rich in salts (Postberg *et al.*, 2008, 2011a). The composition information yields unique insights into interior processes and into the moon's environment. Cassini's measurements have shown that a greater part of the matter in the space between the orbits of the main rings and Titan is dominated by compounds that were once part of Enceladus (Postberg *et al.*, 2009; Horányi *et al.*, 2008; Kempf *et al.*, 2010).

Cassini's Visual and Infrared Mapping Spectrometer (VIMS) was a remote sensing instrument that captured images using visible and infrared light to learn more about the composition of moon surfaces, the rings, and the atmospheres of Saturn and Titan (Brown *et al.*, 2004). It consisted of two telescopes - one used to measure visible light, the other infrared. VIMS measured reflected and emitted radiation from atmospheres, rings and surfaces over wavelengths from 350 to 5100 nm, to help determine their compositions, temperatures and structures (Brown *et al.*, 2004). This dissertation discusses how VIMS observations of Enceladus' plume were used to derive information about the physical properties of the plume particles. There are challenges associated with these measurements: (1) the plume has a low optical depth such that the plume spectra have low signal-to-noise ratios, and (2) the plume particles are strongly forward scattering such that they do not exhibit strong absorption signals. These challenges make it difficult for us to derive useful information from these noisy data. This work discusses the different ways to deal with these challenges and extract reliable information from it.

The plume varies both spatially and temporally. The plume material over the fissures called Baghdad and Damascus Sulci has a dust-to-gas mass ratio roughly an order of magnitude higher than the material above the fissures named Alexandria and Cairo Sulci (Hedman *et al.*, 2018). Major temporal variations in the plume brightness emitted from ice grains, which varies by a factor of 4 between apocenter and pericenter due to the tidal stresses experienced by Enceladus (Hedman *et al.*, 2013; Nimmo *et al.*, 2014). In addition to these orbital-period changes, there are also brightness variations over timescales of years (Hedman *et al.*, 2013; Ingersoll and

Ewald, 2017). VIMS observations of these variations can provide insights into how plume particle properties vary across a range of different timescales and with altitude above Enceladus' south pole.

The rest of this dissertation is structured as follows: First, Chapter 2 discusses analyses of lunar dust observations made by LADEE-UVS. We discuss the results of constraints on dust particles and compare them with already established values in the planetary science community. Beginning with chapter 3, our focus shifts to the dust in Enceladus' plume. For the second paper we extract relevant information from our spectral data. The paper concludes with typical velocity of Enceladus plume particles and its implications on the launch process from the vents on the moon's south pole. In chapter 4, we study the size distribution of Enceladus plume particles and their variations on different scales such as the moon's orbital position, from one orbit to the next and across altitude. Chapter 4 extends the noise reduction techniques applied in Chapter 3 and uses a machine learning model that can handle the noise in these data. The use of this algorithm with noise is a novel technique that can have many applications in the field of planetary spectral science. Finally, the conclusion chapter summarizes the results from the three papers and how they can be used to drive further research.

CHAPTER 2

Constraining low-altitude lunar dust using the LADEE-UVS data

---

H. Sharma, M. M. Hedman, and D. H. Wooden, A. Colaprete, A. M. Cook, "Constraining Low-Altitude Lunar Dust Using the LADEE-UVS Data." Journal of Geophysical Research: Planets, 126.11, 2021

In this paper, the lunar dust population is explored. This was a challenging problem being the first project as part of my Ph.D. Dr. Hedman acquired the data used in this analysis. He wrote the IDL code that extracted the relevant parameters such as scattering angle, position of the spacecraft, instrument and measurements etc. from the LADEE-UVS data. I then used these extracted measurements to perform the rest of the data analysis including filtering, averaging and calculating the constraints on dust population using C and Python code. Dr. Hedman guided me on every step of the process. Co-authors A. Colaprete, A. M. Cook and D. H. Wooden provided helpful comments and suggestions during the publication process.

2.1 ABSTRACT

Studying lunar dust is vital to the exploration of the Moon and other airless planetary bodies. The Ultraviolet and Visible Spectrometer (UVS) on board the Lunar Atmosphere and Dust Environment Explorer (LADEE) spacecraft conducted a series of Almost Limb activities to look for dust near the dawn terminator region. During these activities the instrument stared at a fixed point in the zodiacal background off the Moon's limb while the spacecraft moved in retrograde orbit from the sunlit to the unlit side of the Moon. The spectra obtained from these activities probe altitudes within a few kilometers of the Moon's surface, a region whose dust populations were not well constrained by previous remote-sensing observations from orbiting spacecraft. Filtering these spectra to remove a varying instrumental signal enables constraints to be placed on potential signals from a dust atmosphere. These

filtered spectra are compared with those predicted for dust atmospheres with various exponential scale heights and particle size distributions to yield upper limits on the dust number density for these potential populations. For a differential size distribution proportional to s^{-3} (where s is the particle size) and a scale height of 1 km, we obtain an upper limit on the number density of dust particles at the Moon's surface of 142 m^{-3}.

2.2 INTRODUCTION

Lunar dust, because of its adherence and abrasive properties, is prone to damaging spacesuits and instruments, as well as reducing visibility during landing, and thus poses a hazard to lunar exploration (Michael Holland and Simmonds, 1973; Khan-Mayberry, 2008). Surface electric fields and dust transport on the Moon's surface could also compromise future astronomical observations from the Moon (Stubbs *et al.*, 2007). It is therefore vital to study this dust environment in order to develop solutions for dust-related problems.

Furthermore, characterizing the dust density at different altitudes above the Moon's surface can reveal the amount of dust that gets ejected from the surface and thus clarify dust transport on airless planetary bodies (Wang *et al.*, 2016). Dust above airless bodies can be naturally lofted by micro-meteoroid impacts (Popel *et al.*, 2016). However, some dust grains could also be levitated above the Moon's surface by electrostatic forces (Colwell *et al.*, 2009; Orger *et al.*, 2018). Furthermore, future missions to the surface can loft significant amounts of dust (Metzger, 2020; Immer *et al.*, 2011; Lane and Metzger, 2012) and so understanding the current dust environment can provide a useful baseline for its dynamics and distribution.

Information about the lunar dust exosphere comes both from remote sensing (McCoy, 1976; Glenar *et al.*, 2011; Glenar *et al.*, 2014; Feldman *et al.*, 2014; Rennilson and Criswell, 1974) and in-situ observations (Berg, 1978; Grün *et al.*, 2011; Szalay and Horányi, 2015). Remote sensing observations include excess brightness measurements in the photometrically calibrated coronal photography and the visual observations of extended lunar horizon glow by Apollo 17 astronauts, which were

attributed to forward scattering of sunlight by dust particles (McCoy, 1976). A reanalysis of the Apollo observations by Glenar *et al*. (2011) concluded that this dust cloud would extend into shadow a distance between 100 and 200 km from the terminator. More recently, faint signals in some of the images from the Clementine navigational star tracker measurements were matched to a dust exosphere with a dust column of about 5 - 30 cm^{-2} and scale heights of 3 km and 12 km. (Glenar *et al*., 2014). Dust within a few kilometers of the surface is probably undetectable in these measurements since it corresponds to a small part of the pixel's field of view. The Lyman-Alpha Mapping Project far ultraviolet spectrograph on the Lunar Reconnaissance Orbiter (LRO) has estimated upper limits for vertical dust column at less than 10 grains cm^{-2} of 0.1 μm size (Feldman *et al*., 2014). These far-ultraviolet measurements were within the wavelength range 170 and 190 nm and could probe altitudes down to about 10 km, limited by shadowing. Closer to the surface, light from very low-altitude dust was observed by each of the Surveyor 7, 6 and 5 landers along the western lunar horizon following local sunset (Rennilson and Criswell, 1974).

In-situ measurements of lunar dust include data from the Lunar Ejecta and Meteorite (LEAM) Experiment deployed by Apollo 17, which registered a multitude of unexpected hits during lunar sunrise and sunset, possibly caused by slow moving and highly charged dust grains transported across the lunar surface (Berg, 1978; Grün *et al*., 2011). LEAM events are consistent with the sunrise/sunset–triggered levitation and transport of slow moving, highly charged lunar dust particles (Colwell *et al*., 2007) indicating that the amount of lunar dust varies with local time. More recently, the LDEX experiment on board the LADEE spacecraft observed an extremely tenuous asymmetric dust cloud around the Moon with peak densities around 0.004-0.005 m^{-3} near the dawn terminator for a grain size threshold of 0.3 μm extending hundreds of kilometers above the Moon's surface (Horányi *et al*., 2015). This instrument also reported an upper limit of 100 m^{-3} on the dust density of particles larger than 0.1 μm in the altitude range of $\simeq$ 3-250 km for a putative population of electrostatically lofted dust (Szalay and Horányi, 2015).

In this paper, we analyze the spectra obtained by LADEE's Ultraviolet-Visible Spectrometer (UVS). The UVS made a series of Almost Limb observations from a spacecraft altitude of about 20 km of the lunar sunrise terminator at different locations and times shown in Table 2.1. The observation geometry during the Almost Limb activities enables us to probe the Moon's dust atmosphere at altitudes ranging between 1 and 10 km above the surface. These data probe lower altitudes than any of the prior remote sensing observations from orbiting spacecraft, and even reach below the lowest reported altitudes sensed by the LDEX instrument. Therefore, we aim to constrain whether any additional population of dust exists between 1 and 10 km of the surface beyond the dust cloud seen by LDEX. Given that the nature of the low-altitude dust populations seen by surface observations like LEAM and Surveyor are still uncertain, we will derive empirical limits on this dust population for a range of possible particle populations.

Section 2.3 below describes how we processed the Almost Limb data to obtain the tightest limits on potential dust populations. Note that these data contain a fluctuating signal that is inconsistent with a dust atmosphere whose density declines with altitude. We, therefore, apply a spectral filter to eliminate these fluctuations and isolate signals that can be used to set constraints on the dust atmosphere. We then compare these filtered spectra to the expected signals from various dust populations obtained using a Fraunhofer-diffraction model in order to derive upper limits on the dust particle densities. These constraints are summarized in Section 2.4 and compared with prior limits on the low-altitude dust atmosphere.

2.3 METHOD

The process by which we constrain the dust populations above the Moon's surface from the UVS Almost Limb data has multiple steps, which are described in detail below. Section 2.3.1 gives a brief description of the UVS instrument and describes in detail the Almost Limb activities and their geometry. Section 2.3.2 then describes how the spectra are processed to isolate the dust signal. Section 2.3.3 next discusses how we produce predicted spectra for various dust densities and particle size distributions

TABLE 2.1: Almost Limb activities used in this analysis

Filename	Mid time	Observed		Sub-Solar	Sub-Earth
		latitude	longitude	longitude	longitude
1836A	01 Apr 2014 22:40:16	24.33°	58.43°	157.88°	5.54 °
1840A	02 Apr 2014 08:10:22	24.19°	53.63°	153.65°	5.58°
1847A	03 Apr 2014 03:10:28	23.82°	44.07°	143.37°	5.48°
1873A	05 Apr 2014 23:13:22	23.00°	9.73°	108.76°	3.53°
1875A	06 Apr 2014 04:52:56	23.13°	6.83°	105.88°	3.28°
1880A	06 Apr 2014 18:05:14	23.51°	0.06°	99.17°	2.67°
1882A	06 Apr 2014 21:51:26	23.62°	358.12°	97.25 °	2.48°
1889A	07 Apr 2014 14:50:09	24.16°	349.38°	88.63°	1.63°
1901A	08 Apr 2014 21:01.12	24.94°	333.87°	73.29°	0.04°
1918A	10 Apr 2014 14:31:13	24.86°	317.77°	52.23°	-2.05°
1929A	11 Apr 2014 20:42:35	25.37°	303.42°	36.91°	-3.35°
1956A	14 Apr 2014 17:20:29	22.82°	269.43°	2.11°	-5.06°
1969A	16 Apr 2014 11:58:26	24.26°	247.64°	340.50°	-5.09°
1987A	17 Apr 2014 21:20:19	24.85°	230.67°	323.60°	-4.57°

using a Fraunhofer diffraction model. Finally, Section 2.3.4 describes how we compared our modeled spectra with the spectra obtained by the UVS instrument in order to constrain dust densities above the surface.

2.3.1 *UVS Almost Limb observations*

The LADEE-UVS instrument is described in detail in Colaprete *et al*. (2014), but for the sake of completeness we review some of its properties here.

This instrument observes light with wavelengths between 250 and 800 nm over a 1-degree field of view via a catadioptic telescope that is coupled by a fiber-optic cable to a spectrometer with a spectral resolution of $\lambda/\Delta\lambda \sim 900$ at 500 nm. The spectrometer disperses this light onto a 1044×64 (1024×58 active) pixel detector CCD array. Each column of pixels is binned within the detector, delivering a 1×1044 pixel spectrum. The raw signals recorded by the instrument are processed by standard pipelines in four steps: dark and bias correction, normalization by integration time, second order grating effects correction, and finally the radiance calibration. Each calibrated spectrum recorded by LADEE-UVS therefore contains 1024 active records of radiance in units of W m^{-2} nm^{-1} sr^{-1}. However, when considering the light

scattered by solid material like dust or the Moon's surface, it is more useful to instead consider reflectance, which is typically expressed in terms of the unitless ratio I/F, where I is the intensity of the scattered radiation and F is the solar flux density (solar flux divided by π). Hence for this investigation we converted the UVS radiance data to I/F values using a standard solar spectrum (Mecherikunnel and Richmond, 1980) at 1024 wavelengths ranging from 229.26 nm to 812.55 nm.

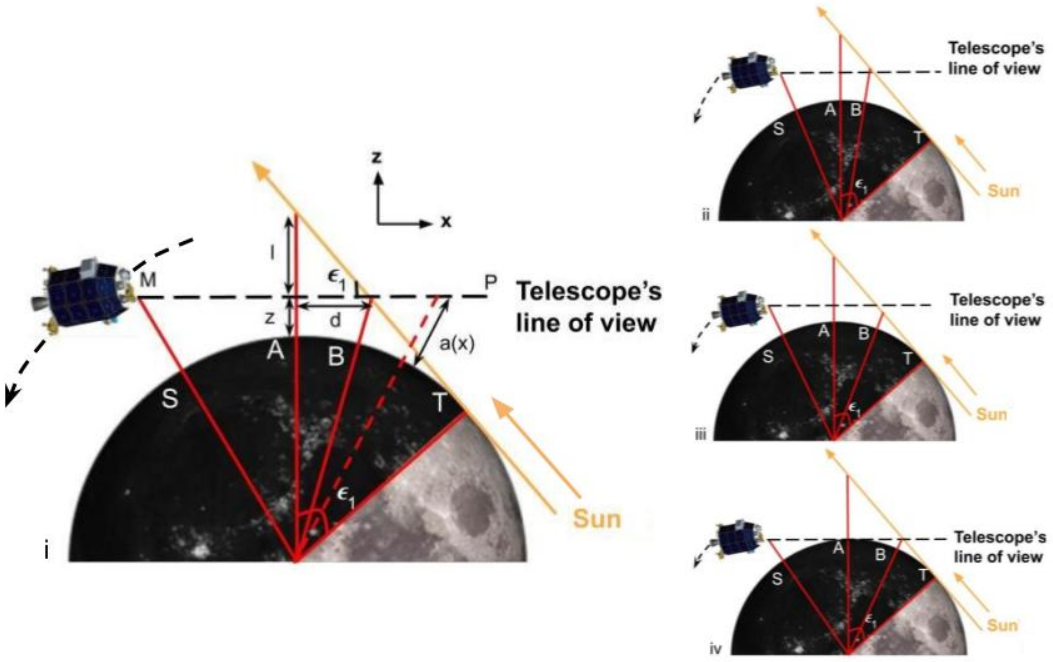

FIGURE 2.1: Illustrations of the Almost-Limb observation geometry using a 2D projection of the geometry in the plane containing the UVS, the line of sight and the lunar center. Note the Moon is not shown to scale in these diagrams. (i) Definitions of relevant geometrical parameters (see also A.1). The black dashed line represents the line-of-sight of the telescope, ϵ_1 and $a(x,t)$ are the Sun's elevation angle at that position and the height above the surface for any point lying on the field of view, respectively. T marks the Terminator point, S is the position on the surface directly below the spacecraft, A is where the telescope's line of sight gets closest to the lunar surface, and B is the point where the line of sight crosses into the shadowed region. Figures (ii), (iii) and (iv) show how the geometry changes over the course of the Almost Limb activity. During this activity the telescope moves around the Moon, so its line of sight approaches and crosses the limb shortly after the Sun sets. At the end of the Almost Limb activity the telescope field of view, which points at the fixed direction relative to the Sun, intercepts the Moon's unlit surface.

The LADEE mission executed science observations in lunar orbit spanning 2013 Oct 16 - 2014 Apr 18. Over the duration of the LADEE mission, UVS executed 1890 activities, collecting over 1 million spectra. During the last month of the mission, the UVS instrument obtained 15 so-called "Almost Limb" observations as the spacecraft lowered its altitude before crashing into the surface. These observations will be the exclusive focus of this study.

The 14 Almost Limb activities included in this analysis are summarized in Table 2.1 (One Almost Limb activity, designated 1855A, did not contain any useful data and is therefore omitted from this analysis). The duration for each of these activities was approximately 8 minutes. Table 2.1 also shows the latitude and longitude of the point where the telescope's line of sight first intersected the Moon's surface during the course of each observation.

During each Almost Limb activity, the spacecraft flies over the Moon on a retrograde orbit at an approximately constant altitude while the telescope points in a fixed direction relative to the Sun, so that the telescope stares at a fixed location in the sky 12° away from the Sun that crosses the limb shortly after the Sun sets. Figure 2.1 is a 2D projection of the observation geometry in a plane containing UVS line of sight and the Lunar center. This type of observation allows the faint signals from dust near the Moon's surface to be cleanly isolated from other astronomical signals like zodiacal light.

Zodiacal light is a diffuse signal created by sunlight scattered off of interplanetary dust (Leinert *et al.*, 1998; Stubbs *et al.*, 2007; Lasue *et al.*, 2020) that is often a significant background for remote-sensing searches for lunar dust (Stubbs *et al.*, 2010; Feldman *et al.*, 2014). The brightness of zodiacal light relative to Lunar Dust is expected to be lower at the ultra-violet wavelengths observed by LADEE-UVS than it is at visible wavelengths (Stubbs *et al.*, 2010), but it cannot be completely neglected. Fortunately, during each Almost Limb activity LADEE-UVS stares at a single point in the sky that is nearly fixed relative to both the Sun and distant stars (the apparent motion of the Sun being negligible over the few minute duration of a typical observation). The signals from zodiacal light and other astronomical backgrounds therefore should remain constant over the course of each observation. By contrast, the signal from

dust should increase as the line-of-sight approaches the Moon's surface, producing a time-variable signal that can be cleanly separated from such constant backgrounds.

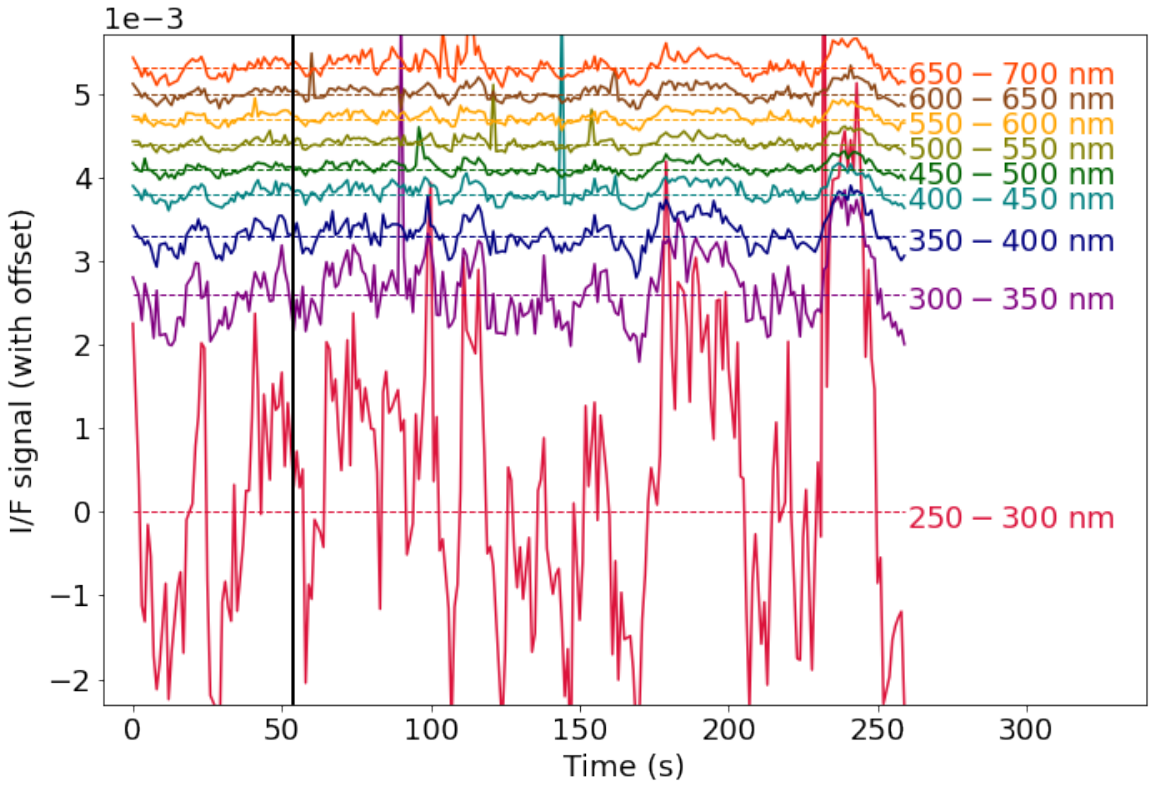

FIGURE 2.2: Unfiltered I/F values for different wavelength ranges as recorded by the UVS instrument on board LADEE during the Almost Limb activity, 1969A. An offset has been added to these values to view the various wavelength ranges distinctly. The vertical black line on the plot denotes the point (t_V) when the telescope's line of view hits the Moon's surface. The fluctuations in the signal level persist even after the telescope's field of view crosses the Moon's terminator, indicating that these fluctuations are likely instrumental artifacts.

2.3.2 *Spectral filtering*

Initial looks at the LADEE-UVS Almost Limb data revealed signal fluctuations that were inconsistent with the model of a uniform dust atmosphere. The signal from dust is expected to be broadband (Stubbs *et al.*, 2010; Van de Hulst, 1957) so we calculated the average of reflectance values for wavelength ranges of width 50 nm from 250-300 nm to 650-700 nm. (Wavelengths shorter/longer than the above range have not been considered for this analysis because their signal-to-noise ratio was poor.) Figure 2.2

shows the resulting average I/F values for the Almost Limb activity 1969A after the Sun sets. The vertical black line on the plot, denotes the point (t_V) when the telescope's line of view meets the Moon's surface. An offset has been added to the spectral channels to view each wavelength signal distinctively.

The signals in Figure 2.2 do not show any obvious trends with altitude above the limb that would be expected from exospheric dust. Instead, the signals contain fluctuations that persist beyond the point when the telescope is viewing the unlit part of the lunar surface. This is not consistent with any dust atmosphere, which would produce a signal that increases with decreasing altitude above the limb and then disappear when the telescope starts viewing the unlit surface.

The origins of these fluctuations are still unknown. The signal fluctuations seen in Figure 2.2 have a similar shape in all the frequency bands, so they likely have a common source with a distinct broad-band spectrum. However, since the spacecraft is in shadow and viewing the dark side of the Moon for part of the time the spacecraft sees these signals (cf. Figure 2.1), it seems unlikely that they represent fluctuations in the amount of light entering the instrument. Likewise, these signals also do not show any correlation with variations in instrument parameters like the target and detector temperature, so they cannot be clearly associated with something internal to the instrument.

Regardless of their origin, these fluctuations obscure the signal from the dust atmosphere. Fortunately, these variations have a different spectrum from dust, and so we can use spectral filtering techniques to remove these variations and isolate potential dust signals in order to constrain any real signals from low-altitude dust.

Let us assume that the total signal S_i in a wavelength channel i in Figure 2.2 is a combination of a dust signal D_i and the varying signal V_i, both of which change with time such that,

$$S_i(t) = D_i(t) + V_i(t). \tag{2.1}$$

The key thing to note is that any spectrum beyond the point of time, t_V at which the line of view hits the surface is entirely due to $V_i(t)$ such that, $S_i(t > t_V) = V_i(t > t_V)$. If the fluctuating signal has a fixed spectrum, then the value of $V_i(t > t_V)$ at any

single wavelength should be a linear function of the average value of $V_i(t > t_V)$ over all wavelengths (i.e. $\bar{V}(t > t_V) = \sum_i V_i(t > t_V)/N$, where N is the number of wavelength bands). Figure 2.3 shows the varying background, $V_i(t > t_V)$ for each wavelength range, i plotted against the average background, $\bar{V}(t > t_V)$ for the complete wavelength range (250-700 nm) for the Almost Limb activity 1969A and considering only times $t > t_V$. This plot confirms that the signal at each wavelength is indeed proportional to the average signal over all wavelengths.

We therefore perform a linear fit to the values of $V_i(t > t_V)$ in each spectral channel i as a function of the mean signal $\bar{V}(t > t_V)$ and use the slope and offset of these fits (m_{V_i} and b_{V_i}) to derive the following estimates of $V_i(t)$ at each wavelength:

$$V_{i,est}(t) = m_{V_i}\bar{V}(t) + b_{V_i}. \tag{2.2}$$

Figure 2.4 shows the derived values of m_{V_i} as a function of wavelength, which is essentially the normalized spectrum of V_i. The spectrum of this signal is clearly different from the spectrum of the expected dust signal (derived in Section 2.3.3), so it should be possible to remove V_i without completely removing the dust signal. Specifically, consider the following quantity:

$$D_{i,est}(t) = S_i(t) - m_{V_i}\bar{S}(t) - b_{V_i} \tag{2.3}$$

where $\bar{S} = \sum_i S_i(t)/N$, and m_{V_i} and b_{V_i} are the same slope and intercept parameters from Equation 2.2 derived from the data obtained at times $t > t_V$.

If we insert $S_i(t) = D_i(t) + V_i(t)$ into this expression, we obtain:

$$D_{i,est}(t) = D_i(t) + V_i(t) - m_{V_i}\bar{D}(t) - m_{V_i}\bar{V}(t) - b_{V_i} \tag{2.4}$$

where $\bar{D}(t) = \sum_i D_i(t)/N$. Provided that $V_{i,est}(t)$ is a good estimate of $V_i(t)$ both before and after t_V, the terms involving $V_i(t)$ and $\bar{V}(t)$ will cancel, leaving

$$D_{i,est}(t) = D_i(t) - m_{V_i}\bar{D}(t). \tag{2.5}$$

The quantity $D_{i,est}$ should therefore not contain any contamination from the fluctuating instrument signal, at the cost of the dust signal being attenuated by a predictable factor. (In practice, we also need to remove a small number of data points that are large outliers to the mean trends, which we do by excluding any data where $S_i(t)$ is more than 3σ from its mean value in any of the wavelength bands.)

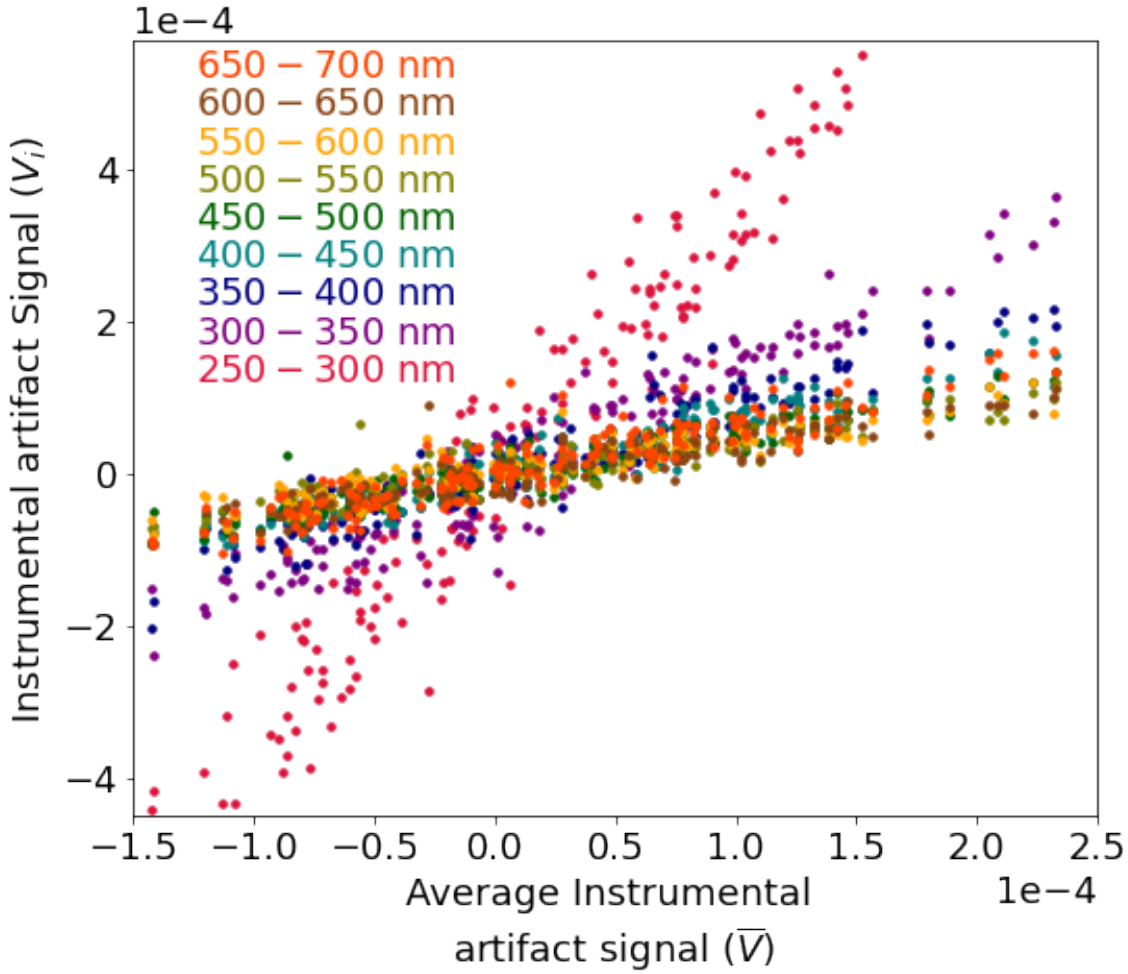

FIGURE 2.3: The varying signal, $V_i(t > t_V)$ for each wavelength band in the Almost Limb activity 1969A plotted against the average signal, $\bar{V}(t > t_V)$ over the whole wavelength range (250-700 nm). Note the strong correlations between each individual spectral channel and the average signal.

The filtered signal $D_{i,est}(t)$ for observation 1969A is shown in Figure 2.5 and indeed the fluctuations are much reduced, as desired. The results of applying this

filtering technique to the other Almost Limb activities are shown in A.2. In all cases, the fluctuations are significantly reduced.

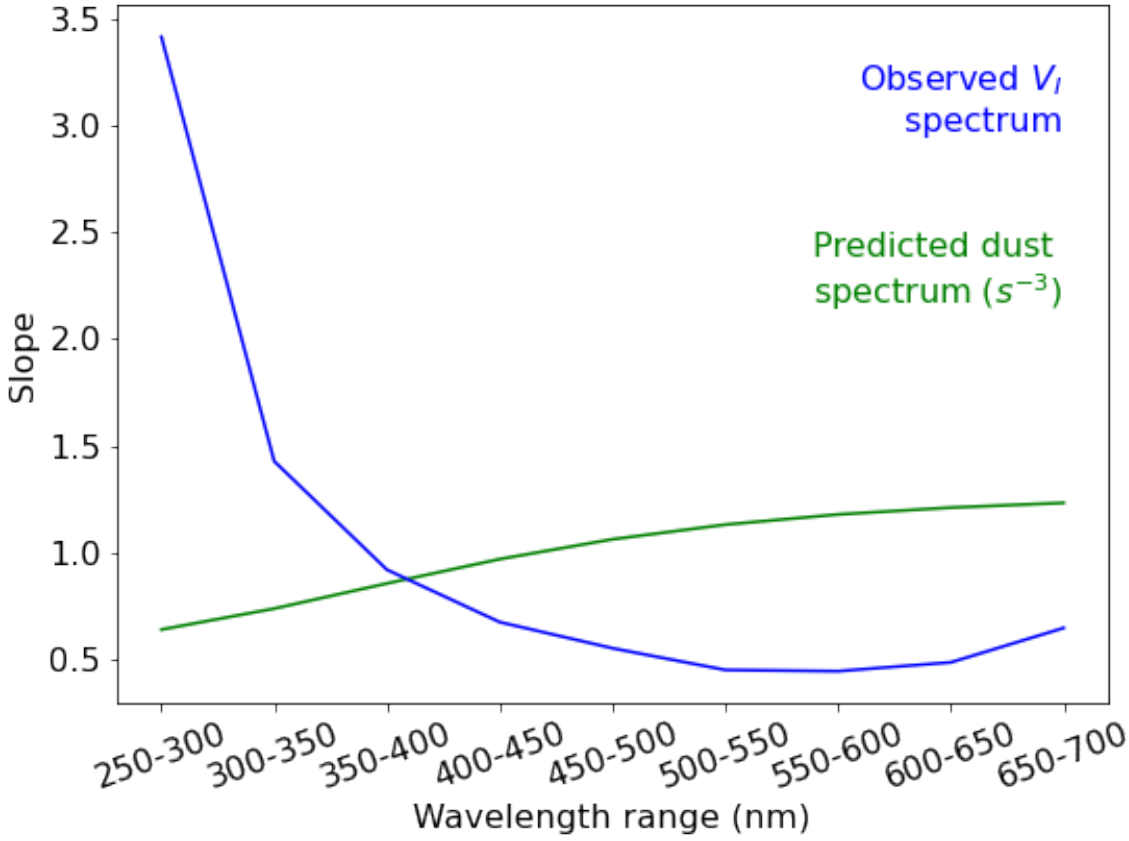

FIGURE 2.4: The slope m_{V_i} from equation 2.2 for a linear fit of the scatter points in Figure 2.3 between the variance signals at each wavelength $V_i(t > t_V)$ versus the average variance signal $\bar{V}(t > t_V)$ for the Almost Limb activity 1969A is shown as the blue line. The green line for comparison, is the predicted slope for a dust atmosphere with a power-law particle size distribution (s^{-3} with a threshold of 0.3 μm) described in Section 2.3.3. These slope curves are equivalent to normalized spectra of the varying signal and dust, respectively. Since these two spectra are so different, filtering out a signal with the blue spectrum will not eliminate signals with something like the green spectrum.

When we apply this filtering technique to the first Almost Limb activities, we observe an interesting phenomenon that further illustrates this technique can reveal real signals in the data. Figure 2.6 shows an example of the results from processing one of these earlier observations (1840A). In this case, the filtered signal shows a clear brightness change at the limb crossing time t_V, with the signals at short wavelengths

becoming more negative while those at long wavelengths become more positive. Since these signals do not change with altitude above the limb, these are probably not real dust signals. Instead, they are almost certainly due to Earthshine, which causes the surface of the Moon to be slightly brighter than the background sky. Earthshine is expected to have a red color, which is consistent with the wavelength trends observed here. Furthermore, these shifts are only clearly visible in the earliest observations, which are also the ones expected to be most strongly affected by Earthshine (see Table 2.1 and Figure A.10).

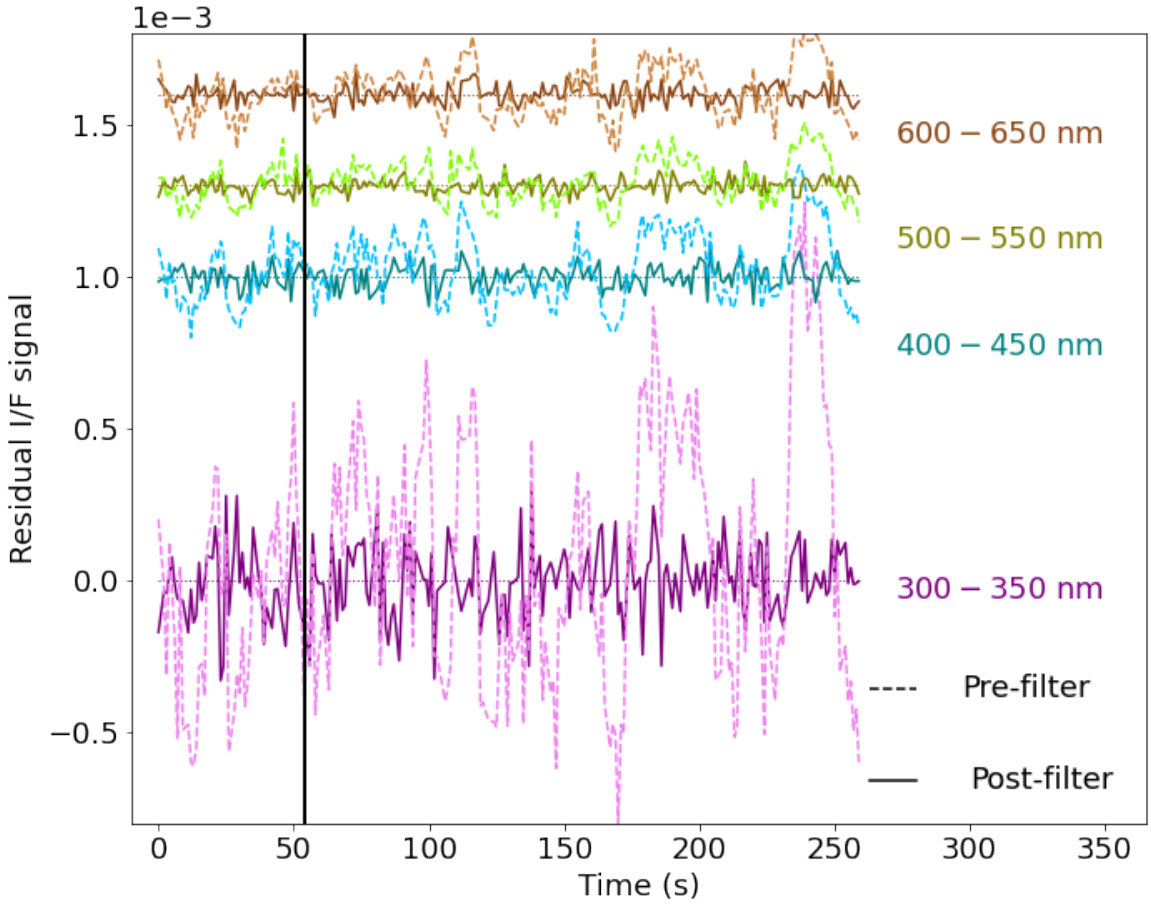

FIGURE 2.5: Corrected signal, $D_{i,est}(t)$ for the Almost Limb activity 1969A, after spectral filtering has been applied to each wavelength range (solid lines) compared with the original data (dashed lines). The vertical black line on the plot, denotes the time (t_V) when the telescope's line of view hits the Moon's surface. An offset has been added here too to view each wavelength range distinctly. Note the filtered data shows much smaller fluctuations than the raw data.

This demonstrates that our spectral-filtering process is able to reveal real astronomical signals that were previously obscured by the instrumental artifacts, and so means that we can also use these filtered data to search for signals from lunar dust. Taking a closer look at the other observations reveals that 9 observations have significant contamination from Earthshine.

But the remaining 5 observations can still be used to search for dust (see Section 2.3.4 below).

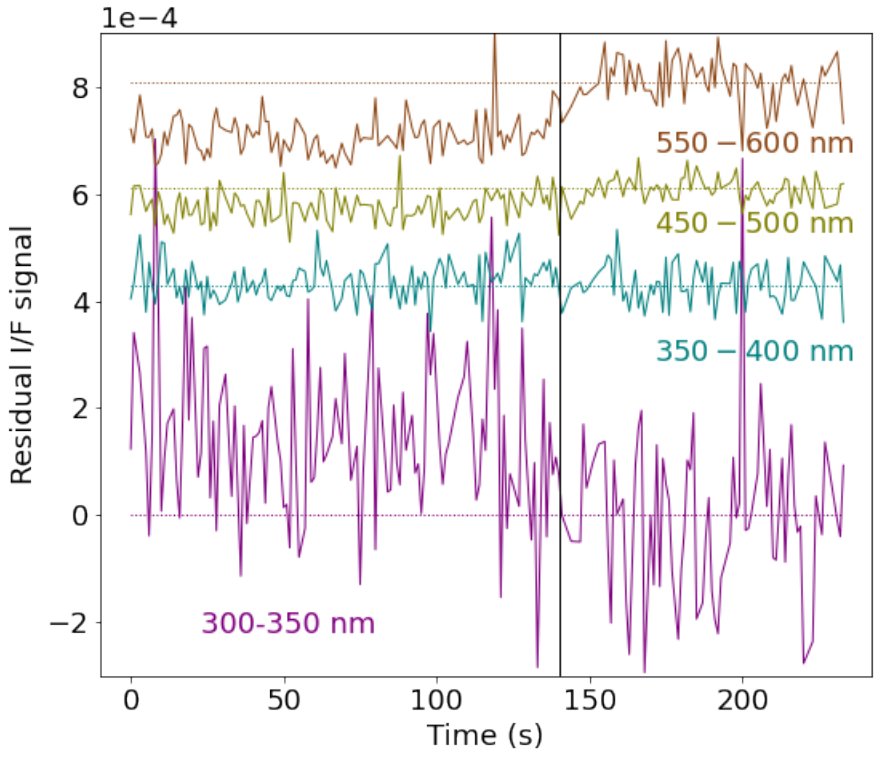

FIGURE 2.6: Corrected signal, $D_{i,est}$ for the Almost Limb activity 1840A, after spectral filtering has been applied to each wavelength range. The vertical black line on the plot, denotes the time (t_V) when the telescope's line of view hits the Moon's surface. An offset has been added here too to view each wavelength range distinctly. Note the slight shifts in the signal level beyond with the vertical line. These shifts are likely due to Earthshine from the Moon's surface, which is expected to be present in these early observations. The wavelength trends observed here are also consistent with the red color expected for Earthshine.

2.3.3 *Predicted signals from model dust atmospheres*

Since the filtered signals do not show clear variations with altitude that could be due to lunar dust, we need an explicit model to constrain the amount of dust that could be present. If we assume a density of particles at each altitude, the spectra can be computed using the appropriate scattering theory. For a flux of radiation πF with wavelength λ, the power scattered by an individual particle per unit solid angle is given by the function $\frac{dP}{d\Omega}$. In principle, these spectra could be computed using Mie Theory or even more sophisticated scattering theories that can account for the irregular shapes of these particles (Shkuratov *et al.*, 1994; Kolokolova *et al.*, 2015). However, in practice the Almost Limb activities were made at such high phase angles (168.3°) that the observed light is predominantly due to diffraction around individual particles, and the lunar dust populations are sufficiently tenuous that multiple scattering among different particles can be ignored. In this situation, Fraunhofer diffraction theory therefore provides a more efficient but still sufficiently accurate way to estimate the spectra of the relevant dust populations.

The power scattered per unit solid angle by a conducting disk of radius s illuminated by flux πF of radiation with wavelength λ is given by the following function (Jackson, 1975; Hedman *et al.*, 2009):

$$\frac{dP}{d\Omega} = \pi F s^2 \frac{J_1^2(k\,s\,\sin\theta)}{\sin^2\theta} \tag{2.6}$$

where s is the size (radius) of the particle, k=$2\pi/\lambda$, J_1 is the spherical Bessel function of first kind and θ is the scattering angle (180°-the phase angle). The above expression holds true for conducting materials, for dielectric particles we need to multiply the above expression by a scaling factor (Fymat and Mease, 1981). This scaling factor can be derived directly from the extinction factor Q_{ext} (the ratio of the total cross-section of the particle to its geometrical cross-section, see A.1) using the optical theorem which gives the following approximation for the scattering by a dielectric sphere:

$$\frac{dP}{d\Omega} = \frac{\pi F s^2}{4\sin^2\theta} J_1^2(k\,s\,\sin\theta) Q_{ext}^2(k\,s, m). \tag{2.7}$$

The above equation defines the power scattered per unit solid angle for particles of size s. This value of power scattered obtained using the Fraunhofer model differs from the Mie theory values by only a factor of about 0.97 - 1.8 for the ranges of particle sizes and observing geometries considered here, and hence can be considered a reasonable approximation of the expected signals from spherical particles. Furthermore, at low scattering angles (high phase angles) the signals from compact irregular grains differ from spheres with equivalent volume only by atmost 50%. (Pollack and Cuzzi, 1980). Our Fraunhofer calculations therefore also provide reasonable approximations for the signals for irregular grains with the equivalent effective sizes s.

The dust above the Moon's surface is a collection of particles of different size ranges for which a size distribution can be defined. The reflectance of this collection of particles in a given wavelength channel i and time t is given by the standard unitless quantity:

$$\left[\frac{I}{F}(t)\right]_{i,pred} = \frac{1}{F}\int_{s_{min}}^{s_{max}} \frac{dP_i}{d\Omega}\mathcal{N}(s,t)ds. \tag{2.8}$$

where $\frac{dP_i}{d\Omega}$ is the scattered power in wavelength channel i and $\mathcal{N}(s,t)$ is the particle size distribution integrated along the line of sight during that particular time. The limits on the above integral are defined by the lower and upper limits of the size distribution discussed below.

For this analysis, we will consider several different models for the spatial and size distributions of particles. However, we will assume that the particle size distribution is independent of location, and only the total density of particles varies with altitude above the Moon's surface. These assumptions not only make the calculations more tractable by restricting the phase space of possible predictions, but also facilitate comparisons with previously published measurements of these dust populations.

We consider two different types of particle size distributions in this study. On the one hand, we consider narrow size distributions for particles with radii between 0.07 to 1 μm in order to illustrate how sensitive these observations are to particles of different sizes (Feldman *et al.*, 2014; Glenar *et al.*, 2014). Also, narrow size

distributions could be more representative of electrostatically charged dust grains (Criswell, 1973; Rennilson and Criswell, 1974).

On the other hand, we consider power-law size distributions because these size distributions are also more likely to be representative of material lofted by impacts, which are expected to have a broad size distribution (Horányi *et al.*, 2015; Grün *et al.*, 2011). More specifically, we will use power-law size distributions with limits at 0.3 μm and 10 μm. These limits have been chosen to facilitate comparisons with previous limits on dust density (Horányi *et al.*, 2015; Szalay and Horányi, 2015; Glenar *et al.*, 2014; Feldman *et al.*, 2014) and because UVS operates at wavelengths between 200 and 800 nm and these sorts of remote sensing observations are more sensitive to particles comparable to the operating wavelength range of the instrument (Van de Hulst, 1957). Also, we consider two different cases for the power-law index: $\mathcal{N}(s,t) \propto s^{-3}$ and $\mathcal{N}(s,t) \propto s^{-4}$. These two numbers (-3 and -4) bracket the expected differential size distribution of collision debris, which has a differential index of around -3.5 (Dohnanyi, 1969; Tanaka *et al.*, 1996), and the value of -3.7 measured in-situ by LDEX (Szalay and Horányi, 2016).

In addition to assuming a specific size distribution, we also need to assume that the dust has a specific spatial distribution before we can compute the predicted signals and how they vary with time. Since this analysis seeks to constrain a low-altitude global dust atmosphere, we will assume that the number of particles per unit area along the line of sight can be described by a simple exponential dust profile defined by nominal total number density of particles at the surface $n_{o,nom}$ and scale height H. Such models are almost certainly an oversimplification because the actual dust distribution from both electrostatically lofted and impact-generated dust is a convolution of the launch velocity distribution of the particle populations ejected from the surface, which depends on how the particles are ejected, as well as their size and charge state. Both methods of launching dust can potentially send material to a wide range of altitudes (Szalay and Horányi, 2015; Horányi *et al.*, 2015). However, a simple exponential profile is a reasonable choice for this initial study, primarily because it facilitates comparisons with prior remote-sensing searches for and in-situ measurements of lunar dust, which have assumed exponential density

profiles (Feldman *et al.*, 2014; Glenar *et al.*, 2014; Szalay and Horányi, 2016). In this case, the total number of particles per unit area along the line of sight is given by the integral

$$N(t) = n_{o,nom} \int_{d}^{\infty} e^{-a(x,t)/H} dx \tag{2.9}$$

where x denotes the distance along the line of sight and $a(x,t)$ is the altitude above the surface at a particular time (see Figure 2.1). This integral is evaluated from a lower limit d that signifies the point where the dust is illuminated to an upper limit of $+\infty$ (see Figure 2.1). The lower limit d and $a(x,t)$ are both explicitly calculated in A.1. For this study, we will specifically consider scale heights H of 1, 3 and 5 km. These values were chosen because the LADEE-UVS data are most sensitive to variations in the dust density on these scales. These also correspond to scales that have not yet been probed by previous remote-sensing observations (Feldman *et al.*, 2014; Glenar *et al.*, 2014) and are near the lower limits of the published LDEX observations (Horányi *et al.*, 2015; Szalay and Horányi, 2015).

Finally, in order to account for the spectral filtering of the observations, we apply the same filter to the predicted I/F signal as we did to the observed data (see Equation 2.3) to create the following quantity.

$$P_{i,est}(t) = \left[\frac{I}{F}(t)\right]_{i,pred} - m_{V_i}\overline{\left[\frac{I}{F}(t)\right]}_{pred} - b_{V_i}, \tag{2.10}$$

where $I/F_{i,pred}$ is the predicted I/F for each wavelength channel i, $\bar{I/F}_{pred}$ is the average predicted I/F over all wavelengths, and m_{V_i} and b_{V_i} are the same parameters used in Equation 2.3. The resulting estimates of $P_{i,est}(t)$ can therefore be directly compared to the filtered observed values of $D_{i,est}(t)$ to derive limits on the dust signals.

2.3.4 *Comparison of UVS spectra and the Predicted signal*

Figures 2.7 - 2.8 show the predicted signal, $P_{i,est}(t)$ for a nominal surface concentration of 10^3 m^{-3} and scale heights of 1, 3 and 5 km overlaid on the observational data, $D_{i,est}(t)$ from Figures 2.5 and 2.6 with error bars based on the

scatter in the data points (Figures A.3, A.5, A.7 and A.9 for Almost Limb activities 1918A-1987A can be found in the A.2). As expected, the predicted signals become stronger as the telescope's line-of-sight approaches the lunar surface. Note that at short wavelengths the predicted signals are negative because m_{V_i} becomes large enough to flip the sign of the difference in Equation 2.10.

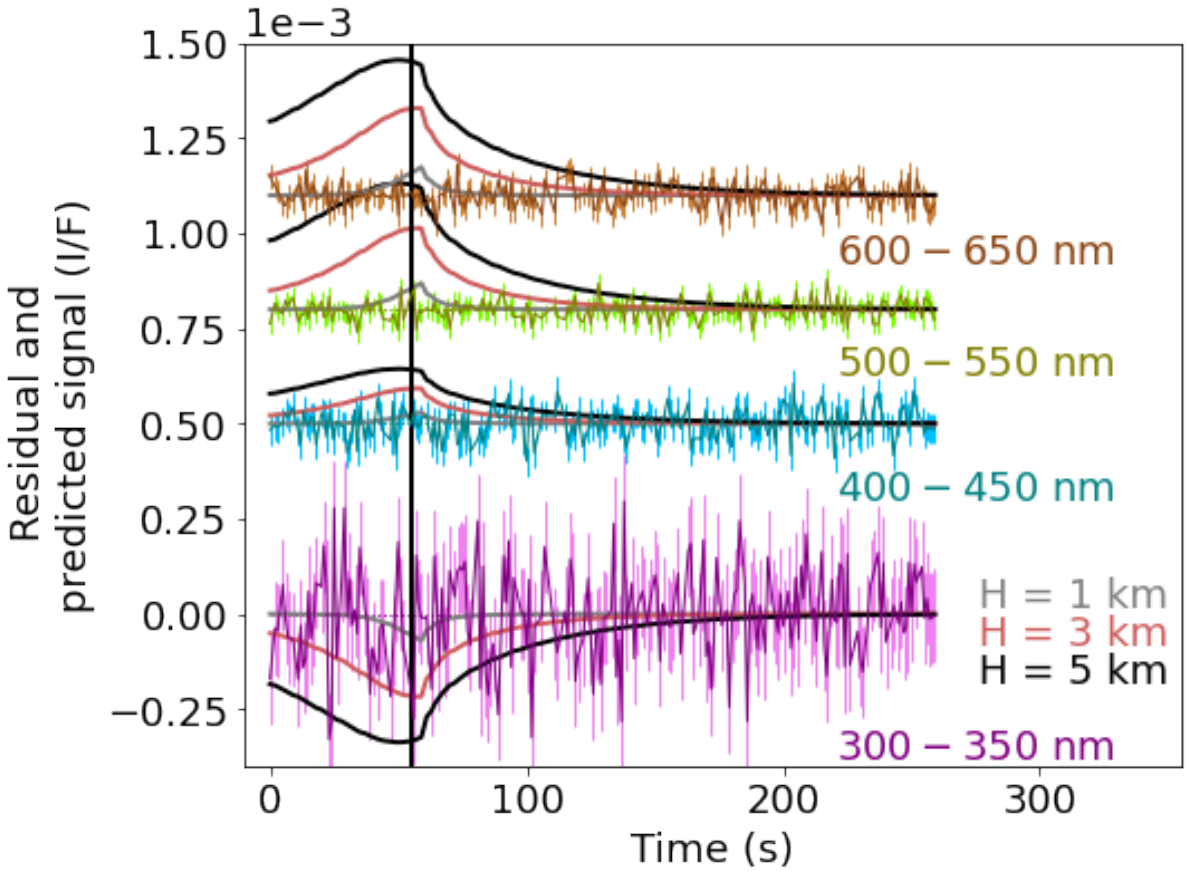

FIGURE 2.7: This figure shows the filtered residual I/F signal, $D_{i,est}(t)$ with error bars for Almost Limb activity 1969A at each wavelength range. The error bars are based on the scatter in the data points. The vertical black line on the plot, denotes the point (t_V) when the telescope's line of view hits the Moon's surface. The signal, $P_{i,est}(t)$ predicted using the Fraunhofer model and the exponential density profile for a size distribution proportional to s^{-3} and for scale heights of 1, 3 and 5 km, is plotted over the residual signal in grey, light coral and black, respectively. An offset has been added to view the signals distinctly. Note that the predicted signal, $P_{i,est}(t)$ is estimated for a nominal surface concentration of $n_{o,nom} = 10^3 m^{-3}$ and is greater than the residual signal, indicating that the upper limit on dust density will be below this value.

In Figure 2.7 the observed brightness trends are much smaller than the predicted trends for dust populations with an arbitrarily chosen nominal dust density of $n_{o,nom} = 10^3\ m^{-3}$. The limits these data can place on these low-altitude dust populations are therefore well below the value of $n_{o,nom}$. We derive quantitative limits on the dust density from each spectral channel by performing a least-squared linear fit of the observed signal calculated in equation 2.5 versus the model predictions from equation 2.10:

$$D_{i,est} = \frac{n_{o,est}}{n_{o,nom}} P_{i,est} + C. \tag{2.11}$$

Note that the slope of this fit is simply the ratio of the most likely value of the surface dust density $n_{o,est}$ to the nominal surface dust density assumed in computing $P_{i,est}$.

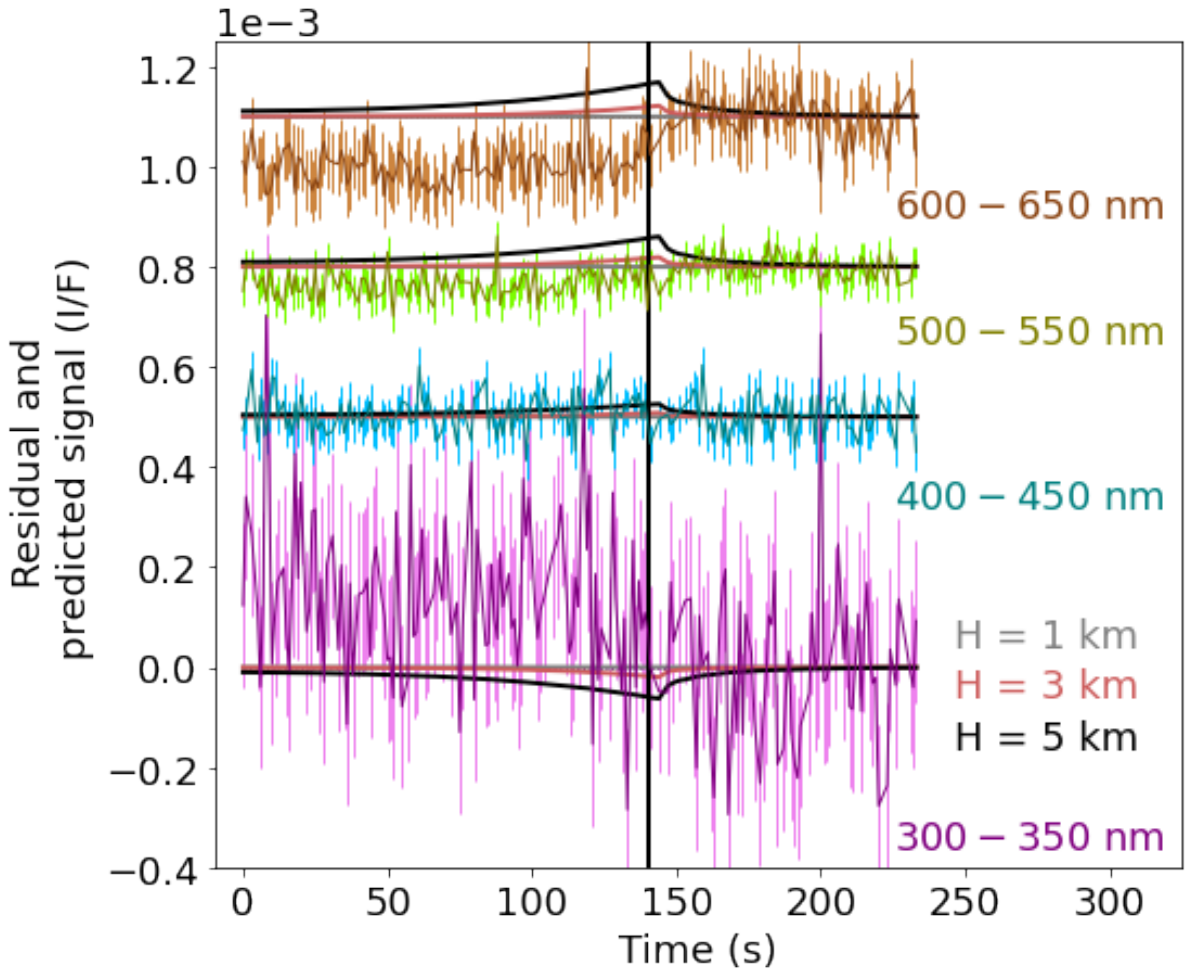

FIGURE 2.8: This figure shows the filtered residual I/F signal, $D_{i,est}(t)$ with error bars for Almost Limb activity 1840A at each wavelength range. The error bars are based on scatter in the data points. The vertical black line on the plot, denotes the point (t_V) when the telescope's line of view hits the Moon's surface. The signal predicted using the Fraunhofer model and the exponential density profile for a size distribution proportional to s^{-3}, nominal surface dust densities of 10^3 m^{-3} and for scale heights of 1, 3 and 5 km is plotted over the residual signal in grey, light coral and black, respectively. An offset has been added to view the signals distinctly. This plot is an example of the Almost Limb activity contaminated with Earthshine and hence is not included in calculating the upper limit on dust density.

We also take the weighted average of these slope and offset estimates from the different wavelength channels for each observation to obtain more precise estimates on these parameters, and propagate errors appropriately.

In principle, the offset C in the above equation should be equal to zero so long as there are no other sources of signal in the data. However, in practice we find that

Earthshine contaminates many of these observations, making them less suitable for deriving tight constraints on the dust populations. Figure 2.8 shows a clear example of this contamination. Since our filtering method forces the signal to be zero after the vertical line t_V, the filtering step causes significant offsets in the signals observed at earlier times. These signals do not vary with altitude like a low-altitude dust atmosphere signal should and so produce significant offsets in the trends of observed versus predicted signals (see Table A.2 inA.3). We force this offset C to zero for our estimates of dust density limit.

Fortunately, as New Earth approaches and the Earth-Moon phase angle increases, the illumination due to Earthshine on the surface of the Moon decreases. The corresponding values of Earth-Moon system are shown in the Table A.1 and Figure A.10 in A.3. The last three out of the 14 Almost Limb activities (1956A-1987A) are located beyond the Earthshine horizon. In addition, the preceding two Almost Limb activities (1918A and 1929A) were recorded at locations that have high Earth-Moon phase angle (129° and 141° respectively) and should receive negligible amounts of Earthshine.

We verify that Earthshine is negligible for the last five observations using the above linear model by checking that the wavelength-averaged value of C was consistent with zero for all of these five observations (see Table A.2 in A.3). We also computed the chi-squared statistics of a model where C was forced to be zero for all wavelengths for each of the observations and verified that the resulting individual estimates for $n_{o,est}$ from the last five measurements are all consistent with zero (see Table 2.2). This finding demonstrates that for these five observations there is no evidence for extraneous signals, and so we can use these five observations to place firm constraints on the low-altitude dust population. Note that these last few activities also probe the lowest altitudes, so they provide the tightest limits on the dust populations at low altitudes.

2.4 RESULTS AND DISCUSSION

Our final constraints on low-altitude dust populations are based on the weighted average of the estimates of $n_{o,est}$ from the Almost-Limb observations with negligible Earthshine contamination. These weighted averages are all comparable to their corresponding uncertainties, and so these constraints will mostly be provided as upper limits. These upper limits depend on both the assumed scale height and particle size distribution, and so these different assumptions will be considered separately below.

First, consider the limits derived assuming mono-disperse size distributions, since these reveal how our constraints depend on the assumed spherical-equivalent particle size. Figure 2.9 shows the 95% confidence interval limit on dust populations with scale height H of 1 km for mono-disperse size distributions. These limits tighten dramatically with increasing particle size up to around 0.3 μm, at which point they become much less sensitive to the assumed particle size. This demonstrates that the LADEE-UVS data provide the tightest constrains on the dust density for particles with equivalent radii bigger than 0.3 μm. This conclusion is reasonable, given the UVS data used in this analysis was obtained at wavelengths between 200 nm and 800 nm, and light is most efficiently scattered by particles that are at least as large as the light's wavelength (Van de Hulst, 1957).

Many of the prior works on Lunar dust reported limits on particles around 0.1 μm in size, which is also a reasonable size for a potential population of electrostatically-lofted grains. We therefore compare these prior observations with our corresponding limit for a mono-dispersed particle size distribution in Figure 2.10. The specific model limit shown in this figure correspond to a mono-disperse size distribution for an equivalent particle size of 0.1 μm and a scale height of 1 km, for which our upper limit on the surface dust density, $n_{o,est}$ is 3.1 $\times 10^4$ m^{-3}. The diagonal line shows the corresponding limit on the dust density as a function of altitude for this particular limit, and the green shaded area shows the allowed range of dust densities for this particular model.

Our limit on the surface dust density is of the same order of the estimates of surface dust density derived from Apollo 15 coronal photographs (Glenar *et al.*, 2011),

and is several orders of magnitude higher than limits set by more recent remote-sensing measurements (Feldman *et al.*, 2014; Glenar *et al.*, 2014). However, those measurements were insensitive to dust below altitudes of 10 km, and so our limit extends to lower altitudes. Furthermore, because we can consider much lower scale heights with the UVS data, at 10 km our limits become comparable to those earlier remote-sensing limits. Meanwhile, the LDEX instrument reported limits of order 100 m^{-3} in this same size range at altitudes between 3 km and 250 km (Szalay and Horányi, 2015). Our limit on the dust density at 3 km (1500 m^{-3}) is an order of magnitude above the LDEX limit. However, our constraints also apply to altitudes below 3 km (and even below 1 km), where LDEX was not able to observe.

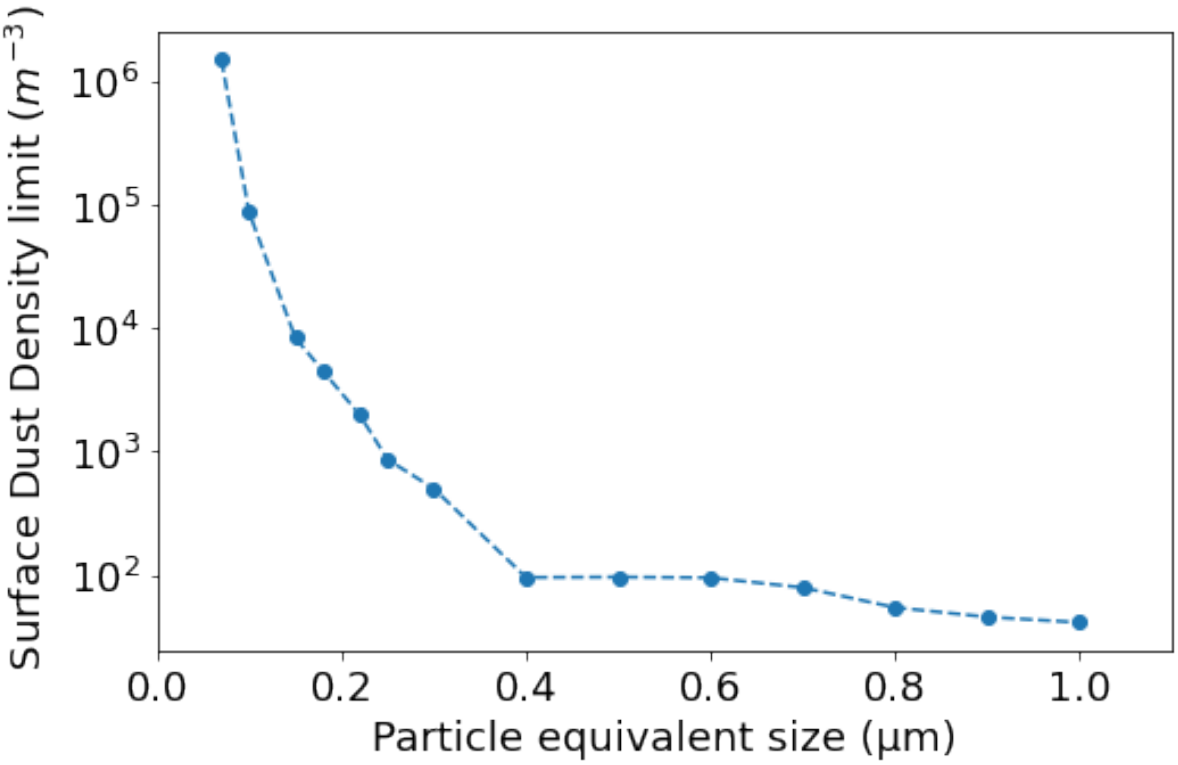

FIGURE 2.9: The upper limits on surface dust density, $n_{o,est}$ for mono-disperse size distribution with dust particles spherical-equivalent size (see Section 2.3) ranging from 0.07 to 1 μm derived for the 5 Almost-Limb observations in Table 2.2 with negligible Earthshine. The scale height H for all these values is 1 km. These limits are within the 95% confidence level, assuming a positive density value. In principle, this mono-disperse size distribution can be convolved to get upper limits for an arbitrary size distribution.

If we instead consider the populations with broader size distributions, our limits become much tighter. Table 2.3 shows our surface dust density limits obtained for the two different power-law size distributions (0.3 - 10 μm) and three different scale heights . There are two sets of values displayed in the table for the last three Almost Limb activities (1956A-1987A) with no Earthshine signal at all and the last five activities (1918A-1987A) with negligible Earthshine present. These limits on the surface dust density for particles larger than 0.3 μm are orders of magnitude above the values of 0.004 - 0.005 m^{-3} measured by the LDEX experiment for the same size range (Horányi *et al.*, 2015). However, the UVS Almost-Limb observations probe a very different population from the LDEX measurements. The dust population seen by LDEX has a very large scale height, and the contribution of this diffuse cloud to any signal measured in the UVS Almost-Limb data is negligible. However, LDEX could only measure dust densities down to altitudes of around 3 km and so was insensitive to any additional dust population that might be confined to low altitudes, such as the extreme tails of the very low-altitude Lunar Horizon Glow seen by the Surveyor landers. Our upper limits constrain this additional population of low-altitude dust, and for a scale height of 1 km these limits correspond to densities of around 140 m^{-3} near the surface, decreasing to values of around 0.006 m^{-3} (comparable to the LDEX measurements) at altitudes around 10 km.

The dust constraints from the LADEE-UVS observations are therefore consistent with prior limits. Furthermore, since these measurements are sensitive to material within just a few kilometers of the surface, they can help constrain both impact-generated and electrostatically lofted dust in a region that had not been well constrained by prior measurements.

2.5 CONCLUSIONS

In summary, this analysis of the LADEE Almost Limb observations provide new constraints on the dust density at low altitudes above the Moon's surface. Specifically, the upper limit on the surface dust density for a mono-dispersed size distribution for a particle size of 0.1 μm and a scale height of 1 km is 3.1 x 10^4 m^{-3}. The additional

population of low-altitude dust for a scale height of 1 km and a size distribution proportional to s^{-3} ranging from 0.3 to 10 μm (and s^{-4}) has an upper limit on dust density of around 140 m^{-3} (and 190 m^{-3}) closer to the surface which reduces to around 6 x 10^{-3} m^{-3} (and 9 x 10^{-3} m^{-3}) at altitudes reaching 10 km above the Moon's surface.

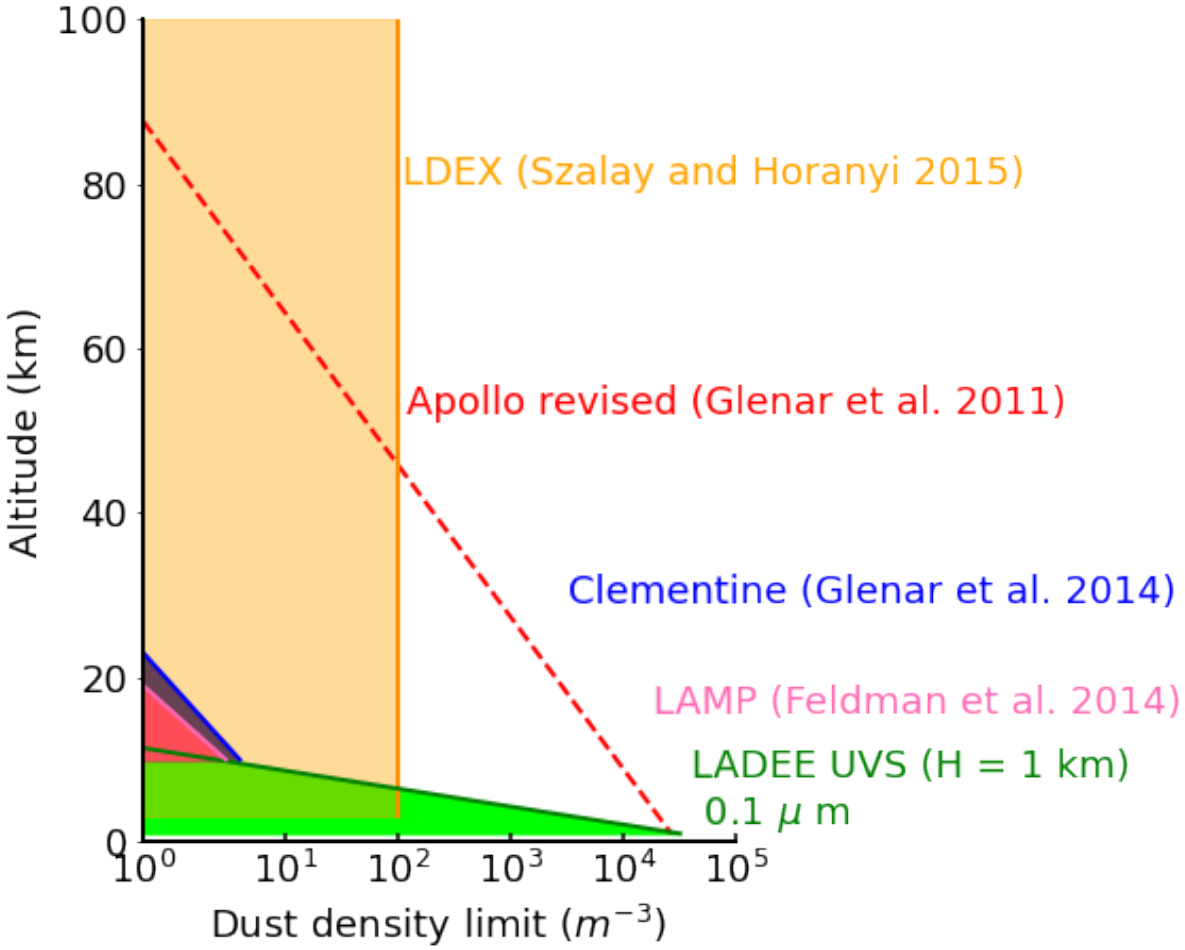

FIGURE 2.10: A comparison of the upper limits on dust density for particle size 0.1 μm as a function of altitude obtained from different measurements. This figure uses values for earlier data summarized in Szalay and Horányi (2015). The LADEE-UVS observation plotted here were computed using the last five Almost Limb activities which have low Earthshine signal and corresponds to a scale height H of 1 km. This value of dust density was calculated using a mono-disperse size distribution for a particle of size 0.1μm to facilitate comparison with previous limits. Note that the upper limit from the LADEE-UVS observations extend closer to the surface of Moon than prior limits.

2.6 ACKNOWLEDGMENTS

This work was supported by a Lunar Data Analysis Program Grant NNX15AV54G.

The primary data used in this analysis are all available on the Planetary Data System and is cataloged under Shirley (2014).

Datasets for this research are available in this in-text data citation references: https://doi.org/10.7923/xnej-7h18, [with license: https://creativecommons.org/licenses/by-nc-sa/4.0/, and the access restrictions: Creative Commons Attribution Non Commercial Share Alike 4.0 International] at the University of Idaho' Institutional repository.

The type of data files used in this analysis include .sav and .txt files. These files are read using .C (C code) and .ipynb (Python notebooks) code files. The processed data and the model data along with the codes and tools have been uploaded to the following: https://doi.org/10.7923/xnej-7h18

TABLE 2.2: Chi squared values and probabilities to exceed for the last five data sets for the size distribution s^{-3} and scale heights H = 1, 3 and 5 km.

Activity name	H = 1 km		H = 3 km		H = 5 km	
	Chi-square	Probability	Chi-square	Probability	Chi-square	Probability
1918A	0.05	82	0.75	39	1.18	28
1929A	0.13	72	0.41	52	1.03	31
1956A	0.06	81	0.04	84	0.02	89
1969A	0.42	52	0.08	78	0.38	54
1987A	1.82	18	1.30	25	1.31	25

TABLE 2.3: Dust density limits $n_{o,est}$ with their respective 1σ error bars.

Scale Height H (km)	Dust Density (m^{-3})			
	1956A-1987A		1918A-1987A	
	s^{-3}	s^{-4}	s^{-3}	s^{-4}
1	75.6±66.9	94.5±93.7	64.6±63.4	83.6±88.7
3	4.6 ± 10.6	3.3 ± 14.8	8.2±9.3	9.6±12.9
5	2.6 ± 6.1	2.1 ± 8.6	6.0±5.1	7.6±7.1

Error bars are defined as $1/(\sqrt{(\sum W_i)})$ where the weights W_i are the errors corresponding to each observation. These upper limits on surface dust density corresponding to two different size distributions: $\mathcal{N}(s,t) \propto s^{-3}$ and $\mathcal{N}(s,t) \propto s^{-4}$ and for scale heights of 1, 3 and 5 km. The limits of size range considered here are from 0.3 to 10 μm.

CHAPTER 3

New Insights into Variations in Enceladus Plume Particle Launch Velocities from Cassini-VIMS spectral data

---

H. Sharma, M. M. Hedman, and S. Vahidinia, "New Insights into Variations in Enceladus Plume Particle Launch Velocities from Cassini-VIMS Spectral Data." The Planetary Science Journal 4.6, 2023: 108.

This chapter begins the exploration into Enceladus plume population using Cassini-VIMS data. Dr. Hedman gathered the relevant data and calibrated it using standard pipelines. He wrote the IDL code to convert the VIMS data into cubes by re-projecting it into a cartesian space. The output of his code converted the data in a reliable shape and format that it could be used for further analysis. Dr. Hedman also devised the way to calculate the Equivalent Width derived from the cubes. I used Python code to reduce noise in this data and convert its altitude profile into velocity. Co-author Sanaz Vahidinia provided inputs and recommendations to improve the analysis.

3.1 ABSTRACT

Enceladus' plume consists mainly of a mixture of water vapor and solid ice particles that may originate from a subsurface ocean. The physical processes underlying Enceladus' plume particle dynamics are still being debated, and quantifying the particles' size distribution and launch velocities can help constrain these processes. Cassini's Visual and Infrared Mapping Spectrometer (VIMS) observed the Enceladus plume over a wavelength range of 0.9 μm to 5.0 μm for a significant fraction of Enceladus' orbital period on three dates in the summer of 2017. We find that the relative brightness of the plume on these different dates varies with wavelength, implying that the particle size distribution in the plume changes over time. These observations also enable us to study how the particles' launch velocities vary with time and observed wavelength. We find that the typical launch velocity of particles

remains between 140 ms^{-1} and 148 ms^{-1} at wavelengths between 1.2 μm and 3.7 μm. This may not be consistent with prior models where particles are only accelerated by interactions with the vent walls and gas, and could imply that mutual particle collisions close to the vent are more important than previously recognized.

3.2 INTRODUCTION

Enceladus emits a plume of water vapor and icy particles from a series of fissures located near its south pole (Spencer *et al.*, 2006; Dougherty *et al.*, 2006; Porco *et al.*, 2006). This plume can shed light on the processes operating inside Enceladus and the driving forces behind this geological activity. Measurements from several instruments onboard the Cassini spacecraft have been used to examine the plume's characteristics (Hansen *et al.*, 2006; Waite Jr *et al.*, 2006; Spahn *et al.*, 2006; Waite Jr *et al.*, 2009; Hedman *et al.*, 2009; Postberg *et al.*, 2009; Schenk *et al.*, 2018). At the same time, several different theoretical models have been developed to explain various aspects of the plume (Kieffer *et al.*, 2006; Hurford *et al.*, 2007; Schmidt *et al.*, 2008; Brilliantov *et al.*, 2008; Ingersoll and Pankine, 2010; Goldstein *et al.*, 2018; Kite and Rubin, 2016).

One important source of information about the physics behind Enceladus' plume is its variations over time periods ranging from days to years. Variations have been observed in plume's total particle output by both the Visual and Infrared Mapping Spectrometer (VIMS) instrument (Hedman *et al.*, 2013) and the Imaging Science Subsystem (ISS) cameras (Nimmo *et al.*, 2014; Porco *et al.*, 2014; Helfenstein and Porco, 2015; Ingersoll and Ewald, 2017; Ingersoll *et al.*, 2020) onboard the Cassini spacecraft. Most dramatically, both the ISS and VIMS data show that the plume's ice grain output varies systematically with the moon's orbital phase (the angular distance between the moon's current position and its orbital pericenter, equivalent to the moon's orbital mean anomaly). The primary maximum in the plume's brightness occurs close to orbital apocenter (orbital phase of 180°), where the particle output is roughly four times higher than it is at other points in its orbit. The most likely cause of the variations on orbital timescales are the tidal stresses experienced by Enceladus as it moves in its eccentric orbit around Saturn (Hurford *et al.*, 2007, 2012; Nimmo

et al., 2007; Smith-Konter and Pappalardo, 2008; Goldstein *et al*., 2018). Variations in the plume's activity on longer time scales were also seen by both VIMS (Hedman *et al*., 2013) and ISS (Ingersoll and Ewald, 2017; Porco *et al*., 2018; Ingersoll *et al*., 2020) which may be due to either a 5% decrease in the eccentricity of the orbit as part of a $\sim$ 11-year tidal cycle, or slow (and perhaps seasonal) changes in the clogging of vents (Porco *et al*., 2018; Ingersoll and Ewald, 2017). The plume is also prone to stochastic time variability on month-to-year timescales (Ingersoll *et al*., 2020) whose origins are still unclear and maybe due to individual jets turning on and off (Spitale and Porco, 2007; Ingersoll and Pankine, 2010; Hurford *et al*., 2012; Nimmo *et al*., 2014; Porco *et al*., 2014; Nakajima and Ingersoll, 2016; Teolis *et al*., 2017).

Compared to the relatively dramatic brightness variations listed above, trends in other plume particle properties like launch velocity and size distributions are more subtle. Hedman *et al*. (2009) found some differences in the spectral properties of the plume among the early VIMS observations, but these were of marginal statistical significance. Both Hedman *et al*. (2013) and Ingersoll and Ewald (2017) found small variations in the launch velocity with orbital phase. Nimmo *et al*. (2014) also reported an essentially constant scale height parameter for the plume. These observations are generally consistent with models where increasing crack width increases the total mass flow but has little effect on particle velocities (Ingersoll and Pankine, 2010).

This paper aims to quantify variations in the plume's properties using spectral data obtained by the Visual and Infrared Mapping Spectrometer (VIMS) onboard the Cassini spacecraft (Brown *et al*., 2004). VIMS can provide new information about trends in the particle size and velocity distribution over time because it was able to observe the plume over a broad range of near-infrared wavelengths. More specifically, we will examine VIMS data obtained on three dates – June 18th, Aug 2nd and Aug 28th, 2017. There is a clear maximum in the plume's brightness around apoapsis in the VIMS data on all three of these dates (see Figure 3.1), consistent with previous ISS results (Ingersoll *et al*., 2020). The VIMS observations at short wavelengths also show the same variations in the plume's brightness among the three orbits, where the brightness increases from June 18th to Aug 2nd and decreases again on Aug 28th as reported by Ingersoll *et al*. (2020). However, the VIMS data show that these variations

in plume brightness across the three different orbits being studied here are not the same at all wavelengths, suggesting the plume's particle size distribution also varied over this time period of 3 months. In addition, we find that the launch velocities of the plume particles do not vary as much with wavelength as published models would predict (Schmidt *et al.*, 2008; Degruyter and Manga, 2011) but see Schmidt (2014) for modified models that may be consistent with these observations.

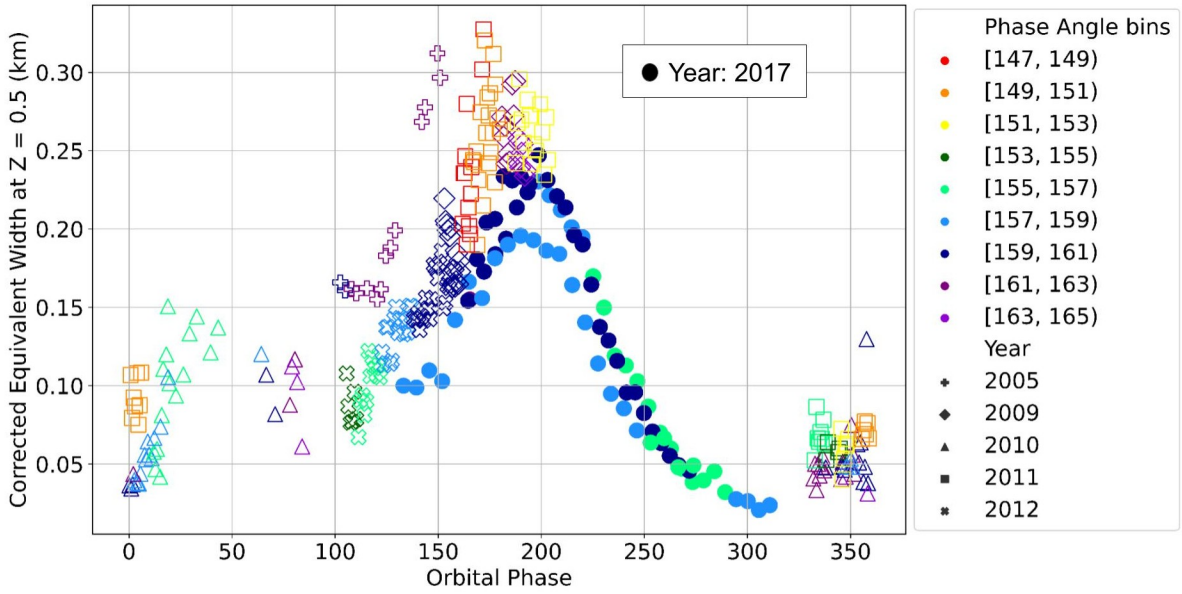

FIGURE 3.1: Overview of variations in the plume's brightness (expressed in terms of the corrected Equivalent Width at a wavelength of 0.88 - 1.56 μm and an altitude of 85 km, see text for details) as a function of orbital phase. This figure compares the plume brightness estimates derived in this study (shown as solid dots) with previously published estimates from earlier in the Cassini mission (shown as empty symbols Hedman *et al.*, 2013). Note that the corrected Equivalent Width used in this particular plot includes the phase angle correction described in Hedman *et al.* (2013) in order to facilitate comparisons among the different data sets.

Our methods for extracting information about the plume from the VIMS data are described in Section 3.3. This analysis begins by converting the raw VIMS data to estimates of the plume's spectra at various distances from the south pole. These spectra are then converted into constraints on the plume's overall intensity and the particles' typical launch velocity assuming the particles follow ballistic trajectories. The results of these calculations are presented in Section 3.4. Finally, in Section 3.5 we further discuss the implication of the observed spectral trends in the brightness and

typical launch velocity of particles. Note that this paper is focused on documenting the spectral trends in these data. Detailed spectral modeling of these trends will be the subject of future work.

3.3 METHODS

This section describes the steps by which the relevant VIMS data are reduced into standardized estimates of the plume brightness and typical launch velocity at a range of wavelengths. Section 3.3.1 describes the geometry and calibration of the VIMS observations for the 3 dates in 2017 being studied here. Section 3.3.2 details how these data are processed to obtain high signal-to-noise spectra of the plume at different altitudes. Finally, Section 3.3.3 shows how these data are fit to obtain the brightness and typical launch velocity at different wavelengths.

3.3.1 *Data*

The Visual and Infrared Mapping Spectrometer (VIMS) was an imaging spectrometer onboard the Cassini spacecraft that covered the 0.3 μm - 5.1 μm wavelength range using 352 spectral channels. This instrument could view an array of up to 64 x 64 locations in the sky to produce a spectral-spatial image "cube" (Brown *et al.*, 2004). In this paper, we focus exclusively on the infrared spectra obtained by the VIMS-IR channel that measured the brightness in 256 wavelength bands between 0.88 μm and 5.1 μm with a typical spectral resolution of 0.016 μm. Further, we have removed the data corresponding to spectral channels at 1.23 μm (channel 118) and at 4.75 μm (channel 330) as they contain null values due to being hot pixels on the detector (Clark *et al.*, 2018) and exclude data beyond 4.0 μm because the signal-to-noise ratio is significantly lower at these wavelengths. This reduces the number of spectral channels considered here from 256 to 186.

This investigation examines VIMS observations of Enceladus from 3 different Cassini orbits (designated 279, 286 and 290) corresponding to 3 days in 2017 - June 18th, Aug 2nd and Aug 28th. During all three of these days, VIMS viewed Enceladus from similarly high phase angles (156° - 162°) over a similar range of the moon's

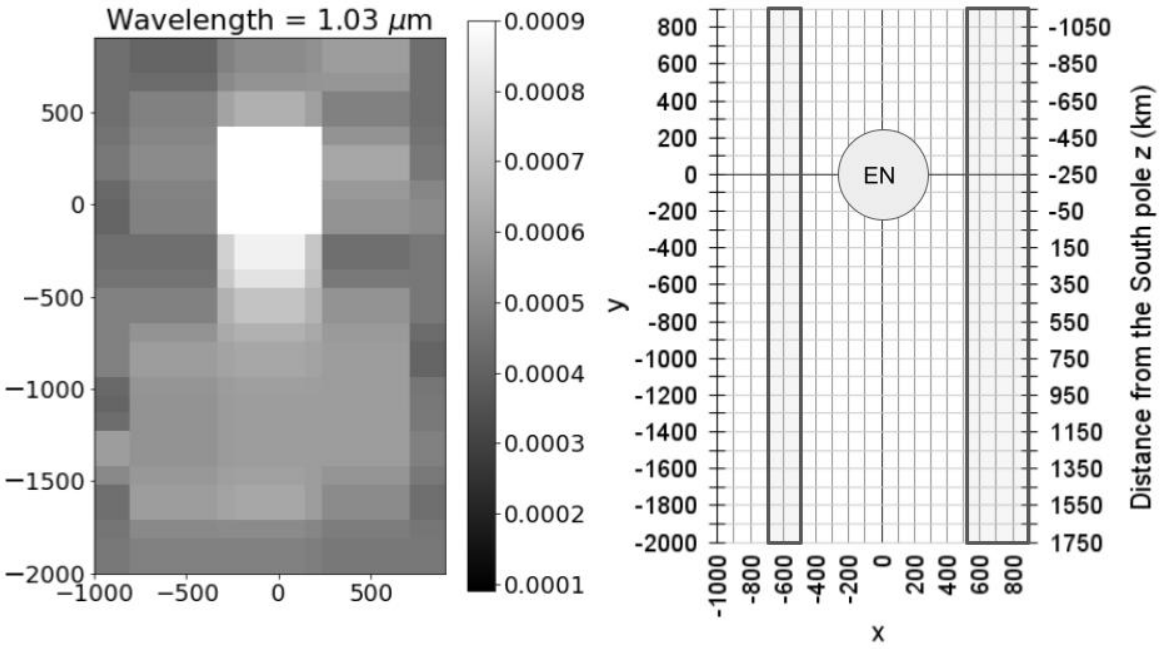

FIGURE 3.2: The spatial geometry of the re-projected VIMS cubes. On the left is a sample image of Enceladus and its plume at a wavelength of 1.03 μm derived from a single re-projected cube (CM_1876456410_1) obtained at an orbital phase of 200° during Orbit no. 279 on June 18th. The sample image shows individual pixels and the data has been over sampled to obtain brightness values with a resolution of 100 km across both x and y co-ordinates. On the right is the geometry of the re-projected VIMS cubes. The re-projected data plane is defined using cartesian co-ordinates [x, y], with Enceladus at the center at [0, 0] and the negative y axis is aligned with the moon's spin axis. The left vertical axis and the horizontal axis show the [x, y] coordinates for the cube. For the right vertical axis of the figure the y co-ordinate has been converted into altitude above the Enceladus' south pole ($z = -(250 + y)$ in km). The outlined regions on either side correspond to the region used to calculate background signal levels.

orbital phase. The parameters for these three observations are listed in Table 3.1. Note that all three observations cover orbital phases around 180°, when the plume is most active, and are at high enough phase angles for the plume signals to be clearly detectable.

The raw data in each cube are converted into I/F values (a standard measure of reflectance) using standard calibration routines (the specific calibration being RC19 (Clark *et al.*, 2018)). To facilitate comparisons among the observations, the observation geometry for each cube is computed using the appropriate SPICE kernels, and the

brightness data are re-projected onto a regular array of cartesian co-ordinates [x, y] containing the moon's spin axis. In these coordinates the center of Enceladus is located at [0, 0] and the negative y-axis is aligned with Enceladus' spin axis. In the resulting maps x ranges from -1000 km to 900 km and y ranges from -2000 km to 900 km. Both coordinates are sampled every 100 km. Figure 3.2 shows the extent of the co-ordinates x and y. We also use the y coordinate to compute the distance from Enceladus' south pole (i.e. the plume's altitude) as $z = -(250 + y)$ in km.

3.3.2 *Extracting Brightness Spectra at different altitudes and times*

The first step in extracting plume spectra from these cubes is to remove cubes that had instrumental artifacts that made their spectra discrepant from the rest of the observation. We identified these anomalous cubes by first averaging the brightness in the region of Enceladus' plume at each wavelength over all values of x from -400 km to 400 km and all values of y from -300 km and beyond. A median filter is then applied to this list of average brightness values at each wavelength. Any image/cube that lies outside the 3σ range of the median brightness was flagged as an outlier for that spectral channel. We then compared the outlier list of each spectral channel and if a cube appeared as an outlier for over 35 spectral channels it was regarded as unreliable and so removed from further consideration. This procedure led to the removal of 22 cubes from the data on June 18th/Orbit no. 279, 24 cubes from the data on Aug 2nd/Orbit no. 286 and 11 cubes from the data on Aug 28th/Orbit no. 290 (see Appendix B.1 for an explicit list of these cubes).

After removing the outliers highlighted across orbital phase and wavelength and before applying background removal techniques the cubes are co-added. Spectra derived from the individual remaining cubes had low signal-to-noise, so we averaged together sets of 10 cubes to improve the signal-to-noise in the spectra. Note that each of these sets of cubes corresponds to a relatively narrow range of orbital phases, so this averaging does not significantly affect our ability to quantify variations in plume activity. Table 3.1 shows the range of cubes corresponding to each orbit, the number of cubes before binning and after binning sets of 10 cubes each.

From each of these co-added cubes, we derive plume spectra as a function of altitude. Preliminary investigations of these data indicated that the majority of the plume signal exists between x = -400 km and x = 400 km. Any signal in the range x < -400 km and x > 400 km is therefore primarily due to background signals from the instrument or the E ring. We estimated this background by fitting the brightness values for -700 km < x < -400 km and x > 400 km at each value of y to a linear trend. Note that the brightness beyond x < -700 km is not included in this linear fit because this region appears to be more strongly contaminated by instrumental backgrounds than the rest of the re-projected image at certain wavelengths.

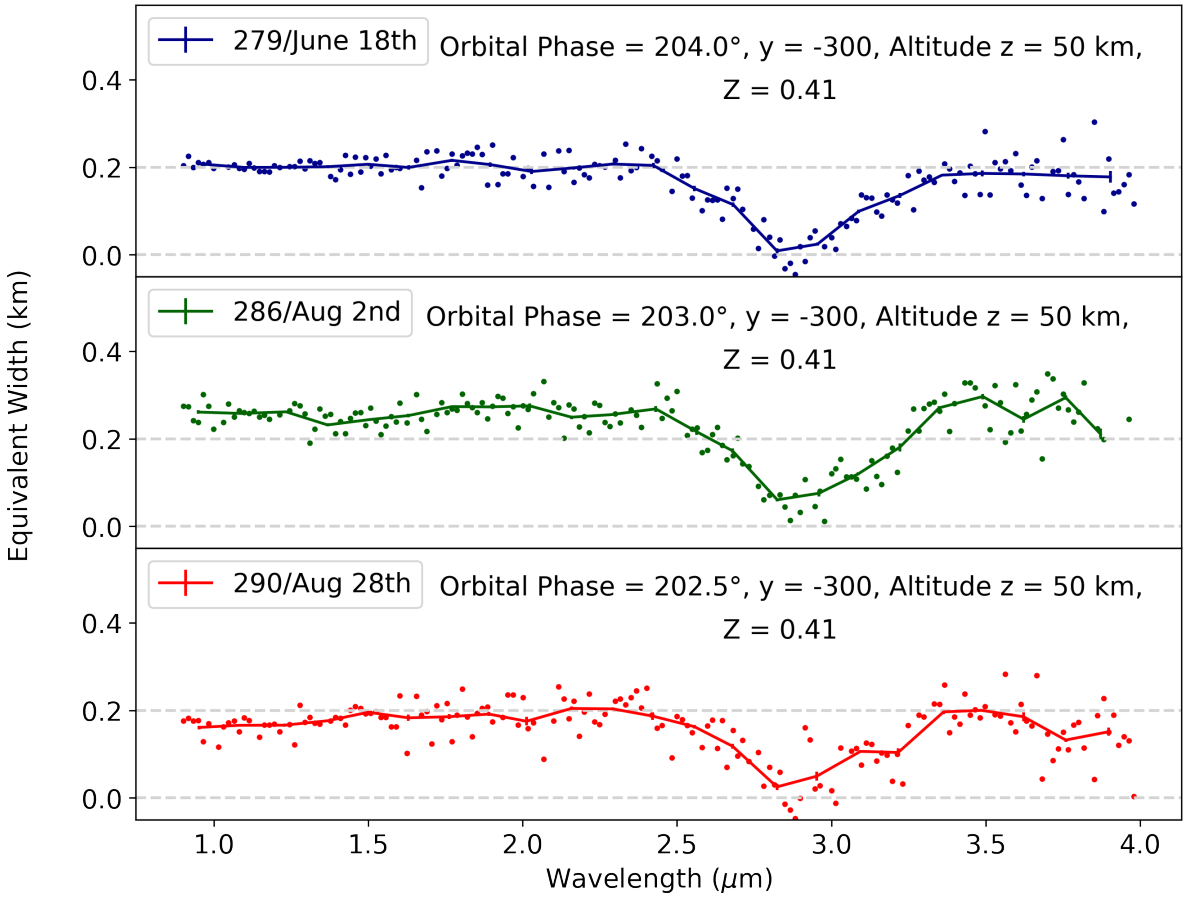

FIGURE 3.3: Example Enceladus plume spectra, showing the plume's Equivalent Width (in km, see sub-section 3.3.2) versus wavelength (in μm) at similar orbital phases for all three orbits. An orbital phase close to 200° is chosen as the signal is strongest closer to the plume maxima at apoapsis. The points show the Equivalent Widths for individual spectral channels (after removing outliers before 2.5 μm and after 3.3 μm) and the line plot with error bars shows the data after averaging each spectrum over 8 wavelength channels.

After removing the background across all values of x we define the plume's Equivalent Width at each y corresponding to an altitude z such that $z = -(250 + y)$ in km as the total integrated brightness in a horizontal slice through the plume (Hedman *et al.*, 2013). The Equivalent Width is calculated as the sum of the signal across x dimension multiplied with the step width (that is, 100 km). This yields the plume's Equivalent Width for all y between -2000 km and -300 km, or altitudes z ranging from 50 km to 1750 km. This process is carried out on each binned cube for all wavelength channels of each of the 3 dates.

Figure 3.3 shows example plume spectra from 0.9 μm to 4.0 μm obtained from cubes obtained close to peak of Enceladus' activity and at low altitudes. Each of these spectra has a clear dip around 3 μm corresponding to the fundamental water-ice absorption band (Mastrapa *et al.*, 2009). While the signal-to-noise of these spectra is reasonably good, for other orbital phases and altitudes it is still rather low and so to better quantify relevant spectral trends we further average these spectra over wavelength.

For this analysis we focus primarily on wavelength ranges outside the water-ice absorption band. Hence we first apply a median filter to find outliers before 2.5 μm and after 3.3 μm range. More specifically, we compute the median of the signal before 2.5 μm and flag outliers beyond the range of 1.5 times the standard deviation of all the points in this range, and then do the same for the signals beyond 3.3 μm range. This threshold value of 1.5σ was chosen because it was found to remove clear outliers based on visual inspection of selected spectra[2] After flagging these general outliers, we compute the average and error on the mean signal in bins of 8 wavelength channels each. These averages and errors are computed after excluding both the outliers flagged previously and any data points that are beyond the 2σ range from the median of the 8 wavelength channels that are being averaged together. This leaves us with 23 averaged wavelength values, which are shown as the connected lines in Figure 3.3. Finally, we compute the weighted average Equivalent Width over four

[2]These particular parameters were chosen after trying a range of values and visually inspecting the results. Figure 4.2 in Chapter 4 shows an example spectrum with outlier points identified with these techniques highlighted in red. This plot shows that the removed points can reasonably be considered outliers and their removal does not substantially change the signal.

wavelengths each and obtain the plume's output centered at 1.2 μm, 1.7 μm, 2.2 μm and 3.7 μm. This last averaging step improves the signal to noise ratio considerably, and is particularly useful for the calculations of overall plume output and typical launch velocity described in the next subsection.

3.3.3 *Quantifying trends with altitude and orbital phase/time*

In order to better quantify the trends in the brightness with time and altitude, we use the same basic parametrization as Hedman *et al*. (2013). That work defined a parameter $Z = [z/(r_E + z)]^{1/2}$ where r_E = 250 km is the radius of Enceladus and z is the plume's altitude. This parameter is useful because for low-optical-depth systems like the plume, it is reasonable to assume that Enceladus' gravity is the dominant force acting on the particles and the particle and gas density are so low that the particles follow purely ballistic trajectories. In this limit, the particle launch velocity v is directly related to the altitude it reaches z:

$$v = v_{esc}\left[\frac{z}{r_E + z}\right]^{1/2} = v_{esc} * Z \tag{3.1}$$

where v_{esc} = 240 ms^{-1} is the escape velocity on Enceladus. Thus for a population of particles, trends in the plume's brightness with Z reflect trends in the particles' launch velocity. Hedman *et al*. (2013) found that at wavelengths around 1 μm the relationship between Equivalent Width and Z was roughly linear with a negative slope.

Figure 3.4 shows that the approximately linear relationship between the plume's integrated brightness and the Z parameter observed by Hedman *et al*. (2013) also holds for the VIMS observations in 2017 over all the observed wavelengths. We therefore fit a linear trend to the plume's EW profile versus Z in Figure 3.4 at altitudes between 50 km and 450 km i.e., Z between 0.41 and 0.8 and launch velocity v between 100 ms^{-1} and 200 ms^{-1}.

The parameters for this linear fit are then used to calculate two quantities. One parameter is the Equivalent Width (a measure of the plume's total brightness) at a reference altitude of z = 85 km (Z = 0.5; v = 120 ms^{-1}) calculated through

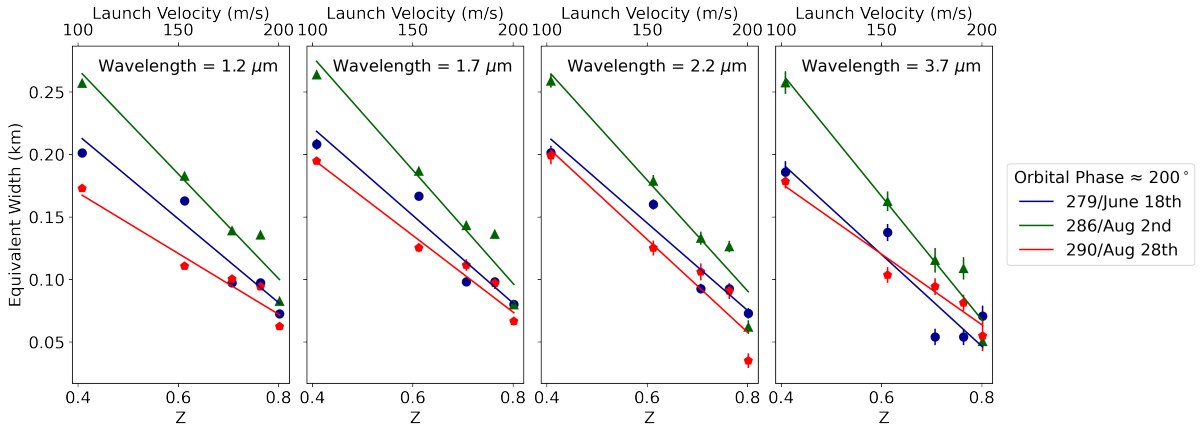

FIGURE 3.4: The integrated brightness of the plume (Equivalent Width or EW) as a function of the parameter Z $(=[z/(r_E+z)]^{1/2}$ where r_E = 250 km is the radius of Enceladus and z the plume's altitude) and launch velocity v (calculated using equation 3.1). The Equivalent Width for the three different dates in 2017 - Orbit no. 279/June 18th, Orbit no. 286/Aug 2nd and Orbit no. 290/Aug 28th are plotted (in blue, green and red respectively) at similar orbital phase value of $\simeq 200^\circ$ and 4 different wavelengths. The Equivalent Width is fit to a linear function of Z. Note the brightness of the plume is higher for the observation on Aug 2nd (in green) than on the other dates.

interpolation using the slope and the y-intercept, while the other is a critical velocity v_c, which is the value of v where the linear trend in the Equivalent Width would pass through zero.

Note that the critical velocity defined above involves an extrapolation of the linear fit into regions where it is not necessarily appropriate since this parameter often exceeds the escape velocity of Enceladus v_{esc}. Hence, we instead use this parameter to compute a quantity called the typical launch velocity $v_{typical}$. This corresponds to the weighted average of launch velocities of the particles visible between altitudes of 50 km and 450 km:

$$v_{typical} = \frac{\int_{v_{min}}^{v_{max}} n(v) v \, dv}{\int_{v_{min}}^{v_{max}} n(v) \, dv} \tag{3.2}$$

where v_{min} = 100 ms^{-1} and v_{max} = 200 ms^{-1} are the minimum and maximum launch velocity of particles in the range of altitude 50 km to 450 km, and $n(v)$ is the launch velocity distribution of the particles. For this analysis, we assume $n(v) \propto (1 - v/v_c)$,

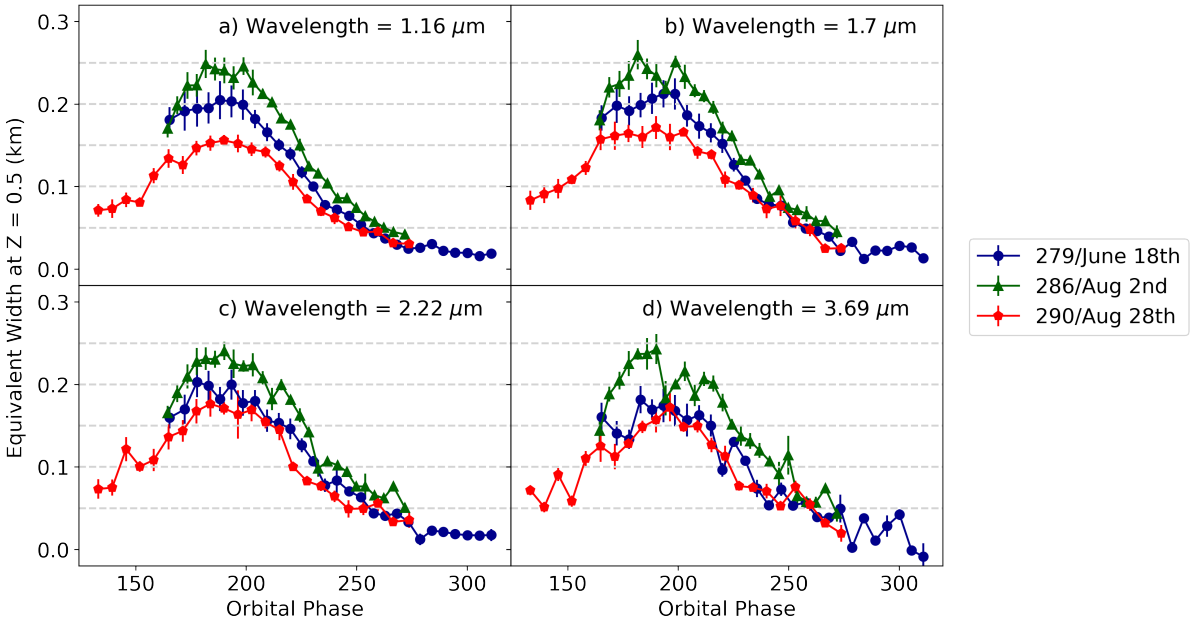

FIGURE 3.5: The plume's Equivalent Width at $Z = 0.5$ (altitude $z = 85$ km) as a function of orbital phase for the three dates and four different wavelength values. The plume's maximum brightness around the orbital phase of 180° is consistent at all wavelengths. Additionally, note that the brightness of the plume was higher on Aug 2nd than it was on June 18th or Aug 28th in 2017 at all wavelengths.

consistent with the observed linear trend between Equivalent Width and launch velocity shown in Figure 3.4. Using these values, Equation 3.2 can be reduced to:

$$v_{typical} = \frac{\left[\frac{v_{max}^2}{2} - \frac{v_{max}^3}{3v_c}\right] - \left[\frac{v_{min}^2}{2} - \frac{v_{min}^3}{3v_c}\right]}{\left[v_{max} - \frac{v_{max}^2}{2v_c}\right] - \left[v_{min} - \frac{v_{min}^2}{2v_c}\right]} \tag{3.3}$$

Using the above equations, the typical launch velocity is calculated for each binned cube. Since the trends among the different panels in Figure 3.4 are nearly the same, the typical launch velocity should not depend strongly on wavelength.

3.4 RESULTS

Figures 3.5 and 3.6 show the plume's Equivalent Width at $Z = 0.5$ as a function of orbital phase for all three dates (June 18th, Aug 2nd and Aug 28th) at 4 different

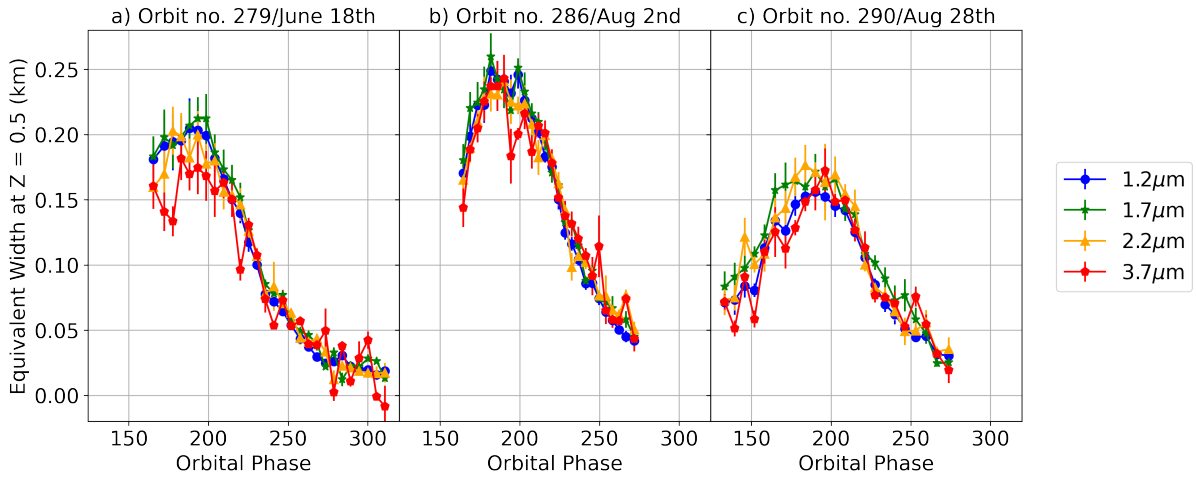

FIGURE 3.6: The plume's Equivalent Width at $Z = 0.5$ (altitude $z = 85$ km, same as Figure 3.5) as a function of orbital phase, grouped by the Orbit no./Date instead of wavelength. Note that on Aug 2nd the brightness variations are nearly identical at all wavelengths, spectral trends in the plume's brightness can be seen in both the June 18 and Aug 28 data at orbital phases below 180°.

wavelengths. In addition, Figure 3.7 shows the differences in the Equivalent Width at different wavelengths for each of the three dates. The Equivalent Width parameter provides an estimate of the plume's overall brightness and therefore the moon's overall activity level. All three observations covered the range of orbital phase 160° to 270°. The plume's maximum brightness is consistently around the orbital phase of 180° for all these observations, regardless of wavelength. This consistent observation confirms that the plume's ice-particle output is highest when the satellite is furthest from Saturn, consistent with prior analysis of ISS and VIMS plume observations also shown in Figure 3.1 (Hedman *et al.*, 2013; Nimmo *et al.*, 2014; Ingersoll and Ewald, 2017).

Closer comparisons of these data with the ISS data reported in Ingersoll *et al.* (2020) not only confirm some of the variations documented in that work, but also highlight novel spectral trends. In Figure 3.5 at wavelengths of 1.2 μm the trends with time and orbital phase among the observations are similar to those seen at visible wavelengths (Ingersoll *et al.*, 2020), with the plume being brighter on August 2nd than it was on June 18th and August 28th, indicating the overall activity level in the plume rose and fell during the 10-week interval of these observations. However,

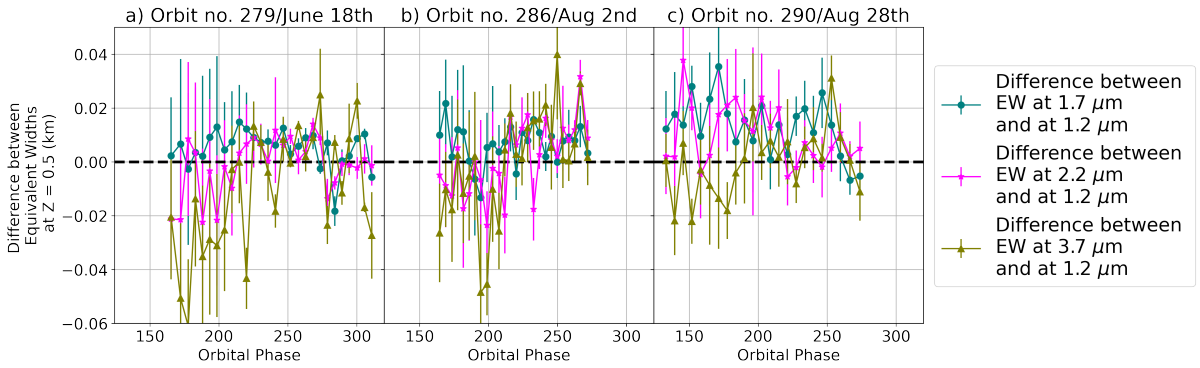

FIGURE 3.7: The difference in plume's Equivalent Width at different wavelengths and at $Z = 0.5$ (altitude $z = 85$ km) as a function of orbital phase, grouped by the Orbit no./Date. Note that on Aug 2nd the brightness variations are nearly identical at all wavelengths, spectral trends in the plume's brightness can be seen in both the June 18 and Aug 28 data at orbital phases below 180°.

the relative brightness of the plume on June 18th and August 28th also varies with wavelength (see also Figure 3.6 and 3.7). At short wavelengths of 1.2 μm and 1.7 μm shown in panels a) and b) of Figure 3.5, the plume is significantly brighter on June 18th (in blue) than it was on August 28th (in red), which is consistent with prior analysis of the imaging data (Ingersoll *et al.*, 2020). However at a longer wavelengths of 3.7 μm in panel d) of Figure 3.5 the plume's brightness on these two dates (in blue and red) are nearly identical. See Section 3.5 for further details on this variation.

Figure 3.8 shows the typical launch velocity of the plume particles derived from the same linear fits described above as a function of orbital phase for the same four average wavelength values and three observation dates. The typical launch velocity plotted across orbital phase in Figure 3.8 are averaged using the inverse of variance as weights. The weighted averages of these typical launch velocities across four wavelength ranges and 5 orbital phase values are also provided in Table 3.2. Unlike the dramatic variations seen in the plume's brightness, this parameter depends much less on orbital phase, date or wavelength. In general, the typical launch velocity increases with increasing orbital phase between 160° and 230°. The spectral variations in the typical launch velocity are subtle, with the values at 3.7μm being only about 10 m s^{-1} less than the values at 1.2 μm (see Table 3.2). This is consistent with Figure 3.4 where the linear trends for each Orbit no./Date are similar for all the

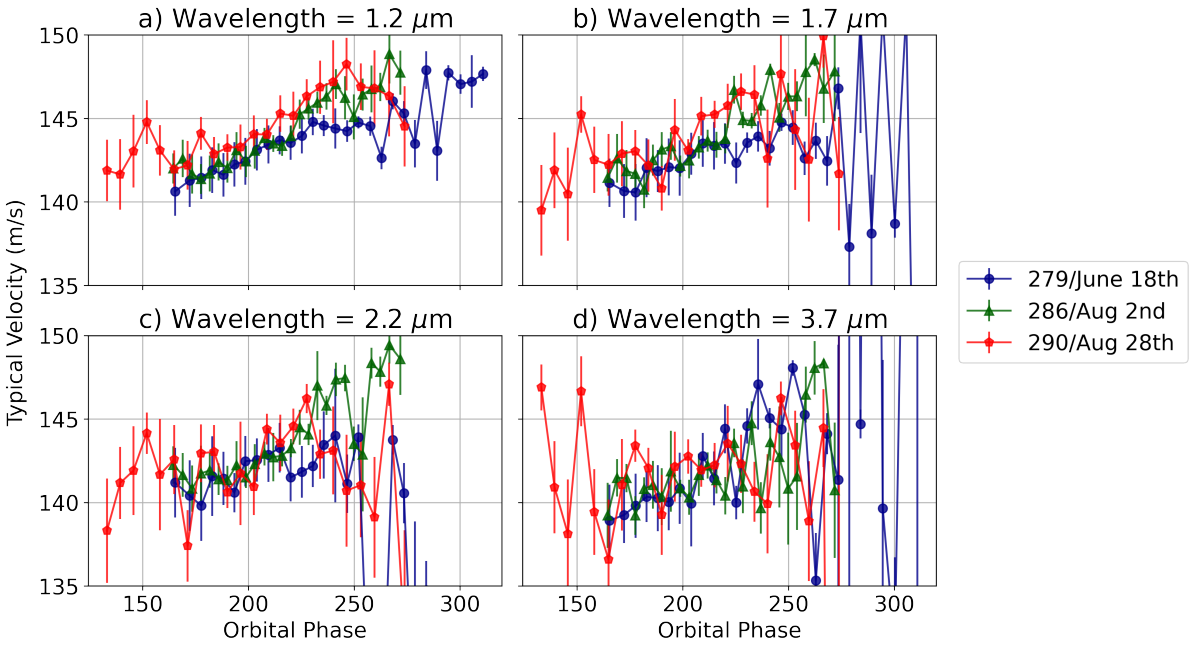

FIGURE 3.8: Typical launch velocity (in ms^{-1}) for three different orbits derived using equation 3.3 as a function of orbital phase. Note that the typical launch velocity is higher on Aug 28th than June 18th or Aug 2nd at lower wavelengths of 1.2 μm. The typical launch velocity also generally increases with orbital phase. Also note the variations in the typical launch velocity with wavelength are relatively small.

different wavelengths. Also note that at 1.2 μm the typical launch velocity is slightly higher on Aug 28th than on June 18th or Aug 2nd.

3.5 DISCUSSION

Figures 3.5 - 3.7 show several interesting trends with orbital phase, time, and particularly wavelength. Since the wavelength trends are the most unique aspect of these new VIMS data, we will focus primarily on these aspects of the data here. In general, particles of different sizes scatter different wavelengths of light with different efficiencies, so the spectral trends provide information about trends with particle size. Detailed modeling of these spectra will be the subject of a future work, but we can already highlight some interesting trends with wavelength that likely reflect trends with particle size. VIMS data are observed at high phase angles, where particles scatter light most efficiently at wavelength comparable to the particle radius (Van de

Hulst, 1957; Hedman *et al.*, 2009). Hence larger particles contribute more to the plume's brightness at longer wavelengths. In other words, larger particles tend to produce a spectrum with a redder slope.

Variations in the plume spectra indicative of variations in the particle size distribution are most easily seen in Figure 3.7. One June 18th, the olive green curve is more negative (brightness decreases from 1.7 μm to 3.7 μm) hinting at a higher number of small particles in the plume on that date. While on Aug 28th both the magenta and teal curves are above the zero line (brightness increases from 1.2 to 1.7 μm and 2.2 μm). This variation is also visible in the spectra shown in Figure 3.3, where the Aug 28th data shows a redder slope than the earlier data on June 18th and Aug 2nd. This indicates that the plume contained a higher fraction of larger particles on Aug 28th than on June 18th.

These changes in plume's spectra may provide additional clues about what happened to produce the brightness changes across these three dates. One potential explanation for these changes is that they reflect localized sources turning on and off. Individual jets have been observed to turn on and off over time scales that are not explicable by simple tidal models (Porco *et al.*, 2014; Spitale *et al.*, 2017, 2020; Ingersoll *et al.*, 2020). The maximum in plume brightness might be due to a highly collimated jet only seen on Aug 2nd (Ingersoll *et al.*, 2020). However, this change in plume activity could also be explained by subsequent opening of new channels or choking of conduits by ice deposition in the near-surface (Spencer *et al.*, 2018; Ingersoll and Pankine, 2010) Changes in the particle size distribution as a whole from one month to another could shed light on the cause of this stochastic variability in the plume such as how these variations reflect changes in vent conditions. We plan to further explore the particle size variations in the plume using Mie scattering in our future work.

Figure 3.8 shows that for all three orbits, the typical launch velocity of particles increases with orbital phase after the satellite passes the plume maxima near apocenter. This increase in the velocity with orbital phase holds true for all wavelengths and is consistent with prior results (Hedman *et al.*, 2013; Ingersoll *et al.*, 2020). This observation suggests an inverse relation between the particle mass

flux and ejection velocity at least in the region beyond the apoapsis. Another key observation is the typical launch velocity is higher on Aug 28th than on June 18th and Aug 2nd at wavelengths of 1.2 μm while the particle mass flux reflected by the Equivalent Width in Figure 3.5 is lowest. This observation further alludes to a complementary change in particle mass flux and typical launch velocity at least at lower wavelength of 1.2 μm. One possible explanation for this observation is the narrowing of vents due to tidal stresses as the satellite cross its apocenter might increase the flow speed while decreasing the mass flux (but see Nimmo *et al*., 2014, for potential complications with this idea).

Interestingly, the launch velocity of particles in Table 3.2 and Figure 3.8 shows only a slight decrease as wavelength increases. This observation is surprising because previously published models by Schmidt *et al*. (2008) predict substantial variations of launch velocity with particle size. According to these models, repeated collisions with the walls of the conduit reduce the particle velocity relative to the gas. Degruyter and Manga (2011) also modeled the particle acceleration within the conduit and their ballistic transport once they exited the vent using the gas flow model of Ingersoll and Pankine (2010) and the Schmidt *et al*. (2008)'s collision model and similarly found that larger particles achieve lower exit speeds. Using Schmidt *et al*. (2008)'s collision model for a gas density of 4.85 gm^{-3} and gas speed of 500 ms^{-1} and a collision length of 0.1 m, a large fractional reduction of 0.98 is expected in the typical particle velocity as size increases from 1.2 μm to 3.7 μm. By contrast, the typical launch velocities in Figure 3.8 shows a fractional reduction of only 0.01 - 0.16 as wavelength increases from 1.2 μm to 3.7 μm which is 6 times lower than predicted by previous models of particle velocities. While the plume's brightness at wavelength is due to particles with a range of sizes, there is still a notable difference between the expected reduction and the observed reduction in launch velocities of the particles.

This finding is also consistent with some of the earlier spectral analysis of the Enceladus plume. Hedman *et al*. (2009) determined the relative number of particles of radii 1, 2 and 3 μm versus height in early VIMS plume observations, which were in turn converted into velocity distribution of particles. Data obtained at orbital phases around 90° - 120° indicated that the number density of larger particles of radius 3 μm

falls faster than the smaller particles of radius 1 μm implying a typical lower launch velocity for 3 μm particles which was roughly consistent with the Schmidt *et al*. (2008). However, the velocity distribution for the data obtained closest to apopasis in Figure 6 of that paper is not significantly steeper for larger particle sizes for most velocities, indicating the typical launch velocity of larger particles does not decrease steeply, which is more consistent with these observations.

One possible explanation for this surprisingly subtle reduction in particle velocity with increasing particle size is that the vent parameters are different from what was assumed in Schmidt *et al*. (2008) model. Changing these parameters such that the critical grain radius is larger could result in a less steep dependence of ejection velocity on grain sizes in the range from sub-microns to a few microns (Schmidt, 2014; Postberg *et al*., 2009, 2011b). Another possible explanation is that particle-particle interactions at the vent are more common than previously thought. Unlike collisions with the walls of the conduit (that produce trends in particle velocity with size (Schmidt *et al*., 2008)), particle-particle collisions would cause grains of different sizes to have similar velocity distributions. Both particle-wall and particle-particle collisions are most important near the vent where the gas density rapidly declines, and the particles become partially decoupled from the gas (so that they are launched at much lower velocities than the gas) (Goldstein *et al*., 2018). Assuming a gas density and a particle density of 10^{23} m^{-3} and 2.1×10^{10} m^{-3} respectively (Yeoh *et al*., 2017) at the end of the conduit, the mean free path for particle-gas collision is of the order of 10^{-13} m while for particle-particle collision is 1 m. The mean free path for particle-particle collisions is comparable to the measured vent sizes on the south pole of Enceladus. Goguen *et al*. (2013) estimated a fissure width of 9 m based on near-IR thermal emission spectra acquired by VIMS and Yeoh *et al*. (2015) estimated vent diameters of up to 2.8 m. Hence particle-particle interactions could occur at a high enough rate to affect particle velocities, which has not been taken into account in the current models.

We plan to model the observed spectral trends to obtain quantitative constraints on the particle size distribution at different altitudes and times. This information should further our understanding of the conditions within the vents.

ACKNOWLEDGEMENTS

We would like to acknowledge J.N. Cuzzi for helpful conversations. This particular work was supported by a Cassini Data Analysis Program Grant 80NSSC18K1071.

TABLE 3.1: The three data sets studied in this paper.

Orbit no. Date	Orbital Phase[c]	Phase angle[d]	Range[a] (km)	Longitude[b]	Cubes	No. of cubes before binning	No. of cubes after binning
279/June 18th, 2017	162 - 319°	156 - 161°	8,37,300 - 10,93,300	11 - 164°	CM_1876443559_1 - CM_1876495215_1	302	28
286/Aug 2nd, 2017	162 - 286°	159 - 161°	8,22,700 - 10,63,000	29 - 150°	CM_1880355368_1 - CM_1880396071_6	293	26
290/Aug 28th, 2017	130 - 281°	156 - 158°	8,68,600 - 11,40,800	13 - 160°	CM_1882597042_1 - CM_1882646878_5	240	23

[a]Range defines the distance between Enceladus and Cassini.

[b]Sub-spacecraft longitude on Enceladus

[c]The orbital phase refers to the position of Enceladus in its orbit around Saturn, also known as mean anomaly

[d]The phase angle is the angle formed between the Sun, the target being imaged (Enceladus and its plume), and the spacecraft (Cassini). Note that this number does not increase continuously over the course of the observation, but stays in the given range.

TABLE 3.2: Typical launch velocity for the three orbits being studied in this paper across orbital phase and wavelength.

Wavelength (μm)	Orbital Phase (°)	Typical launch Velocity (ms^{-1}) 279 June 18th	286 Aug 2nd	290 Aug 28th
0.95 - 1.37	174.6	141.3 ± 0.7	141.7 ± 0.5	142.9 ± 0.6
	196.0	142.4 ± 0.7	142.6 ± 0.5	143.5 ± 0.6
	217.4	143.7 ± 0.5	143.9 ± 0.3	145.1 ± 0.5
	238.4	144.5 ± 0.4	146.2 ± 0.4	147.5 ± 1.0
	260.2	144.8 ± 0.2	146.9 ± 0.5	146.8 ± 1.1
1.50 - 1.89	174.6	141.1 ± 0.8	141.4 ± 0.5	142.6 ± 0.8
	196.0	142.2 ± 0.7	142.7 ± 0.4	142.8 ± 0.6
	217.4	143.1 ± 0.7	144.2 ± 0.4	145.6 ± 0.5
	238.4	144.1 ± 0.3	146.5 ± 0.2	145.9 ± 1.3
	260.2	143.4 ± 0.6	148.1 ± 0.4	147.7 ± 1.5
2.01 - 2.41	174.6	140.7 ± 1.1	141.8 ± 0.6	141.9 ± 0.9
	196.0	141.7 ± 0.7	141.6 ± 0.5	140.8 ± 0.8
	217.4	142.3 ± 0.8	143.2 ± 0.3	145.0 ± 0.5
	238.4	142.2 ± 0.9	145.8 ± 0.4	142.7 ± 1.2
	260.2	142.6 ± 0.6	148.3 ± 0.5	145.5 ± 1.1
3.49 - 3.90	174.6	139.7 ± 0.9	140.7 ± 0.5	142.5 ± 0.7
	196.0	140.3 ± 1.0	140.8 ± 0.4	142.2 ± 0.9
	217.4	141.7 ± 0.6	141.9 ± 0.5	142.2 ± 0.7
	238.4	145.0 ± 0.5	142.0 ± 0.8	144.5 ± 0.8
	260.2	146.1 ± 0.3	148.2 ± 0.3	143.1 ± 1.4

CHAPTER 4

Noisy spectra to Particle properties: A machine learning analysis of Enceladus plume spectral data using VIMS observations

---

H. Sharma, M. M. Hedman, and S. Vahidinia

This paper is a continuation on the exploration of Enceladus plume particle population. Here in we use the same data from the second paper to study the size distribution of plume particles. I used python code to pre-process the data and apply a machine learning algorithm to derive the results discussed in the paper. I plan to submit this paper for publication by the end of 2023.

4.1 ABSTRACT

The physical properties of Enceladus plume particles can shed light on the processes responsible for driving the plume. Cassini's Visual and Infrared Mapping Spectrometer (VIMS) recorded near-infrared spectra of the plume for three Enceladus orbits around Saturn in 2017 that shows variations that may reflect changes in vent parameters over various timescales. We use a machine learning model trained on theoretical spectra generated using Mie scattering theory to deduce the plume particles' size distribution. By adding artificial noise to the data this new model is able to provide helpful constraints on the size distribution parameters. These size distribution parameters are used to calculate the average size of plume particles. The observations suggest stratification in the plume where the typical particle size decreases with increasing altitude. This stratification is stronger at higher orbital phase and is weaker when Enceladus is closer to its orbital apocenter. The average particle size appears to increase as the orbital phase increases after Enceladus passed through its the apocenter during the orbits on Jun 18th and on Aug 2nd but not

during the orbit on Aug 28th. Secondly, the overall particle size is higher on Aug 2nd, which may be due to a highly collimated jet that was active only on Aug 2nd.

4.2 INTRODUCTION

Enceladus emits a plume of water vapor and icy particles from a series of fissures located near its south pole (Spencer *et al.*, 2006; Dougherty *et al.*, 2006; Porco *et al.*, 2006). The properties of the plume particles reflect various phenomena occurring beneath the moon's surface, and so studying the properties of these particles can shed light on the processes operating inside Enceladus and the driving forces behind this geological activity. Measurements from multiple flybys of the Cassini spacecraft have been utilized to examine the plume's characteristics (Hansen *et al.*, 2006; Waite Jr *et al.*, 2006; Spahn *et al.*, 2006; Waite Jr *et al.*, 2009; Hedman *et al.*, 2009; Postberg *et al.*, 2009; Schenk *et al.*, 2018). At the same time, several different theoretical models have been developed to understand the plume and its driving mechanism (Kieffer *et al.*, 2006; Hurford *et al.*, 2007; Schmidt *et al.*, 2008; Brilliantov *et al.*, 2008; Ingersoll and Pankine, 2010; Goldstein *et al.*, 2018; Kite and Rubin, 2016).

It is important to understand the physical properties of plume particles and how they vary on different scales in order to propose more data-informed models that explain the processes involved in driving the plume. There is evidence to suggest that Enceladus' plume supplies water molecules and ice grains to the E-ring of Saturn, so studying the E-ring could also provide information on plume particles. (Spahn *et al.*, 2006; Horányi *et al.*, 2009; Kempf *et al.*, 2010). Some of the material from the plume falls back on Enceladus's surface to form deposits (Kempf *et al.*, 2010; Southworth *et al.*, 2019). Most of the current plume particle size distributions are calculated as an extrapolation of the particles in the E-ring and deductions from Enceladus' surface deposition. Kempf *et al*. (2010) concluded using simulations that the size distribution of the jet particles varies from jet to jet. Southworth *et al*. (2019) used surface deposition data from Encealdus plume emissions proposed in Spitale and Porco (2007), Porco *et al*. (2014) and Spitale *et al*. (2015) to characterize the deposition of particles in the size range, 0.6 - 15 μm. The distribution of particles

on Enceladus' surface (derived from Cassini-VIMS surface spectra) is dominated by particles ranging in size between 15 $\pm$ 5 and 60 $\pm$ 20 μm with a peak at about 20 μm (Jaumann *et al.*, 2008). In-situ measurements of the dust particles described by Postberg *et al.* (2011b) indicate that the plume is compositionally stratified with a mean particle radius in the range of 0.4 - 1.0 μm.

In this study, we use VIMS spectral data to constrain the particle size distribution of the plume using a new methodology that involves machine learning. For this analysis, we focus on the VIMS data for 3 different orbits of Enceladus around Saturn dated June 18th, Aug 2nd and Aug 28th, 2017 (Sharma *et al.*, 2023). Cassini's VIMS instrument recorded the spectra of Enceladus' plume at a wide range of wavelength from 0.3 μm to 5.2 μm at high phase angles. The variations in the shape of the spectra from one orbital position to the next, across altitude, and from one orbit to the next can be translated into shifts in particle size distribution across the same scales. In order to accomplish this task, the observed spectra need to be compared to theoretically generated spectra to find the best fit for the size distribution parameters. Theoretical spectra are generated using Mie scattering theory for a power law size distribution defined by a minimum size, maximum size, and power law index. A machine learning model is then trained on these theoretical spectra and the trained model is then used to estimate the size distribution parameters for the observed spectra of the plume particles. In order to design a more robust machine learning model, artificial noise is added to the theoretical spectra so simulate the noise in the observed spectra. This step makes the machine learning model more robust at predicting values on noisy data. Similarly, by applying the same algorithm to multiple realizations of the observed plume spectra, we obtain robust error bars on the relevant parameters. The results of these calculations are discussed in Section 4.4.

4.3 METHODS

This section describes the three steps involved in estimating the size distribution of Enceladus plume particles across orbital positions and distance from the south pole.

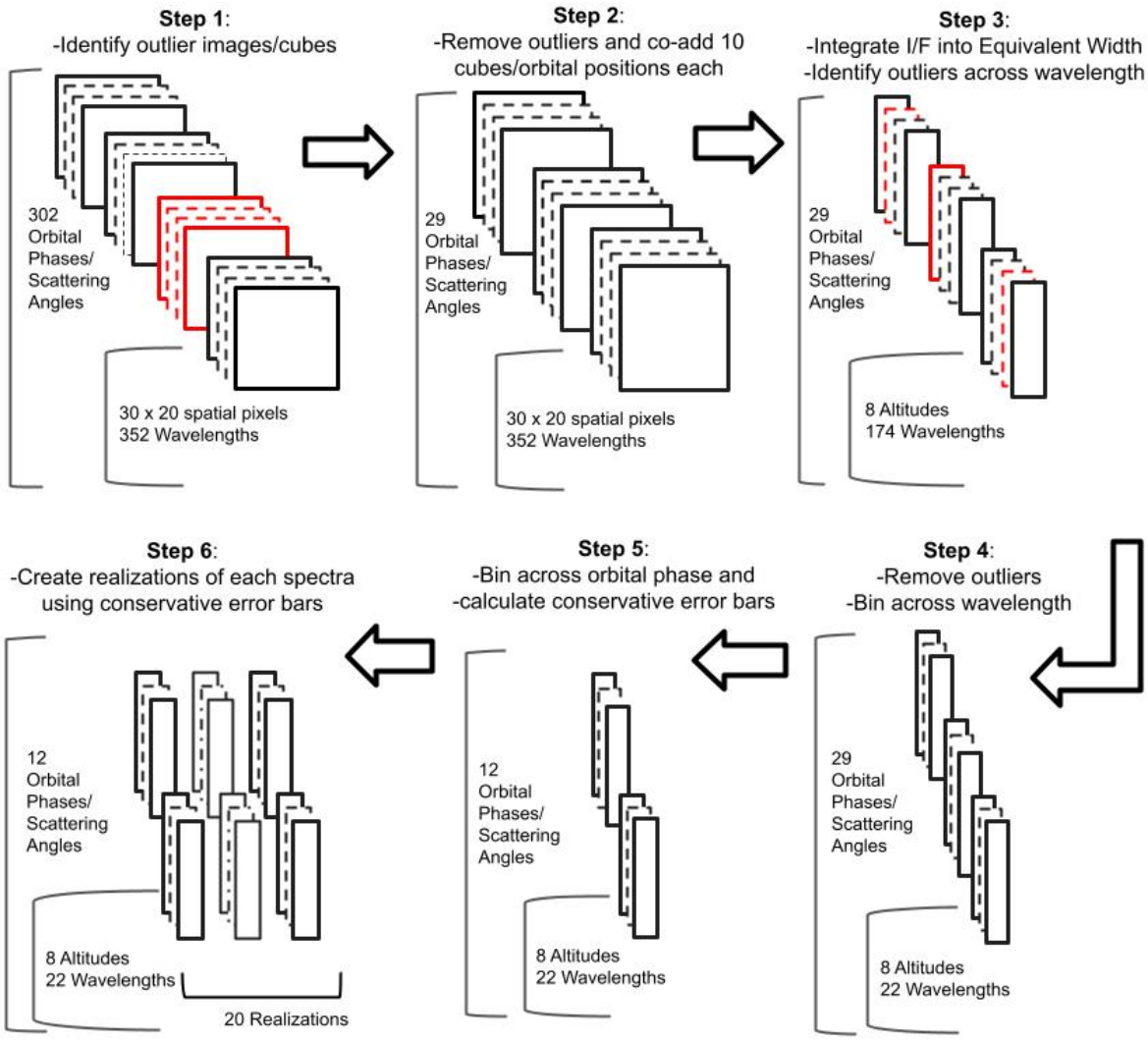

FIGURE 4.1: This figure shows the pre-processing applied to the Enceladus plume spectra. This process is applied to three different orbits - 279, 286 and 290, and the numbers shown here correspond to Orbit 279. In the first step outliers images/cubes are identified (an example is shown in red). After removing the outliers these cubes are binned into groups of 10. The cubes are then integrated into Equivalent Width and outliers are identified across wavelength at each position. After removing outliers across wavelength, the spectra is binned across 8 wavelength channels as shown in Figure 4.2. In the next step, the spectra is further binned by calculating weighted average across orbital phases of bins shown in Figure 4.3. Using the conservative error bars from the previous step, the plume spectra are augmented by generating 20 realizations of the plume spectra at each position.

Section 4.3.1 details the pre-processing applied to the observed plume spectra derived from the VIMS observations for 3 dates in 2017. Section 4.3.2 details the parameters of the generated theoretical Mie spectra used to train the machine

learning models and the similar pre-processing applied to it. Section 4.3.3 describes the machine learning algorithms applied to derive the parameters of particle size distribution.

4.3.1 *Observed Spectra/Plume Spectra*

This paper considers the VIMS observations for three different Enceladus orbits corresponding to the following dates in 2017 - June 18th/Orbit no. 279, Aug 2nd/Orbit no. 286 and Aug 28th/Orbit no. 290. Each orbit consists of a set of orbital positions defined by the orbital phase value (the angular distance between the moon's current position and its orbital pericenter, equivalent to the moon's orbital mean anomaly) and includes the orbital apocenter at an orbital phase of 180°. At each orbital position there are several altitude positions that refer to the distance from the south pole of Enceladus. The VIMS data are available for each orbital position and the different altitudes at that position. The procedure applied to improve the signal-to-noise ratio of these observations is explained in greater detail in Sharma *et al*. (2023). These steps yielded the spectra of Enceladus plume at wavelength range between 1 μm and 4 μm for the three different orbits each with its own set of orbital positions (> 10 positions for each orbit) ranging from 130° to 300° and at four altitudes from the south pole ranging from 50 km to 350 km. The raw data in each VIMS cube are converted to I/F values and re-projected onto a set of (X by Y) common spatial coordinates in a reference frame that contained the moon's spin axis. In these coordinates the center of Enceladus is located at [0, 0] and the negative y-axis is aligned with Enceladus's spin axis (Hedman *et al*., 2013), which results in a cube for each orbital position and wavelength. Table 4.1 shows the exact details for each orbit. For the sake of reference, we summarize the processing steps for these spectra in Figure 4.1. The processing of these re-projected cubes begins by identifying anomalous cubes that contain instrumental artifacts are identified as outliers and are removed from all spectral channels, (see Step 1 in Figure 4.1). Then, sets of 10 cubes are averaged to improve the signal-to-noise ratio (Step 2 in Figure 4.1) Next, in Step 3 of Figure 4.1, we convert the brightness data in the images into estimates of the plume's equivalent width at 8 different altitudes. This step involved removing

background across the cube and calculating equivalent width as the total integrated brightness in a horizontal slice through the plume (see Sharma *et al*. (2023) for more details).

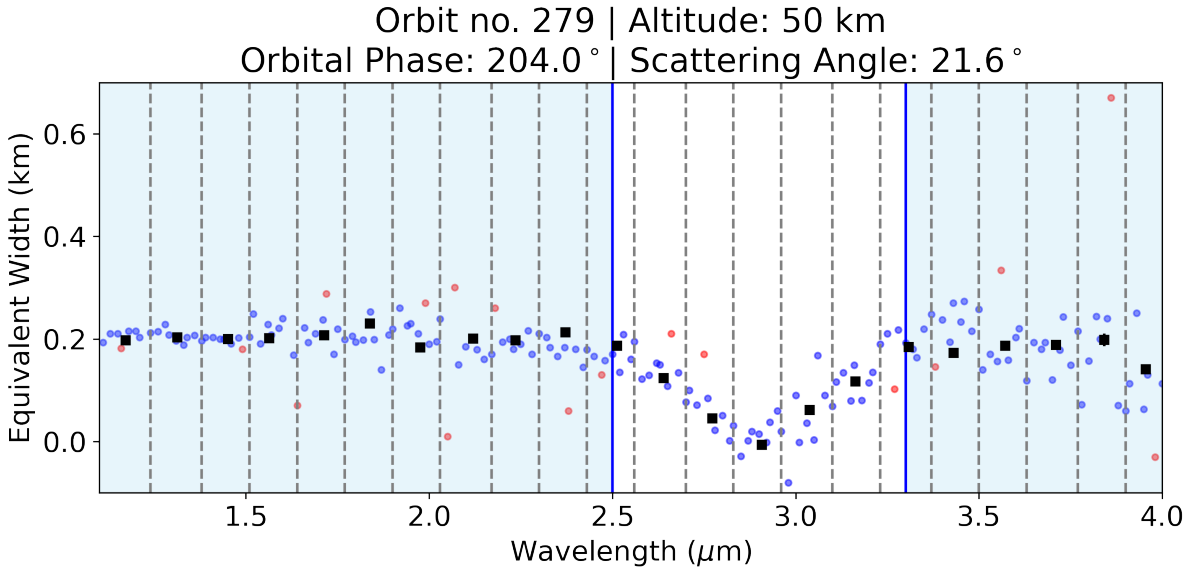

FIGURE 4.2: Example Enceladus plume spectrum showing the plume's Equivalent Width (km) across wavelength ranging from 1.1 μm to 4.0 μm. The spectrum has a clear dip around 3.0 μm corresponding to the water-ice absorption band. The blue vertical lines at 2.5 μm and 3.3 μm define two different regions outside the absorption band that are used to identify the first set of outliers using a median filter. The blue scatter points show the EW at 174 wavelengths and the red scatter points show the outliers that are removed from the spectra. This signal is then binned across 8 wavelength channels each shown using the black dashed lines. The averaged Equivalent width with respective error bars is shown as black squares.

Next, in Step 4 outliers are removed across wavelength channels and the spectra is binned across 8 wavelength channels. We exclude data beyond 4.0 μm because the signal-to-noise ratio is significantly lower at these wavelengths. Figure 4.2 shows the resulting plume spectra in terms of Equivalent width for orbit no. 279 at an altitude of 50 km and an orbital phase of 204°. There is a dip around 3 μm due to the fundamental water-ice absorption band. The blue vertical lines at 2.5 μm and 3.3 μm show the two regions outside the absorption band that are used to identify the first set of outliers across wavelength channels using a median filter in each region. The dashed black lines show the wavelength ranges that are averaged over during spectral binning and the blue scatter points show the binned values. Before averaging

the signal in each wavelength bin (defined by black dashed lines) a median filter is applied to identify a second set of outliers in each bin. After removing all outliers across wavelengths (shown in red in Figure 4.2), the Equivalent width is obtained for each wavelength bin (shown by the black squares in Figure 4.2).

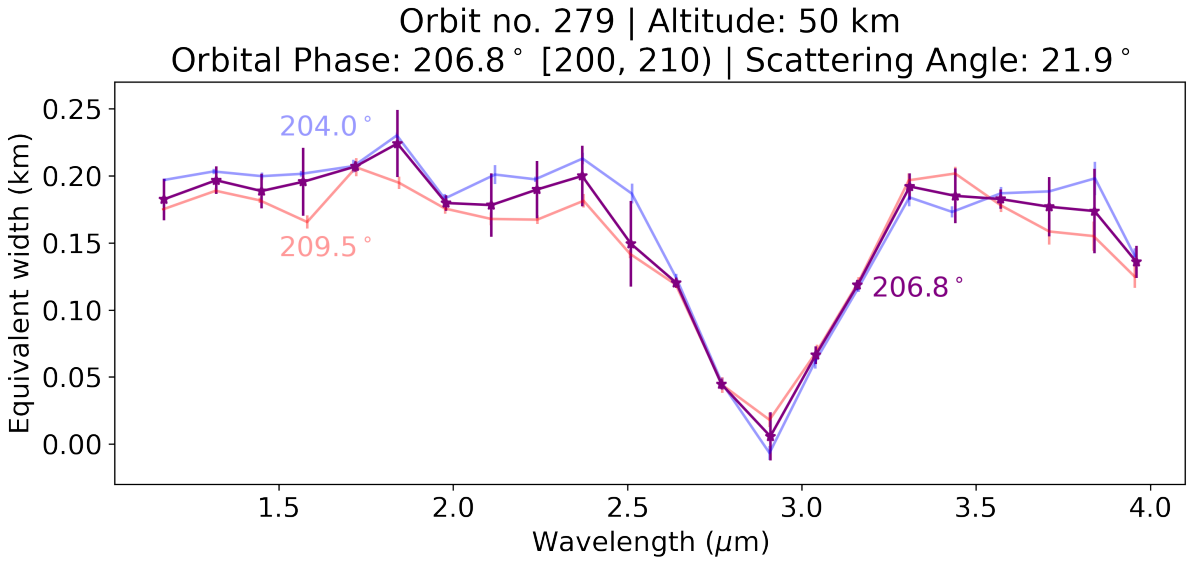

FIGURE 4.3: Example Enceladus plume spectra showing the plume's Equivalent Width (km) versus wavelength. The red and blue lines shows the EW at orbital phases in the range 200° to 210°. The dark purple line shows the weighted average of EW with conservative error bars. These error bars as calculated as the square root of the sum of squares of error on the weighted average and the standard deviation across the two orbital position shown in red ad blue.

The cubes/images are further co-added into bins of orbital phase (see step 5 of Figure 4.1). Figure 4.3 shows an example where the spectra is binned across orbital phase. To co-add the spectra across orbital phases weighted averaging is used with inverse of variance on the Equivalent width as weights. The standard deviations of this weighted average is the standard deviations of the co-added spectra. To account for any underestimation of the error bars, a conservative error is calculated for the plume spectra. A conservative error bar is the square root of the sum of squares of the error obtained from the weighted average and the standard deviation of the Equivalent width across the orbital phase bin.

The dark purple line in Figure 4.3 shows the processed plume spectra after binning across wavelength and orbital phase at an altitude of 50 km and a binned

orbital phase of 207°. The shape of the spectra around the absorption band varies from one position to another. This change in the spectral shape can help us derive information about the size distribution of the particles in the plume.

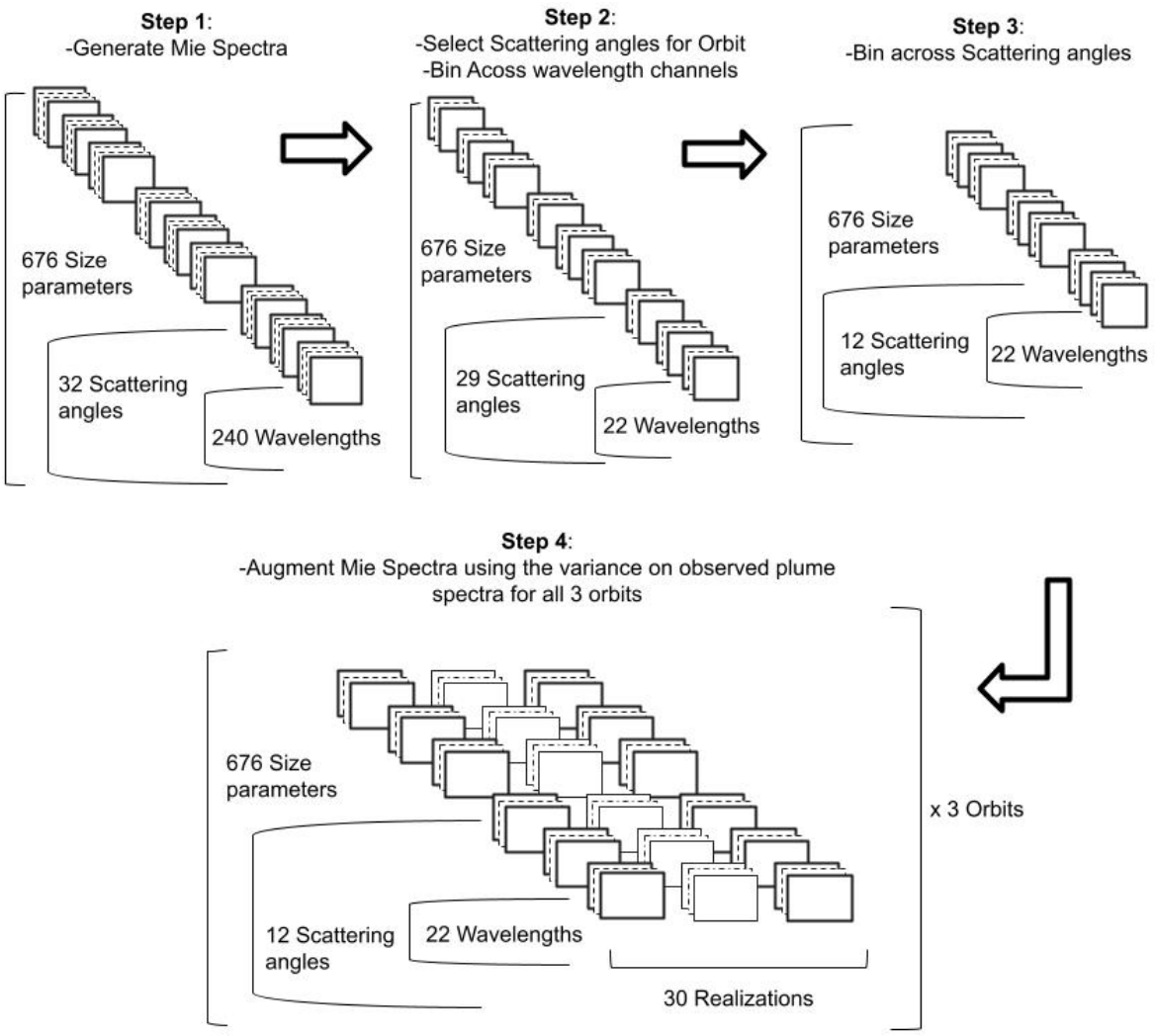

FIGURE 4.4: An outline of the processing steps applied to the Mie spectra/theoretical spectra. Theoretical spectra is generated for a power law size distribution defined by a minimum radius, maximum radius and power law index. 676 combinations of the maximum radius and power law index are used for each of 32 phase angles to generate the theoretical spectra. The relevant Mie spectra corresponding to the scattering angles of each orbit is selected and averaged over bins of scattering angles. In the final step, 30 realizations are created for each variation of Mie spectra, which will be used to train a robust machine learning model that results in best fit for observed spectra.

4.3.2 *Theoretical/Mie Spectra*

In order to translate the observed spectra into information about the size distribution parameters of particles in Enceladus' plume, we need to compare the observed data to predictions from Mie theory. Mie theory is based on Maxwell's electromagnetic field equations and predicts the scattering intensity as a function of particle size, angle of observation, and wavelength and polarization of the incident beam provided that the particle being measured is spherical, internally (optically) homogeneous, and of known refractive index. From this Mie scattering pattern, information related to the size distribution of the particles (where the size of the scattering particles is comparable to the wavelength of the light) can be obtained.

Figure 4.4 shows the pre-processing steps applied to Mie spectra, which is similar to the processing for the spectra of plume particles as shown in Figure 4.1. In step 1, we generate theoretical spectra based on Mie scattering theory for a large parameter space using the SF_SD function from the python library PyMieScatt created by Sumlin *et al*. (2018). The parameters required to generate scattering intensity pattern are the wavelength of the incident light, the wavelength-dependent refractive index of material, the observed scattering angle, and the particle size distribution. The wavelength of the incident light and the range of scattering angles are the same as the VIMS observations i.e. 0.9 to 5.0 μm and 18° to 24.4°. The wavelength-dependent refractive index of crystalline water-ice is defined using Mastrapa *et al*. (2009) at 20 K. The size distribution of particles is assumed to follow a truncated power-law defined by a power index, minimum radius, and maximum radius. The minimum radius is assumed to be 0.1 μm since the near-infrared spectra are not sensitive to this parameter. The maximum radius and power law index vary from 2.0 μm to 4.5 μm and -3.5 to -1.0 with a resolution of 0.1 μm and 0.1 respectively. This yields 676 combinations of size parameters and for each of these combinations the theoretical spectra is generated for 32 scattering angles ranging from 18° to 24.4°. Figure 4.5 shows examples of Mie spectra for a fixed scattering angle of 21.9° and for different combinations of size distribution parameters (maximum radius and power index). The shapes of this theoretical spectra capture the water-ice absorption band that we

observed in the plume's observed spectra. The other combinations of these size distribution parameters provide a large parameter space to fit the observed spectra.

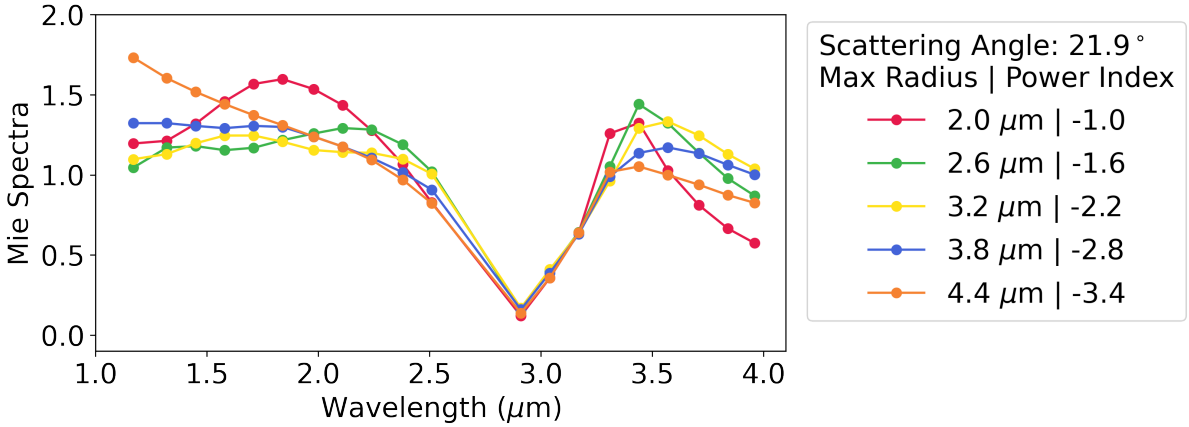

FIGURE 4.5: A selection of the Mie spectra generated for different size distribution parameters at a scattering angle of 21.9°. These theoretical Mie spectra is generated using a Python package called PyMieScatt for a range of size distribution parameters that follow a truncated power law. The minimum radius is assumed to be constant at 0.1 μm and the maximum radius is varied from 2.0 μm to 4.5 μm and the power law index ranges from -3.5 to -1.0.

Each orbit has its own range of scattering angles and in step 2 of the pre-processing, the Mie spectra are chosen for a subset of the scattering angles corresponding to the appropriate orbit. The wavelength range of the spectra is then reduced to 4.0 μm as is the range selected for the observed plume spectra. The theoretical Mie spectra are then binned in the similar way as the observed plume spectra to yield brightness values at 22 wavelengths. In step 3 of Figure 4.4 the theoretical spectra are further binned across scattering angles using the same bins used in step 5 of the pre-processing of observed plume spectra. This step generates the spectra for the same range of scattering angles as the observed spectra during the appropriate orbit.

We next augment these theoretical spectra with realizations of noise based on the errors from the observed spectra. Since the plume spectra are defined for several different altitudes, the error bars on the spectra are averaged across all 8 altitudes. These averaged error bars are then multiplied by a randomly generated standard normal distribution and added to the Mie spectra. This process is used to create 30

realizations of each Mie spectra as shown in step 4 of Figure 4.4. Figure 4.6 shows an example Mie spectra in black and its 30 realizations in color. Since the plume spectra is defined for several different altitudes, the error bars on the spectra are averaged across all 8 altitudes. These averaged error bars are then multiplied by a randomly generated standard normal distribution and added to the Mie spectra. This process is used to create 30 realizations of each Mie spectra as shown in Step 4 of Figure 4.4. Figure 4.6 shows an example Mie spectra in black and its 30 realizations in color. A similar process is also applied to each plume spectra to obtain error bars on the predicted target variables shown in Step 6 of Figure 4.1. Figure 4.7 shows an example plume spectra in black and its 20 realizations in color. These realization were obtained by adding the spectra and the product of random standard distribution and error on the observed plume spectra. The motivation behind calculating these realizations is used to obtain error bars on the maximum radius and power law values estimated using machine learning model as discussed in the next Section 4.3.3.

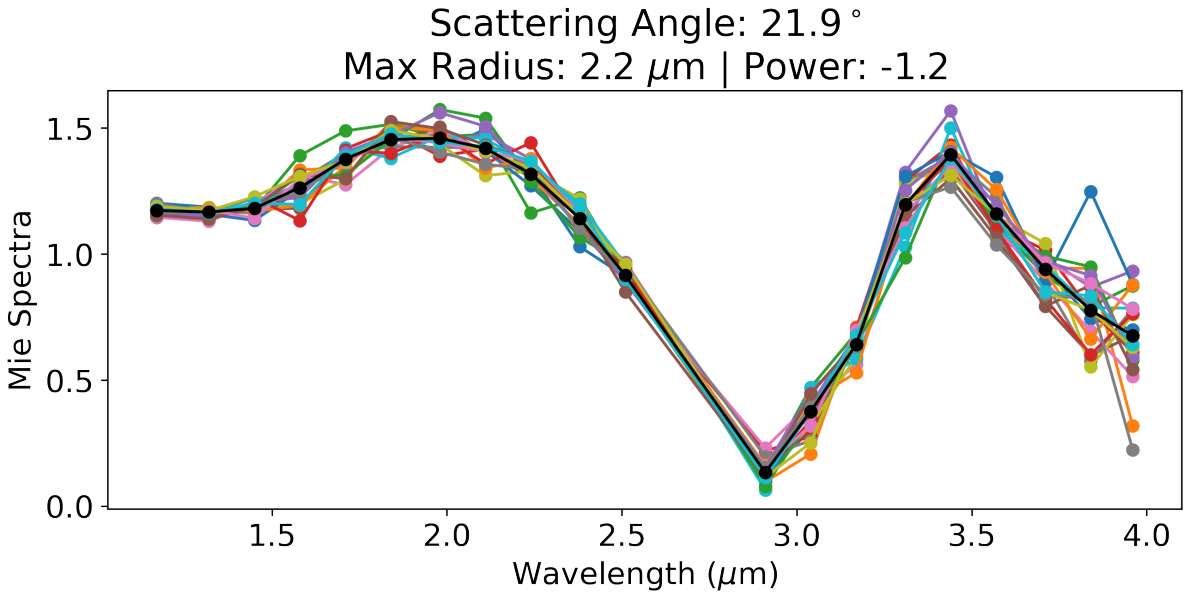

FIGURE 4.6: Example augmented Mie spectra for a scattering angle 21.9° and a maximum radius of 2.2μm and a power law index of -1.2. in black and 30 realization of the spectra in color. The various realizations are calculated by adding the product of a random standard distribution and the error bars on the observed plume spectra to the generated Mie spectra.

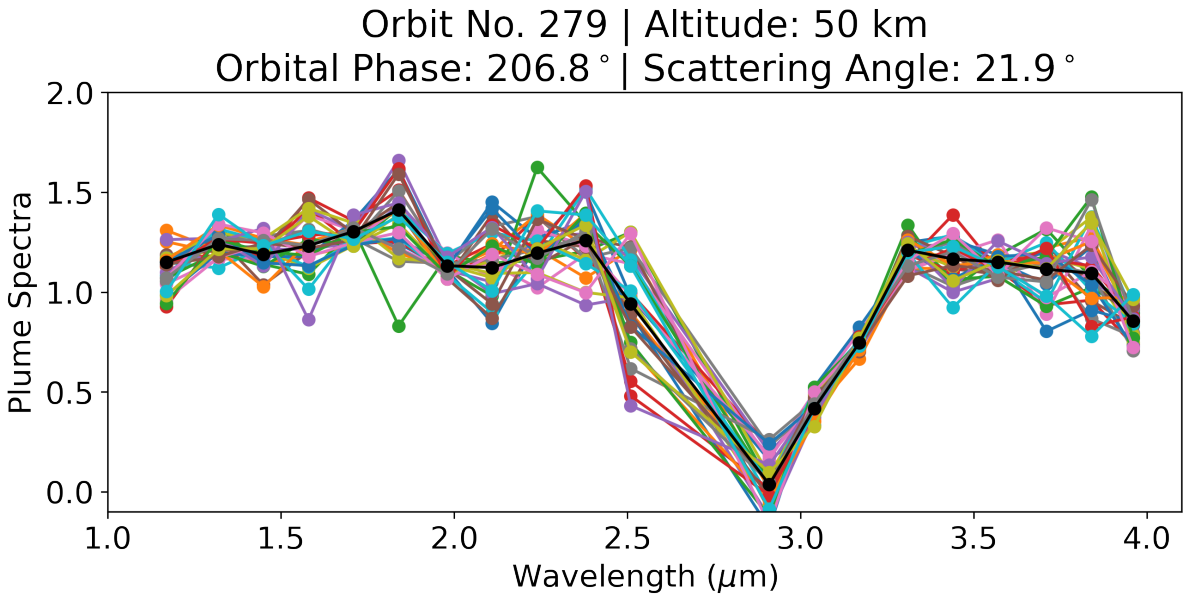

FIGURE 4.7: Example augmentations of an observed Enceladus plume spectra at an altitude of 50 km and an orbital phase close to 200° after pre-processing. The black line shows the binned spectra obtained after weighted average across orbital phase and the colored lines show the 20 realizations created using the conservative error bars. The realizations are calculated as the sum of the plume spectra and the product of the error bars and random standard normal distribution.

4.3.3 *Machine Learning*

In principle, we can identify the theoretical spectrum that is closest to each observed spectrum using appropriate statistics like chi-square goodness of fit method, and thereby determine the most likely values of the size distribution parameters. However, in practice the observed spectra are a nonlinear function of the particle size distribution parameters, and the data are sufficiently noisy that multiple theoretical spectra provide comparably good matches to each observation. These issues complicate any effort to reliably estimate the error bars on the size distribution parameters. Fortunately, we have developed a machine-learning algorithm that can handle these complications in an relatively automatic manner.

The specific machine learning algorithm we use is a supervised learning algorithm. A supervised learning algorithm is where you have input variables (X) and an output variable (y) and you use an algorithm to learn the mapping function f(X) from the input to the output such that, y = f(X). The goal is to approximate

the mapping function so accurately that the model can predict the output variables y for new input data X. Regression is a sub-type of supervised machine learning where in the target variable is continuous. In this case, the theoretical spectra generated using Mie scattering theory can be used as input X with two continuous target variables (y): maximum radius and power index (the minimum radius is assumed to be constant at 0.1 μm). A supervised regression machine learning model can approximate a mapping function between the input spectra and the target size distribution parameters and then be applied to the observed spectra.

A machine learning model is termed robust when it performs consistently in real-world scenarios where data may be noisy, unexpected, or contain variations. The theoretical spectra being used as input for the supervised regression model is generated using the Mie scattering theory and contains no errors or noise while the observed plume spectra contains noise or variations. A machine learning model that is trained on perfect, noiseless data, such a model does not generalize well to new data that may contain noise. To make the model robust to noise, we create realizations of Mie spectra using the variance on observed plume spectra (discussed in Section 4.3.2). This process helps us to train a more reliable machine learning model that can detect the relationship between the shape of the spectra and the size distribution parameters irrespective of noise in the data.

A machine learning model trained on the realizations of the noisy theoretical spectra can estimate the maximum radius and power index for each observed plume spectra. These results are devoid of error bars. Realizations are also calculated for the observed spectrum as discussed in Section 4.3.2. With 20 realizations for each observed spectra, 20 target variables can be predicted and averaged to obtain the standard deviation on the result. The machine learning model trained on robust data can now be used to estimate the size distribution parameter for each realization enabling us to average these results in order to obtain more reliable estimate with error bars on them.

There are several machine learning models available that have a range of properties, and we are trying to evaluate, which algorithm to use for the current problem. The accuracy of the ML model can be judged by testing the model's

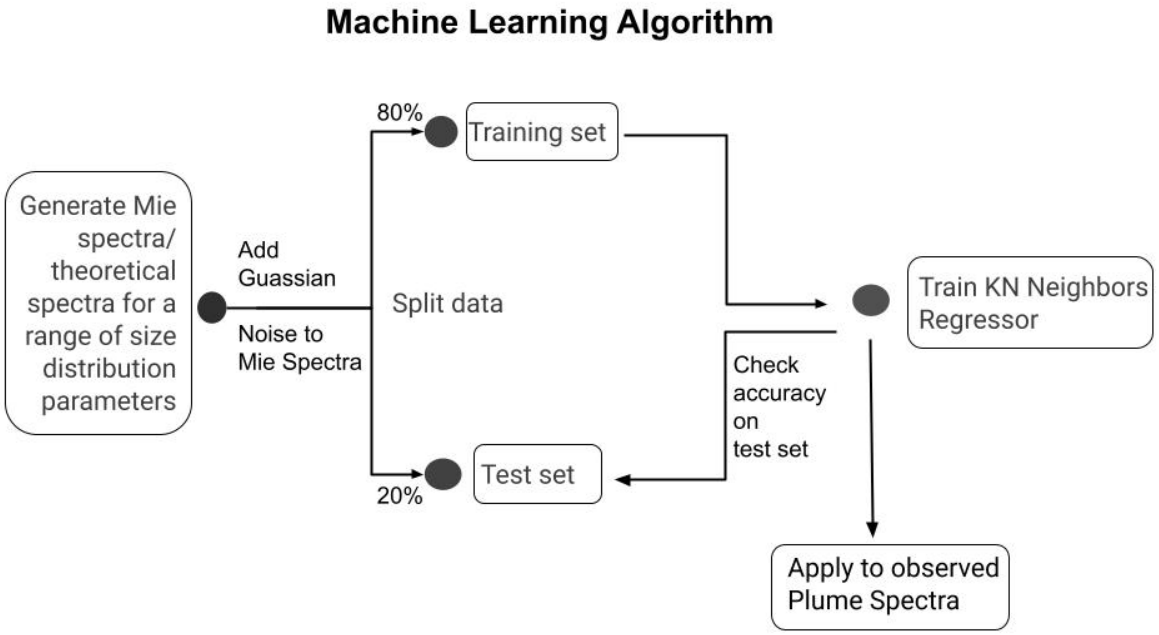

FIGURE 4.8: Flow chart for the machine learning approach used in this project. This begins with the Mie spectra derived in Figure 4.4. The Mie spectra are then split into 80:20 ratio as training and testing data. The machine learning model is trained on the training data and an error is calculated on the test data. The trained model is then used to estimate the size distribution of plume particles.

performance on the theoretical data. The theoretical spectra dataset can be divided into two parts: training and testing as shown in Figure 4.8. The mapping function is modeled on the training data and its accuracy is calculated on the test set to determine how well the model fits the data. In the case of a regression problem, we use root mean squared error on the predicted target labels and the original target labels to find the error on test set of the data. In order to compare the root-mean-squared error computed by each model we use the K-fold cross validation. K-fold cross validation divides the data into k-subsets. This method is repeated k times where in each step the model is trained on the k-1 number of folds and the model is tested on the kth set. The four different models compared are: Linear regressor, K-nearest neighbors regressor, Decision tree regressor and Random forest regressor as shown in Figure 4.9. Figure 4.9 shows the root mean squared error on the k folds in the form of a box plot. The random forest does better than the other models but takes much longer. We chose to use K-nearest neighbors regressor because it is less

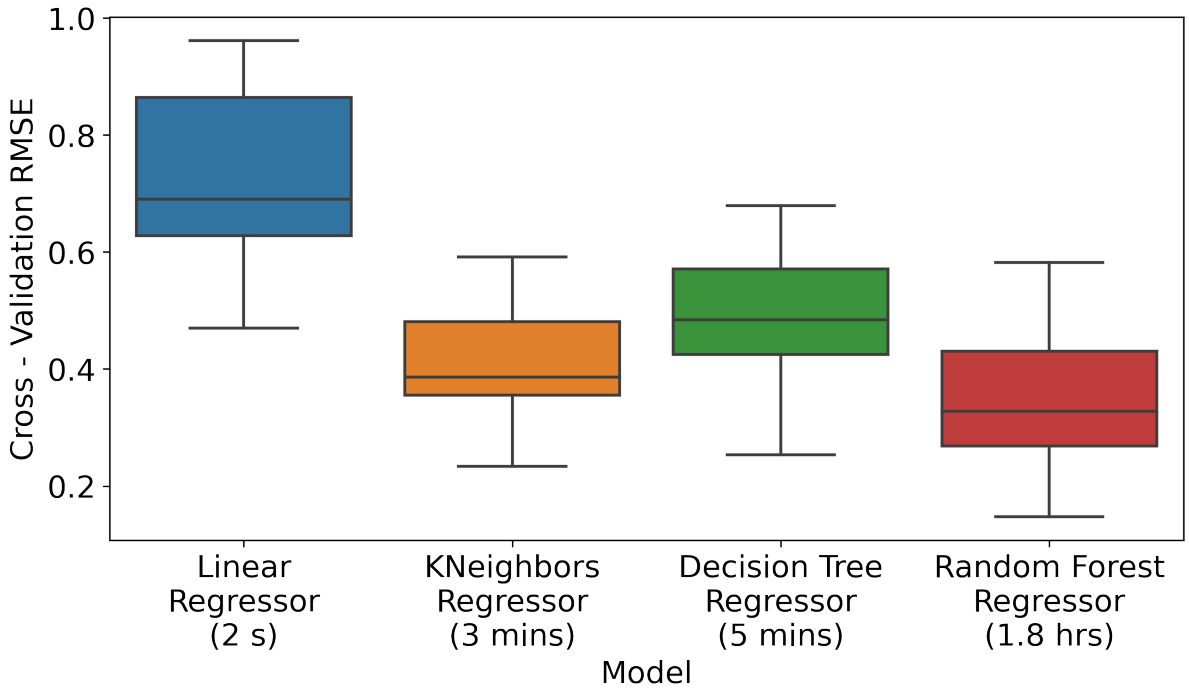

FIGURE 4.9: The x-axis shows the 4 machine learning models being compared and the y-axis shows the root-mean-squared-error on the predicted values. This plot shows a relative metric of different algorithms rather than an overall assessment of the quality of the fit. A machine learning algorithm provides a framework that can handle the non-linear relationship between the plume brightness at different wavelengths and particle size distribution parameters. These models are trained on k-1 folds of data and used to make predictions on the kth fold to obtain these cross validation scores. Finally, K-nearest neighbors is used to calculate the plume's particle size distribution as it is less computationally expensive and has a low error rate.

computationally expensive as it only takes 3 minutes to run the model and the root mean squared error has a median value of 0.3. This accuracy and efficient of the model affirms that the model performs well on theoretical spectra with added noise in it and can be used on observed spectra.

The chosen machine learning model is called K-nearest neighbors and uses the input data features to calculate the best fit. The input data also need to be transformed for the model to work accurately. The features of the dataset consists of the Equivalent Width at different wavelength channels and the scattering angle as the input and the maximum radius and power index as the output variables. K-nearest neighbors uses an inverse distance weighted average of the K-nearest neighbors of

the sample data. In order to calculate the euclidean distance between data points we need a normalized range for the data. The range of features is different and since K-nearest neighbors uses a distance metric the features need to be scaled. Feature scaling is applied to the features such as the mean is 0 and the standard deviation is 1. The K-nearest neighbors regressor is trained on the theoretical Mie spectra and is tested on the test set. The trained model is then used to make predictions on the observed plume spectra.

The target variables give us the best fit Mie spectra for each observed plume spectra. We can also verify that this process yields sensible results by comparing the observed spectra to the predicted spectra for the particle size distribution parameters provided by the algorithm. Figure 4.10 shows the plume spectra with the predicted Mie spectra for a few example observations. These plots show that the machine learning model provides a reasonably good fit for the observed spectra of plume particles.

4.4 RESULTS AND DISCUSSION

We can now use the machine learning model to compare particle size over the different scales such as across orbital phase, altitude, and from one orbit to another. The machine learning model gives a reasonable estimate of the parameters of the size distribution of particles in the plume. The variations in these parameters across all scales are shown in the Figure C.1 and Figure C.2 available in the Appendix C.1. While the fits yield estimates and errors for the index and cut off, it is also useful to consider the average particle size. Since the size distribution is assumed to follow a power law, an average particle size can be calculated for a specific set of parameters. The maximum particle size and power index are used to calculate the average particle size as follows:

$$s_{avg} = \frac{\int_{s_{min}}^{s_{max}} s^{p+1}\, ds}{\int_{s_{min}}^{s_{max}} s^{p}\, ds} \tag{4.1}$$

where s_{min} is the minimum particle size assumed to be 0.1 μm, s_{max} and p are the maximum particle size and the power index for the spectra being studied.

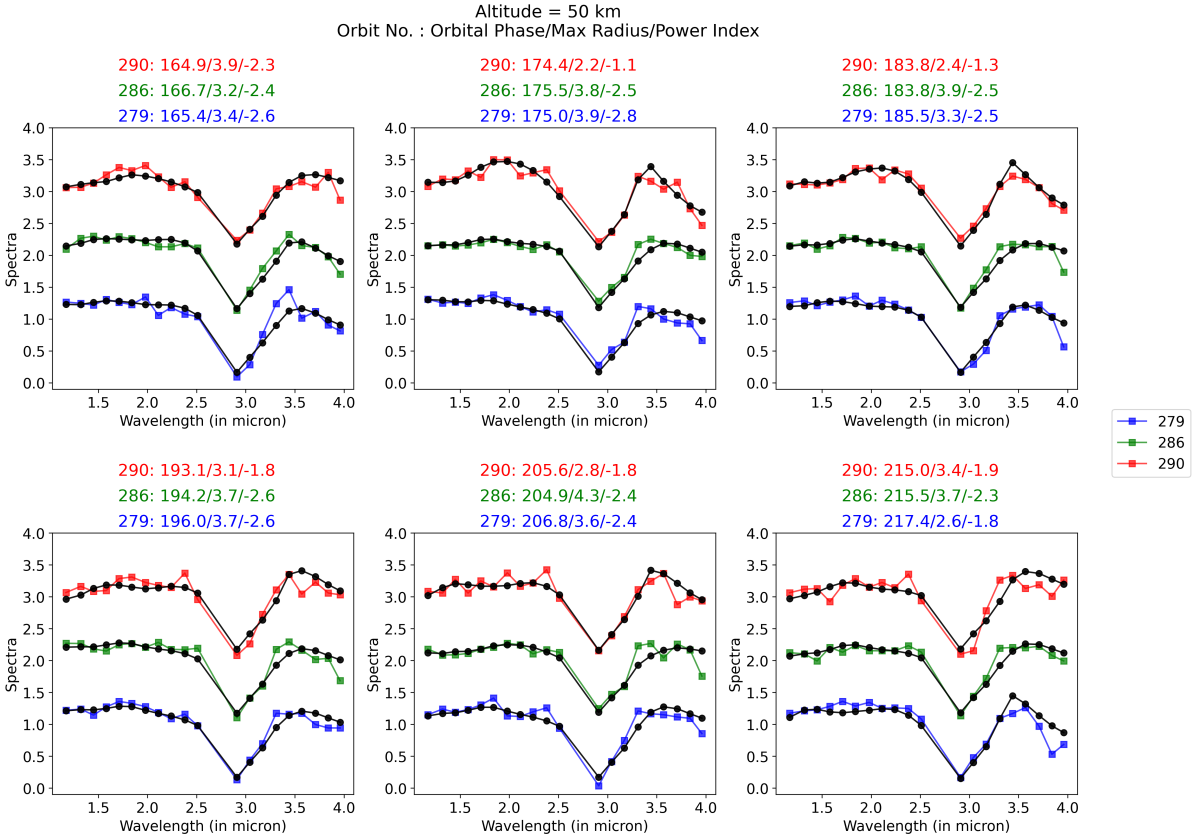

FIGURE 4.10: Example plume spectra (in color) over plotted with Mie spectra (in black) using the best-fit size distribution predicted using the machine learning model. The theoretical Mie spectra are a reasonably good fit on the plume spectra. This reaffirms that the machine learning model is indeed working and gives good results.

Ingersoll and Ewald (2011) used ISS images at distinct wavelength filters to fit a grain size distribution model that results in a median-grain radius of 3.1 μm, which is higher than the average particle sizes obtained in the current analysis. This discrepancy could be due to the different wavelength ranges being explored by the two instruments and the fact that the Ingersoll and Ewald (2011) model assumes that the particle size distribution to be independent of altitude/distance from the south pole.

Figure 4.11 shows the average particle size for all three orbits at different altitudes. On of the common variations among all orbits/dates is the slight reduction in the average size of plume particles as altitude increases. This general trend is consistent with the conclusions made in Hedman *et al.* (2009) and is generally expected. There

are variations in this decrement that are interesting. The degree of this decrement is different on different dates/orbits. Another important observation is the change is average particle size as the orbital phase increases. For these observations, we are able to observe Enceladus crossing its apocenter around 180° to getting closer to its orbital pericenter at 360°/0°. The average particle size appears to decrease as the orbital phase gets closer to 300°. These variations are discussed in more detail below.

In Figure 4.11 on June 18th/Orbit no. 279 at a distance of 50 km from the south pole of Enceladus, the average size of particles in the plume increases as the orbital phase increases i.e. as the moon moves beyond its orbital apocenter (180°). This increase in average particle size appears to be phase shifted with respect to the plume's brightness maxima. At the apocenter, Enceladus is farthest from Saturn and the cracks at the south pole are being pulled apart due to tidal stresses (Hedman *et al*., 2013). The wider cracks around the apocenter could be contributing to the rise in average size of plume particles.

The June 18th/Orbit no. 279 observation covers a larger range of orbital position as compared to Aug 2nd/Orbit no. 286 and Aug 28th/Orbit no. 290. There is some evidence to suggest a subtle drop in the average size of plume particles as the orbital phase increases beyond 280° at altitudes of 150 km and 250 km, as the moon progresses towards its orbital pericenter (360° or 0°). This hints at a weak direct relationship between the crack width and plume particle size, which appears to be phase shifted.

There is a slight drop in the overall particle size as the altitude increases from 50 km to 350 km. One possible explanation is that the larger particles are launched at a slightly lower velocity than smaller particles and thus are unable to reach higher altitude from the south pole. This drop is larger at higher orbital phase for orbit 279 on June 18th.

On Aug 2nd/ Orbit no. 286 at a distance of 50 km from the south pole, we see an increase in the average particle size as the orbital phase increases beyond 200°. This trend is present at all altitudes in this particular observation. Ingersoll *et al*. (2020) reported that the brightness of the plume is higher on Aug 2nd than on June 18th and Aug 28th at short wavelengths due to a highly collimated jet seen only on Aug 2nd

(Ingersoll *et al.*, 2020). The lack of a trend in the average particle size with altitude for orbit 286 on Aug 2nd implies larger particles are no longer being launched at lower speeds, which might be consistent with more intense jets.

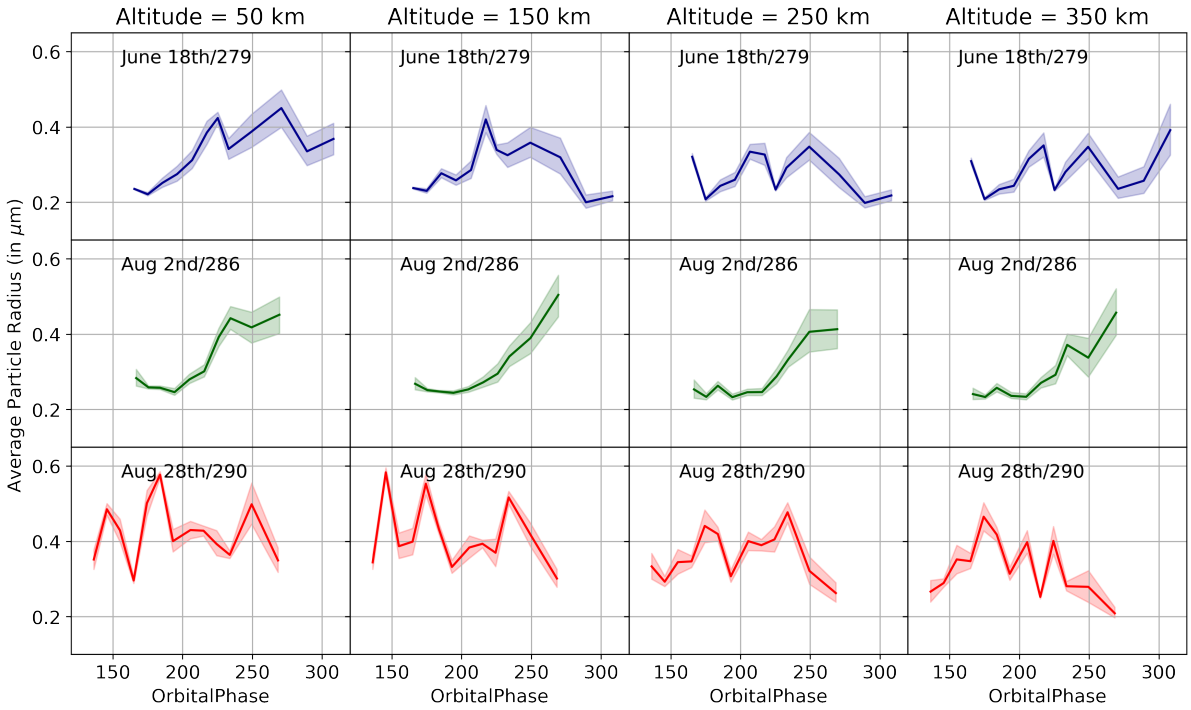

FIGURE 4.11: The average particle radius of the plume particles as a function of orbit phase and altitude for the three orbits. The shaded region highlights the degree of uncertainty on the estimated values. There is an overall reduction in the particle size as the altitude increase from 50 km to 350 km. This over fit suggests a degree of stratification in the plume.

On Aug 28th/Orbit no. 290 the average particle size around orbital phase of 180° is slightly higher than June 18th and Aug 28th. Sharma *et al.* (2023) noticed that the spectra from Aug 28th have a redder slope than the earlier data on June 18th and Aug 2nd and proposed that this observation indicated that the plume contained a higher fraction of larger particles on August 28. This observation is because the particle size is higher in orbit 290 than in the other 2 orbits as seen in Figure 4.11. The trends of increasing size with orbital phase is not present for orbit 290, but there is stratification in the plume at high and low orbital phase. At low orbital phase of around 150° and high orbital phase of 250° the average particle size decreases with increasing altitude.

On all three dates, June 18th, Aug 2nd and Aug 28th, there is a slight decrease in the overall average particle size as altitude increases. This decreases in size implies that the average of plume particles varies with altitude thus introducing stratification in the plume. The stratification in the plume column could indicate that the smaller particles are faster while the larger particles slow down and are unable to reach higher altitudes. We observe an increased stratification at higher orbital phase of 250° and a lower stratification at lower orbital phase of 180°.

Numerical models have been proposed to understand the physics of Enceladus south polar plume that takes into account the particle grain size and how they interact with gas (Yeoh *et al.*, 2015). Yeoh *et al.* (2015) reasoned that the distribution of grain size, speeds and temperature need to be used an an input to predict and accurate model that can simulate the subsurface flow properly. The observations studied in this paper and the results of average particle size variation could be used to design/propose more thorough models that explain the origins and the processes involved to generate Enceladus' plumes.

TABLE 4.1: The three data sets studied in this paper.

Orbit no. Date	Orbital Phase[c]	Phase angle[d]	Range[a] (km)	Longitude[b]	Cubes	No. of cubes before binning	No. of cubes after binning
279/June 18th, 2017	162 - 319°	156 - 161°	8,37,300 - 10,93,300	11 - 164°	CM_1876443559_1 - CM_1876495215_1	302	28
286/Aug 2nd, 2017	162 - 286°	159 - 161°	8,22,700 - 10,63,000	29 - 150°	CM_1880355368_1 - CM_1880396071_6	293	26
290/Aug 28th, 2017	130 - 281°	156 - 158°	8,68,600 - 11,40,800	13 - 160°	CM_1882597042_1 - CM_1882646878_5	240	23

[a]Range defines the distance between Enceladus and Cassini.

[b]Sub-spacecraft longitude on Enceladus

[c]The orbital phase refers to the position of Enceladus in its orbit around Saturn, also known as mean anomaly

[d]The phase angle is the angle formed between the Sun, the target being imaged (Enceladus and its plume), and the spacecraft (Cassini). Note that this number does not increase continuously over the course of the observation, but stays in the given range.

CHAPTER 5

Conclusion

This dissertation focused on three different papers that explored noisy spectral data of dust particles on our own Moon and Saturn's moon Enceladus. The first paper on Lunar dust used the data collected by Lunar Atmosphere and Dust Environment Explorer (LADEE) spacecraft's Ultraviolet and Visible Spectrometer (UVS). The UVS conducted a series of Almost Limb Observations near the dawn-terminator region of the Moon. The paper discussed in details the methods used to reduce the noise in this spectral data such as averaging and background subtraction. The filtered data were then compared to the predicted spectra for dust atmospheres with various exponential scale heights and particle size distributions. Even though we do not find evidence of dust above the Moon's surface, we can use the generalized spectra of dust particles to isolate the part of the signal that can constrain dust density limits above the Moon's surface. For a mono-dispersed size distribution at a particle size of 0.1 μm and a scale height of 1 km the upper limit for dust density at the Moon's surface is 3.1 x 10^4 m^{-3}. For the dust population that follows a differential size distribution proportional to s^{-3} and s^{-4} ranging from 0.3 to 10 μm at a scale height of 1 km, the upper limit on dust density at the Moon's surface is 140 m^{-3} and 190 m^{-3} respectively. At an altitude of 10 km above the Moon's surface these values reduce to around 6 x 10^{-3} m^{-3} and 9 x 10^{-3} m^{-3} respectively.

These constraints on dust population should inform models of interactions between the lunar surface and any ambient plasma. Our limits on the dust density within 3 km of moon's surface equal to 142 m^{-3} are orders of magnitude higher than the measured densities of 0.0004 m^{-3} for particles larger than 0.3 μm obtained by Szalay and Horányi (2015) using LDEX data. LDEX could only measure dust densities down to altitudes of around 3 km while LADEE-UVS can probe lower altitudes as the line-of-sight touches the surface during the Almost Limb observations studied in this analysis. Rennilson and Criswell (1974) used Surveyor data to measure a tenuous cloud formed temporarily just above sharp sunlight/shadow

boundaries in the terminator zone and estimated column grain density of 50 grains cm^{-2} for particles of size 10 μm and converting this value into a density estimate is challenging because the column length is not well constrained. The current dust density limits in this work at most constrain the very tail end of the dust population observed by Surveyor. These higher limits mean that additional low-altitude dust populations besides the dust population measured by LDEX could potentially exist on the Moon, including electrostatically lofted dust that can only reach low altitudes. Electrostatically lofted dust could answer questions about the charged state of the regolith as dust is raised above the surface due to electric fields. Additionally, the dust density limits obtained in this study are in agreement with models that predict higher dust densities closer to the lunar surface. For example, the theoretical model by Popel *et al*. (2018) and the experimental measurements by Yeo *et al*. (2021) propose dust lofting mechanisms involving an electrostatic potential barrier in the region of the terminator and a photoelectron sheath. Using these models the lofting heights on the Moon were found to be about 30 cm for 2 - 3 μm radius dust grains and 3 km for 0.1 μm radius grains. The latter altitude is in the range of observations in the current analysis. Hence, these observations constrain the density of such small grains, which are expected to have negative charges and thus contribute to the lunar plasma environment. Future measurements like these could therefore potentially constrain the size and charge state of the lunar dust.

The amount of dust above the lunar surface could also constrain overturning rates in the top 1 mm of the lunar regolith, since the total amount of dust constrains the rate at which micrometeoroids hit the lunar surface and cause regolith overturn. For example, Pokornỳ *et al*. (2019) proposed a model with a meteoroid mass flux of approximately 1.4 tons per day impacting the lunar surface that gave an estimated gardening rate of about 30 cm per million years. However, this model also predicts the density of lunar ejecta cloud to be four orders of magnitude larger than reported values by LADEE dust detector (Pokornỳ *et al*., 2019; Szalay and Horányi, 2015). However, these limits are in agreement with the dust density limit of 142 m^{-3} for the size range of 0.3 - 10 μm obtained in this analysis. This agreement between the predictions of Pokornỳ *et al*. (2019)'s model and the current limits implies that the

conditions of the model would be a reasonable estimate of the lunar environment with an ejecta mass product rate of 3 x 10^{-12} g cm^{-2} s^{-1}. The amount of dust lofted also depends on the properties of the surface like its cohesion and composition, so tighter constraints on the dust density can help further constrain these regolith properties.

These dust density limits also have practical application for more accurate and safer future lunar exploration. For example, sub-micron dust grains could contaminate astronomical observations of infra-red, visible and UV light over the majority of the lunar surface and a thorough understanding of lunar dust behaviour is necessary in order to effectively tackle these problems in the future (Murphy and Vondrak, 1993). The dust density limits obtained here can therefore help define design specifications for remote-sensing instruments that will be stationed on the Moon.

The next part of this dissertation explored the data recorded by the Visual and Infrared Mapping Spectrometer (VIMS) onboard Cassini. VIMS observed Saturn's moon Enceladus, specifically the plumes emanating out of the cracks on its south poles. The plumes contain water vapor and icy dust particles that may originate from its subsurface ocean. The second paper studies the spectra of the plume to understand the variations in velocity of dust particles with Enceladus' orbital position and from one month to the next. The spectra recorded by the VIMS instrument also have a low signal to noise ratio and this work also details the methods used to reduce noise and improve the signal strength. The outliers are removed in two different ways at different steps of the process and the spectra is averaged across orbital phase and wavelengths. These procedures helped us obtain data that was then used to derive typical velocity of dust particles using the plume's spectral profile with altitude/distance from the south pole. We found that at wavelengths between 1.2 μm and 3.7 μm, the typical launch velocity of dust particles in the plume ranges between 140 ms^{-1} and 148 ms^{-1}.

The typical launch velocities of plume particles obtained in this analysis do not vary as expected by the current models, which implies that the dynamics of the plume at the vents are different from what had been proposed. The vent openings

at the south pole of Enceladus act a bit like a nozzle, which allows the gas to leave the vent at supersonic speeds. By contrast, the plume particles are moving slower than both the observed and the expected speed of vapor coming from liquid water exposed to vacuum ($\sim$ 450 m/s Hansen *et al.*, 2011). The most common explanation for this is that the particles are both accelerated upwards by the water vapor but are slowed on its way out of the cracks by collisions with the walls. These sorts of models naturally lead to larger particles having lower launch velocities (eg. Schmidt *et al*. (2008)). However, we observed a much smaller reduction in particle velocity than these models would predict. Schmidt *et al*. (2008) expects a large fractional reduction of 0.98 in the typical particle velocity as size increases from 1.2 µm to 3.7 μm, while only a fractional reduction of 0.01 - 0.16 is observed in the current work for the same wavelength range, which is 6 times lower than predicted. There are two possible explanations for this observation: either the vent parameters are very different from what was assumed in Schmidt *et al*. (2008) model, or particle-particle interactions at the vent are more common than previously thought. The mean free path for particle-particle collisions is 1 m and is comparable to the measured vent sizes of 2.8 m and 9 m on the south pole of Enceladus (Goguen *et al.*, 2013; Yeoh *et al.*, 2015) implying that these collisions could occur at the vents affect the launch velocity of particles in the plume.

A simplistic view of these particle-particle interactions would be that smaller particles with higher velocities could kick up the larger particles with slower velocities, accelerating them through the vent columns. These sorts of particle-particle collisions would naturally cause grains of different sizes to have similar velocity distributions. Future models of the particle and vapor dynamics near the vents will therefore likely need to consider these particle-particle interactions. The complete model that explains the complex affects of particle-particle collisions requires further work and is beyond the scope of this work.

The third paper takes the exploration of Enceladus plume particles one step further. This paper dived into how noisy spectra can be used to derive the physical properties of particles in a reliable and efficient manner. The observed plume spectra are compared to the theoretical spectra using a machine learning model to derive

size distribution parameters for particles of the plume. These parameters are then used to calculate the average size of particles in the plume and how it varies with orbital position, altitude and from one orbit of Enceladus to the next. The significance of this methodology lies in the way it handles noise in spectral data. A form of artificial noise is added to both the theoretical spectra to better train the machine learning model and to the observed spectra to obtain error bars on the parameters estimated using the trained machine learning model. This robust machine learning model enables us to predict the size distribution parameters for Enceladus' plume particles for three different dates in 2017. On all three dates, there is a slight decrease in the overall average particle size as altitude increases. This indicates a degree of stratification in the plume profile with smaller particles preferentially reaching higher altitudes. The degree of stratification varies with orbital phase and from orbit to another.

The combined information on the velocity and size distribution of plume particles should further advance our knowledge of the vent dynamics at the south pole of Enceladus. For example, both the average particle size and the typical launch velocity of the particles tend to increase as Enceladus crosses its orbital apocenter, with the launch velocities and particle sizes only decreasing at orbital phases beyond 300°. These coordinated changes may both reflect systematic variations in the width of the vents at the south pole. That is, as the cracks open near apocenter, this could lead to increases in both particle size and velocity, but as the cracks shut down the pressure in the system is enough to sustain higher velocities and larger particles until the moon gets within 60 degrees of pericenter.

The vent dynamics can be used to understand the connection between the ocean and Enceladus' surface. According to the gravity field measurements and the rotational asymmetries, Enceladus may be inferred to have a differentiated interior consisting of a low-density rocky core (with an estimated radius of 191–198 km) that is contact with a global sub-surface liquid water ocean (Iess *et al*., 2014; McKinnon, 2015). Iess *et al*. (2014) used long-range data collected by the Cassini spacecraft to construct a gravity model of Enceladus and suggested the presence of a large, subsurface ocean 30 to 40 km deep. The ice shell thickness is found to be variable

using a combination of observed libration amplitude and measurement of Enceladus' topography (Thomas *et al*., 2016; Nimmo *et al*., 2011) and may be only a few kilometers thick at the south pole (Čadek *et al*., 2016). Tidal heating in combination with a porous core throughout which water can circulate is thought to be the main heat source, preventing quick freezing of the subsurface ocean (Nimmo *et al*., 2014; Roberts, 2015). The temperature of the ocean is expected to be near the freezing point of pure water ($\approx 0\ ^{\circ}C$) and with only small variations with the change in ice thickness ($0.1\ ^{\circ}C$) (Zeng and Jansen, 2021). Freezing of the water surface may be avoided by water vapor pressure buildup over the water surface, due to a combination of dissipative heating of water and a combination of the narrowing of the fractures toward the surface and viscous throttling of the escaping vapor (Postberg *et al*., 2009; Ingersoll and Pankine, 2010; Nakajima and Ingersoll, 2016; Yeoh *et al*., 2015; Kite and Rubin, 2016; Schenk *et al*., 2018).

The characteristics of the plume's particles and gases are clues to the physical and chemical processes at the ocean-gas interface. For example, Postberg *et al*. (2009, 2011a) suggest that different particles in the plume could have different origins, with smaller ice-rich grains condensing from the vapor phase and larger grains erupting from the liquid water surface. Nakajima and Ingersoll (2016) and Porco *et al*. (2017) also suggested the process of controlled boiling involving bubbles at the surface could launch micrometer-sized particles from the ocean. These different particle populations could be consistent with the variations in the size stratification we observe in the plume, and could therefore further constrain the subsurface conditions. We observed a slight decrease in the overall average particle size as altitude increases showing smaller particles reaching higher altitudes, implying stratification in the plume. For example, if the larger particles launched at lower speeds do in fact come from the water interface, while the faster small particles are formed in the vapor, then the variations in the relative amounts of these particles should constrain the depth of the water surface within these cracks. This is relevant to future exploration of the potentially habitable environments where in missions can be planned to use these grains to assess conditions in the subsurface ocean.

Observations of activity on Europa may play out in a similar manner to Enceladus. Plume activity on Europa has been observed by the Hubble Space telescope and Keck observatory (Roth *et al.*, 2014; Sparks *et al.*, 2016, 2017, 2019; Paganini *et al.*, 2020). Europa's activity may be more sporadic and less energetic than Enceladus, indicating that eccentricity-driven tidal stress is not the only source controlling the plumes on Europa. It is likely that any plume material on Europa originates in discrete fluid pockets perched at shallow levels in the ice shell, rather than directly from the ocean (Manga and Wang, 2007). The current data shows evidence for vapor plumes and that the only evidence for particle plumes are potential deposits on Europa's surface (Fagents *et al.*, 2000; Phillips *et al.*, 2000; Quick and Hedman, 2020). If our observations of Enceladus imply that the water surface on Enceladus is relatively shallow, there might be similarities between the plumbing system behind the plumes at the two moons. It is important to note that the study of the Enceladus plume in this dissertation constrain primarily conditions near the vent and don't provide strong constraints as to whether the ocean is deep or shallow. It would be interesting to know if there exists similar temporal evolution in Europa's plume and how the properties of particle vary on difference scales compared to Enceladus. Such a comparison could help narrow down the subsurface conditions on the two moons.

The methodology discussed in this work have a wider range of applications and can be expanded on for future research. The studies discussed in this work assumed that the particles in the plume have a spherical shape. Further studies of the spectral particles could also reveal whether the plume particles are compact grains or loose aggregates of smaller particles. For example, the machine learning methodology could be expanded by adding new features to the model. These new features can contain information about the possible aggregate populations such as size, and numbers. Since a machine learning model is capable of learning from large amount of data to find the best fit for observed spectra, we can potentially test for an extremely large parameter set. Similarly, composition information can also be added to the model. The current Mie scattering theory only takes into account the refractive index of water-ice and hence we were able to simulate the water-ice absorption band clearly in the theoretical data. A new element or compound or

even ratio of multiple compounds can be used to calculate theoretical spectra for many possible combinations. For example, the absorption bands of water vapor and carbon dioxide are in a similar range of wavelength value (from 2.3 μm to 5.6 μm). The refractive indices of these compounds can be used to calculate theoretical spectra. All these additional data would make for a comprehensive machine learning model, which can be generalized to spectral data of E-ring too. One potential issue would be the noise in the data we might need to come up with even better ways to handle data with low signal-to-noise.

Now that we have some information about the variations in average particle size and velocity, the next step of the process could be to map these variation to the specific features on the south pole of Enceladus. The detailed shape of the absorption band and the shape of spectra at shorter wavelengths differs from fissure to fissure (Dhingra *et al*., 2017; Hedman *et al*., 2018), which reflects differences in the particle size distribution of the material from different fissures. Porco *et al*. (2014) identified over 100 discrete jets that are time-variable in ways that are not obviously related to the tidal modulation of the plume as a whole. The spatial distribution of particles could hint at whether the solids are lifted mainly in jets or curtains. The question is could this data be resolved enough to facilitate this mapping to surface features? I believe we would need additional data such as from a different instrument maybe ISS images that will need to be merged with VIMS data on similar dates and positions to reach at this level of granularity.

Another area where the methods discussed in these papers can be applied is JWST data, the James Webb Space Telescope (JWST) is a space observatory launched by NASA. JWST is expected to revolutionize our understanding of the universe. It is designed to be one of the most powerful and advanced space telescopes ever built, specifically optimized for studying the universe in the infrared spectrum. JWST's primary goals include studying the early universe, the formation of stars and planetary systems, the atmospheres of exoplanets, and more. JWST is equipped with a suite of scientific instruments including the Near Infrared Camera (NIRCam), Near Infrared Spectrograph (NIRSpec), Mid-Infrared Instrument (MIRI), and the Near Infrared Imager and Slitless Spectrograph (NIRISS) providing with

a whole host of spectral data (Sabelhaus and Decker, 2004). JWST will collect (and is collecting) various types of data, including images, spectra, and time series observations (Pontoppidan *et al*., 2022; Schaerer *et al*., 2022; Rustamkulov *et al*., 2022). After obtaining JWST data, we typically need to reduce and process the data to extract scientifically meaningful information. This involves calibration, correcting for instrument artifacts, and extracting spectra or images from raw data. The methodologies applied to reduce noise in spectra data in all three papers can be replicated and advanced to study data collected by other spectrometers. The techniques to improve the signal to noise can be beneficial to spectroscopy especially in planetary science.

Bibliography

Berg O.E. 1978. A lunar terminator configuration. Earth and planetary science letters 39:377–381.

Blum J., Levasseur-Regourd A.C., Muñoz O., Slobodrian R., and Vedernikov A. 2008. Dust in space. Europhysics news 39:27–29.

Brilliantov N.V., Schmidt J., and Spahn F. 2008. Geysers of enceladus: Quantitative analysis of qualitative models. Planetary and Space Science 56:1596–1606.

Brown R.H., Baines K.H., Bellucci G., Bibring J.P., Buratti B.J., Capaccioni F., Cerroni P., Clark R.N., Coradini A., Cruikshank D.P., *et al*. 2004. The cassini visual and infrared mapping spectrometer (vims) investigation. Space Science Reviews 115:111–168.

Brown R.H., Clark R.N., Buratti B.J., Cruikshank D.P., Barnes J.W., Mastrapa R.M., Bauer J., Newman S., Momary T., *et al*. 2006. Composition and physical properties of enceladus' surface. Science 311:1425–1428.

Čadek O., Tobie G., Van Hoolst T., Massé M., Choblet G., Lefèvre A., Mitri G., Baland R.M., Běhounková M., Bourgeois O., *et al*. 2016. Enceladus's internal ocean and ice shell constrained from cassini gravity, shape, and libration data. Geophysical Research Letters 43:5653–5660.

Chavez Jr P.S. 1988. An improved dark-object subtraction technique for atmospheric scattering correction of multispectral data. Remote sensing of environment 24:459–479.

Clark R.N., Brown R.H., Lytle D.M., and Hedman M. 2018. The vims wavelength and radiometric calibration 19, final report. NASA Planetary Data System .

Colaprete A., Vargo K., Shirley M., Land is D., Wooden D., Karcz J., Hermalyn B., and Cook A. 2014. An Overview of the LADEE Ultraviolet-Visible Spectrometer. Scientific Studies of Reading 185:63–91.

Colaprete A., Vargo K., Shirley M., Landis D., Wooden D., Karcz J., Hermalyn B., and Cook A. 2015. An overview of the ladee ultraviolet-visible spectrometer. *In* The Lunar Atmosphere and Dust Environment Explorer Mission (LADEE), pages 63–91, Springer.

Collins G.C. and Goodman J.C. 2007. Enceladus' south polar sea. Icarus 189:72–82.

Colwell J., Batiste S., Horányi M., Robertson S., and Sture S. 2007. Lunar surface: Dust dynamics and regolith mechanics. Reviews of Geophysics 45.

Colwell J.E., Robertson S.R., Horányi M., Wang X., Poppe A., and Wheeler P. 2009. Lunar dust levitation. Journal of Aerospace Engineering 22:2–9.

Criswell D.R. 1973. Horizon-glow and the motion of lunar dust. *In* Photon and particle interactions with surfaces in space, pages 545–556, Springer.

Degruyter W. and Manga M. 2011. Cryoclastic origin of particles on the surface of enceladus. Geophysical research letters 38.

Dhingra D., Hedman M.M., Clark R.N., and Nicholson P.D. 2017. Spatially resolved near infrared observations of enceladus' tiger stripe eruptions from cassini vims. Icarus 292:1–12.

Dohnanyi J. 1969. Collisional model of asteroids and their debris. Journal of Geophysical Research 74:2531–2554.

Dougherty M., Khurana K., Neubauer F., Russell C., Saur J., Leisner J., and Burton M. 2006. Identification of a dynamic atmosphere at enceladus with the cassini magnetometer. Science .

Fagents S.A., Greeley R., Sullivan R.J., Pappalardo R.T., Prockter L.M., Team G.S., *et al*. 2000. Cryomagmatic mechanisms for the formation of rhadamanthys linea, triple band margins, and other low-albedo features on europa. Icarus 144:54–88.

Feldman P.D., Glenar D.A., Stubbs T.J., Retherford K.D., Gladstone G.R., Miles P.F., Greathouse T.K., Kaufmann D.E., Parker J.W., and Stern S.A. 2014. Upper limits for a lunar dust exosphere from far-ultraviolet spectroscopy by lro/lamp. Icarus 233:106–113.

Fymat A. and Mease K. 1981. Mie forward scattering: improved semiempirical approximation with application to particle size distribution inversion. Applied optics 20:194–198.

Gaier J.R. 2007. The effects of lunar dust on eva systems during the apollo missions. Tech. rep., National Aeronautics and Space Administration.

Glenar D.A., Stubbs T.J., Hahn J.M., and Wang Y. 2014. Search for a high-altitude lunar dust exosphere using clementine navigational star tracker measurements. Journal of Geophysical Research: Planets 119:2548–2567.

Glenar D.A., Stubbs T.J., McCoy J.E., and Vondrak R.R. 2011. A reanalysis of the Apollo light scattering observations, and implications for lunar exospheric dust. Planetary and Space Science 59:1695–1707.

Goguen J.D., Buratti B.J., Brown R.H., Clark R.N., Nicholson P.D., Hedman M.M., Howell R.R., Sotin C., Cruikshank D.P., Baines K.H., *et al*. 2013. The temperature and width of an active fissure on enceladus measured with cassini vims during the 14 april 2012 south pole flyover. Icarus 226:1128–1137.

Goldstein D.B., Hedman M., Manga M., Perry M., Spitale J., and Teolis B. 2018. Enceladus plume dynamics: from surface to space. Enceladus and the Icy Moons of Saturn pages 175–194.

Grün E., Horanyi M., and Sternovsky Z. 2011. The lunar dust environment. Planetary and Space Science 59:1672–1680.

Hansen C., Esposito L., Aye K.M., Colwell J., Hendrix A., Portyankina G., and Shemansky D. 2017. Investigation of diurnal variability of water vapor in enceladus' plume by the cassini ultraviolet imaging spectrograph. Geophysical Research Letters 44:672–677.

Hansen C., Shemansky D.E., Esposito L.W., Stewart A., Lewis B., Colwell J., Hendrix A., West R.A., Waite Jr J., Teolis B., *et al*. 2011. The composition and structure of the enceladus plume. Geophysical Research Letters 38.

Hansen C.J., Esposito L., Stewart A., Colwell J., Hendrix A., Pryor W., Shemansky D., and West R. 2006. Enceladus' water vapor plume. Science .

Hedman M., Dhingra D., Nicholson P., Hansen C., Portyankina G., Ye S., and Dong Y. 2018. Spatial variations in the dust-to-gas ratio of enceladus' plume. Icarus 305:123–138.

Hedman M., Gosmeyer C., Nicholson P., Sotin C., Brown R., Clark R., Baines K., Buratti B., and Showalter M. 2013. An observed correlation between plume activity and tidal stresses on enceladus. Nature 500:182–184.

Hedman M., Nicholson P., Showalter M., Brown R.H., Buratti B., and Clark R. 2009. Spectral observations of the enceladus plume with cassini-vims. The Astrophysical Journal 693:1749.

Hedman M.M., Nicholson P.D., Showalter M.R., Brown R.H., Buratti B.J., and Clark R.N. 2009. Spectral Observations of the Enceladus Plume with Cassini-Vims. The Astrophysical Journal 693:1749–1762.

Helfenstein P. and Porco C.C. 2015. Enceladus' Geysers: Relation to Geological Features. 150:96.

Horányi M., Burns J., Hedman M., Jones G., and Kempf S. 2009. Diffuse rings. Saturn from Cassini-Huygens pages 511–536.

Horányi M., Juhász A., and Morfill G.E. 2008. Large-scale structure of saturn's e-ring. Geophysical Research Letters 35.

Horányi M., Szalay J., Kempf S., Schmidt J., Grün E., Srama R., and Sternovsky Z. 2015. A permanent, asymmetric dust cloud around the moon. Nature 522:324–326.

Hurford T., Helfenstein P., Hoppa G., Greenberg R., and Bills B. 2007. Eruptions arising from tidally controlled periodic openings of rifts on enceladus. Nature 447:292–294.

Hurford T.A., Helfenstein P., Hoppa G.V., Greenberg R., and Bills B.G. 2007. Eruptions arising from tidally controlled periodic openings of rifts on Enceladus. 447:292–294.

Hurford T.A., Helfenstein P., and Spitale J.N. 2012. Tidal control of jet eruptions on Enceladus as observed by Cassini ISS between 2005 and 2007. 220:896–903.

Iess L., Stevenson D., Parisi M., Hemingway D., Jacobson R., Lunine J., Nimmo F., Armstrong J., Asmar S., Ducci M., *et al*. 2014. The gravity field and interior structure of enceladus. Science 344:78–80.

Immer C., Lane J., Metzger P., and Clements S. 2011. Apollo video photogrammetry estimation of plume impingement effects. Icarus 214:46–52.

Ingersoll A.P. and Ewald S.P. 2011. Total particulate mass in enceladus plumes and mass of saturn's e ring inferred from cassini iss images. Icarus 216:492–506.

Ingersoll A.P. and Ewald S.P. 2017. Decadal timescale variability of the enceladus plumes inferred from cassini images. Icarus 282:260–275.

Ingersoll A.P., Ewald S.P., and Trumbo S.K. 2020. Time variability of the enceladus plumes: Orbital periods, decadal periods, and aperiodic change. Icarus 344:113345.

Ingersoll A.P. and Pankine A.A. 2010. Subsurface heat transfer on enceladus: Conditions under which melting occurs. Icarus 206:594–607.

Jackson J. 1975. Multipoles, electrostatics of macroscopic media, dielectrics. Classical electrodynamics, 2nd edn. Wiley, Inc., New York .

Jackson J.D. 1999. Classical electrodynamics.

Jaumann R., Stephan K., Hansen G., Clark R., Buratti B., Brown R., Baines K., Newman S., Bellucci G., Filacchione G., *et al*. 2008. Distribution of icy particles across enceladus' surface as derived from cassini-vims measurements. Icarus 193:407–419.

Kaltenegger L., Selsis F., Fridlund M., Lammer H., Beichman C., Danchi W., Eiroa C., Henning T., Herbst T., Léger A., *et al*. 2010. Deciphering spectral fingerprints of habitable exoplanets. Astrobiology 10:89–102.

Kempf S., Beckmann U., and Schmidt J. 2010. How the enceladus dust plume feeds saturn's e ring. Icarus 206:446–457.

Khan-Mayberry N. 2008. The lunar environment: Determining the health effects of exposure to moon dusts. Acta Astronautica 63:1006–1014.

Khurana K.K., Dougherty M.K., Russell C.T., and Leisner J.S. 2007. Mass loading of saturn's magnetosphere near enceladus. Journal of Geophysical Research: Space Physics 112.

Kieffer S.W., Lu X., Bethke C.M., Spencer J.R., Marshak S., and Navrotsky A. 2006. A clathrate reservoir hypothesis for enceladus' south polar plume. Science 314:1764–1766.

Kite E.S. and Rubin A.M. 2016. Sustained eruptions on Enceladus explained by turbulent dissipation in tiger stripes. Proceedings of the National Academy of Science 113:3972–3975.

Kite E.S. and Rubin A.M. 2016. Sustained eruptions on enceladus explained by turbulent dissipation in tiger stripes. Proceedings of the National Academy of Sciences 113:3972–3975.

Kolokolnikov I., Nepomnyashchaya E., and Velichko E. 2019. Static light scattering for determination of physical parameters of macro-and nanoparticles. *In* Journal of Physics: Conference Series, vol. 1410, page 012168, IOP Publishing.

Kolokolova L., Hough J., and Levasseur-Regourd A.C. 2015. Polarimetry of Stars and Planetary Systems. Cambridge University Press.

Lane J.E. and Metzger P.T. 2012. Ballistics model for particles on a horizontal plane in a vacuum propelled by a vertically impinging gas jet. Particulate Science and Technology 30:196–208.

Lasue J., Levasseur-Regourd A.C., and Renard J.B. 2020. Zodiacal light observations and its link with cosmic dust: A review. Planetary and Space Science 190:104973.

Leinert C., Bowyer S., Haikala L.K., Hanner M.S., Hauser M.G., Levasseur-Regourd A.C., Mann I., Mattila K., Reach W.T., Schlosser W., Staude H.J., Toller G.N., Weiland J.L., Weinberg J.L., and Witt A.N. 1998. The 1997 reference of diffuse night sky brightness. Astronomy and Astrophysics Supplement Series 127:1–99.

Manga M. and Wang C.Y. 2007. Pressurized oceans and the eruption of liquid water on europa and enceladus. Geophysical Research Letters 34.

Mastrapa R., Sandford S., Roush T., Cruikshank D., and Dalle Ore C. 2009. Optical constants of amorphous and crystalline h20-ice: 2.5–22 μm (4000–455 cm- 1) optical constants of h20-ice. The Astrophysical Journal 701:1347.

Mastrapa R.M., Sandford S.A., Roush T.L., Cruikshank D.P., and Dalle Ore C.M. 2009. Optical Constants of Amorphous and Crystalline H_2O-ice: 2.5-22 μm (4000-455 cm^{-1}) Optical Constants of H_2O-ice. 701:1347–1356.

Mccord T.B., Coradini A., Hibbitts C., Capaccioni F., Hansen G.B., Filacchione G., Clark R.N., Cerroni P., Brown R.H., Baines K.H., *et al*. 2004. Cassini vims observations of the galilean satellites including the vims calibration procedure. Icarus 172:104–126.

McCoy J.E. 1976. Photometric studies of light scattering above the lunar terminator from apollo solar corona photography. *In* Lunar and planetary science conference proceedings, vol. 7, pages 1087–1112.

McKay D.S., Heiken G., Basu A., Blanford G., Simon S., Reedy R., French B.M., and Papike J. 1991. The lunar regolith. Lunar sourcebook 567:285–356.

McKinnon W.B. 2015. Effect of enceladus's rapid synchronous spin on interpretation of cassini gravity. Geophysical Research Letters 42:2137–2143.

Mecherikunnel A.T. and Richmond J.C. 1980. Spectral distribution of Solar radiation. NASA Goddard Space Flight Center).

Metzger P. 2020. Dust transport and its effect due to landing spacecraft. LPICo 2141:5040.

Michael Holland J. and Simmonds R.C. 1973. The mammalian response to lunar particulates. Space life sciences 4:97–109.

Murphy D. and Vondrak R. 1993. Effects of levitated dust on astronomical observations from the lunar surface. *In* American Astronomical Society, 182nd AAS Meeting, id. 51.21; Bulletin of the American Astronomical Society, Vol. 25, p. 889, vol. 25, page 889.

Nakajima M. and Ingersoll A.P. 2016. Controlled boiling on enceladus. 1. model of the vapor-driven jets. Icarus 272:309–318.

Nimmo F., Bills B., and Thomas P. 2011. Geophysical implications of the long-wavelength topography of the saturnian satellites. Journal of Geophysical Research: Planets 116.

Nimmo F., Porco C., and Mitchell C. 2014. Tidally modulated eruptions on enceladus: Cassini iss observations and models. The Astronomical Journal 148:46.

Nimmo F., Spencer J., Pappalardo R., and Mullen M. 2007. Shear heating as the origin of the plumes and heat flux on enceladus. Nature 447:289–291.

Orger N.C., Cordova Alarcon J.R., Toyoda K., and Cho M. 2018. Lunar dust lofting due to surface electric field and charging within Micro-cavities between dust grains above the terminator region. Advances in Space Research 62:896–911.

Paganini L., Villanueva G.L., Roth L., Mandell A., Hurford T., Retherford K.D., and Mumma M.J. 2020. A measurement of water vapour amid a largely quiescent environment on europa. Nature Astronomy 4:266–272.

Phillips C.B., McEwen A.S., Hoppa G.V., Fagents S.A., Greeley R., Klemaszewski J.E., Pappalardo R.T., Klaasen K.P., and Breneman H.H. 2000. The search for current geologic activity on europa. Journal of Geophysical Research: Planets 105:22579–22597.

Pohlen M., Carroll D., Prisk G.K., and Sawyer A.J. 2022. Overview of lunar dust toxicity risk. npj Microgravity 8:55.

Pokornỳ P., Janches D., Sarantos M., Szalay J.R., Horányi M., Nesvornỳ D., and Kuchner M.J. 2019. Meteoroids at the moon: orbital properties, surface vaporization, and impact ejecta production. Journal of Geophysical Research: Planets 124:752–778.

Pollack J.B. and Cuzzi J.N. 1980. Scattering by nonspherical particles of size comparable to a wavelength: A new semi-empirical theory and its application to tropospheric aerosols. Journal of the Atmospheric Sciences 37:868–881.

Pontoppidan K.M., Barrientes J., Blome C., Braun H., Brown M., Carruthers M., Coe D., DePasquale J., Espinoza N., Marin M.G., *et al*. 2022. The jwst early release observations. The Astrophysical Journal Letters 936:L14.

Popel S., Zelenyi L., Dubinskii A.Y., *et al*. 2018. Lunar dust and dusty plasmas: Recent developments, advances, and unsolved problems. Planetary and Space Science 156:71–84.

Popel S.I., Lisin E., Izvekova Y.N., Atamaniuk B., Dol'nikov G., Zakharov A., Zelenyi L., *et al*. 2016. Impacts of fast meteoroids and the separation of dust particles from the surface of the moon. JETP letters 103:563–567.

Porco C., DiNino D., and Nimmo F. 2014. How the geysers, tidal stresses, and thermal emission across the south polar terrain of enceladus are related. The Astronomical Journal 148:45.

Porco C., Mitchell C., Nimmo F., and Tiscareno M. 2018. Enceladus' Plume Temporal Variability from Analysis of Cassini ISS Images. *In* 49th Annual Lunar and Planetary Science Conference, Lunar and Planetary Science Conference, page 2003.

Porco C.C., Dones L., and Mitchell C. 2017. Could it be snowing microbes on enceladus? assessing conditions in its plume and implications for future missions. Astrobiology 17:876–901.

Porco C.C., Helfenstein P., Thomas P., Ingersoll A., Wisdom J., West R., Neukum G., Denk T., Wagner R., Roatsch T., *et al*. 2006. Cassini observes the active south pole of enceladus. science .

Postberg F., Grün E., Horanyi M., Kempf S., Krüger H., Schmidt J., Spahn F., Srama R., Sternovsky Z., and Trieloff M. 2011a. Compositional mapping of planetary moons by mass spectrometry of dust ejecta. Planetary and Space Science 59:1815–1825.

Postberg F., Kempf S., Hillier J., Srama R., Green S., McBride N., and Grün E. 2008. The e-ring in the vicinity of enceladus: Ii. probing the moon's interior—the composition of e-ring particles. Icarus 193:438–454.

Postberg F., Kempf S., Schmidt J., Brilliantov N., Beinsen A., Abel B., Buck U., and Srama R. 2009. Sodium salts in e-ring ice grains from an ocean below the surface of enceladus. Nature 459:1098–1101.

Postberg F., Schmidt J., Hillier J., Kempf S., and Srama R. 2011b. A salt-water reservoir as the source of a compositionally stratified plume on enceladus. Nature 474:620–622.

Quanz S.P., Absil O., Benz W., Bonfils X., Berger J.P., Defrère D., van Dishoeck E., Ehrenreich D., Fortney J., Glauser A., *et al*. 2021. Atmospheric characterization of terrestrial exoplanets in the mid-infrared: biosignatures, habitability, and diversity. Experimental astronomy pages 1–25.

Quick L.C. and Hedman M.M. 2020. Characterizing deposits emplaced by cryovolcanic plumes on europa. Icarus 343:113667.

Raponi A., De Sanctis M.C., Giacomo Carrozzo F., Ciarniello M., Rousseau B., Ferrari M., Ammannito E., De Angelis S., Vinogradoff V., Castillo-Rogez J.C., *et al*. 2021. Organic material on ceres: Insights from visible and infrared space observations. Life 11:9.

Rennilson J. and Criswell D.R. 1974. Surveyor observations of lunar horizon-glow. The Moon 10:121–142.

Roberts D., Yamaguchi Y., and Lyon R. 1986. Comparison of various techniques for calibration of ais data. NASA STI/Recon Technical Report N 87:21–30.

Roberts J.H. 2015. The fluffy core of enceladus. Icarus 258:54–66.

Roth L., Saur J., Retherford K.D., Strobel D.F., Feldman P.D., McGrath M.A., and Nimmo F. 2014. Transient water vapor at europa's south pole. science 343:171–174.

Rustamkulov Z., Sing D.K., Liu R., and Wang A. 2022. Analysis of a jwst nirspec lab time series: characterizing systematics, recovering exoplanet transit spectroscopy, and constraining a noise floor. The Astrophysical Journal Letters 928:L7.

Sabelhaus P.A. and Decker J.E. 2004. An overview of the james webb space telescope (jwst) project. Optical, Infrared, and Millimeter Space Telescopes 5487:550–563.

Sarantos M., Killen R.M., Glenar D.A., Benna M., and Stubbs T.J. 2012. Metallic species, oxygen and silicon in the lunar exosphere: Upper limits and prospects for ladee measurements. Journal of Geophysical Research: Space Physics 117.

Schaerer D., Marques-Chaves R., Barrufet L., Oesch P., Izotov Y., Naidu R., Guseva N., and Brammer G. 2022. First look with jwst spectroscopy: Resemblance among z 8 galaxies and local analogs. Astronomy & Astrophysics 665:L4.

Schenk P.M., Clark R.N., Howett C.J., Verbiscer A.J., and Waite J.H. 2018. Enceladus and the icy moons of Saturn. University of Arizona Press.

Schmidt J. 2014. Plumes and Jets: Constraints on Vents and Eruption Dynamics from Observations and Models. *In* AGU Fall Meeting Abstracts, vol. 2014, pages P51F–05.

Schmidt J., Brilliantov N., Spahn F., and Kempf S. 2008. Slow dust in enceladus' plume from condensation and wall collisions in tiger stripe fractures. Nature 451:685–688.

Sharma H., Hedman M., and Vahidinia S. 2023. New insights into variations in enceladus plume particle launch velocities from cassini-vims spectral data. The Planetary Science Journal 4:108.

Shirley M. 2014. Lunar atmosphere and dust environment explorer (ladee) ultraviolet-visible spectrometer (uvs) archive bundle.

Shkuratov Y.G., Muinonen K., Bowell E., Lumme K., Peltoniemi J., Kreslavsky M., Stankevich D., Tishkovetz V., Opanasenko N., and Melkumova L.Y. 1994. A critical review of theoretical models of negatively polarized light scattered by atmosphereless solar system bodies. Earth, Moon, and Planets 65:201–246.

Shoemaker E.M. and Morris E. 1970. Physical characteristics of the lunar regolith determined from surveyor television observations. Radio Science 5:129–155.

Smith B.A., Soderblom L., Batson R., Bridges P., Inge J., Masursky H., Shoemaker E., Beebe R., Boyce J., Briggs G., *et al*. 1982. A new look at the saturn system: The voyager 2 images. Science 215:504–537.

Smith-Konter B. and Pappalardo R.T. 2008. Tidally driven stress accumulation and shear failure of enceladus's tiger stripes. Icarus 198:435–451.

Solomonidou A., Bampasidis G., Kyriakopoulos K., Bratsolis E., Hirtzig M., Coustenis A., and Moussas X. 2010. Imaging of potentially active geological regions on saturn's moons titan and enceladus, using cassini-huygens data: With emphasis on cryovolcanism. Hellenic J. Geosci 45:257–268.

Southworth B.S., Kempf S., and Spitale J. 2019. Surface deposition of the enceladus plume and the zenith angle of emissions. Icarus 319:33–42.

Spahn F., Schmidt J., Albers N., Horning M., Makuch M., Seiß M., Kempf S., Srama R., Dikarev V., Helfert S., *et al*. 2006. Cassini dust measurements at enceladus and implications for the origin of the e ring. Science .

Sparks W., Richter M., deWitt C., Montiel E., Russo N.D., Grunsfeld J., McGrath M., Weaver H., Hand K., Bergeron E., *et al*. 2019. A search for water vapor plumes on europa using sofia. The Astrophysical Journal Letters 871:L5.

Sparks W.B., Hand K., McGrath M., Bergeron E., Cracraft M., and Deustua S. 2016. Probing for evidence of plumes on europa with hst/stis. The Astrophysical Journal 829:121.

Sparks W.B., Schmidt B.E., McGrath M.A., Hand K.P., Spencer J.R., Cracraft M., and Deustua S.E. 2017. Active cryovolcanism on europa? The Astrophysical Journal Letters 839:L18.

Spencer J., Nimmo F., Ingersoll A.P., Hurford T., Kite E., Rhoden A., Schmidt J., and Howett C. 2018. Plume origins and plumbing: from ocean to surface. Enceladus and the icy moons of Saturn pages 163–174.

Spencer J., Pearl J., Segura M., Flasar F., Mamoutkine A., Romani P., Buratti B., Hendrix A., Spilker L., and Lopes R. 2006. Cassini encounters enceladus: Background and the discovery of a south polar hot spot. science .

Spitale J., Tigges M., Rhoden A., Hurford T., and Webster K. 2020. Curtain-Based Maps of Eruptive Activity in Enceladus' South-Polar Terrain at Fifteen Cassini Epochs. *In* AAS/Division for Planetary Sciences Meeting Abstracts, vol. 52 of *AAS/Division for Planetary Sciences Meeting Abstracts*, page 215.05.

Spitale J.N., Hurford T., and Rhoden A.R. 2017. Short-Term Variability in Enceladus' Plume. *In* AAS/Division for Planetary Sciences Meeting Abstracts #49, vol. 49 of *AAS/Division for Planetary Sciences Meeting Abstracts*, page 207.02.

Spitale J.N., Hurford T.A., Rhoden A.R., Berkson E.E., and Platts S.S. 2015. Curtain eruptions from enceladus' south-polar terrain. Nature 521:57–60.

Spitale J.N. and Porco C.C. 2007. Association of the jets of Enceladus with the warmest regions on its south-polar fractures. 449:695–697.

Spitale J.N. and Porco C.C. 2007. Association of the jets of enceladus with the warmest regions on its south-polar fractures. Nature 449:695–697.

Stubbs T., Vondrak R., and Farrell W. 2007. Impact of dust on lunar exploration. Dust in Planetary Systems pages 239–243.

Stubbs T.J., Glenar D.A., Colaprete A., and Richard D.T. 2010. Optical scattering processes observed at the moon: Predictions for the ladee ultraviolet spectrometer. Planetary and Space Science 58:830–837.

Sumlin B.J., Heinson W.R., and Chakrabarty R.K. 2018. Retrieving the aerosol complex refractive index using pymiescatt: A mie computational package with visualization capabilities. Journal of Quantitative Spectroscopy and Radiative Transfer 205:127–134.

Szalay J.R. and Horányi M. 2015. The search for electrostatically lofted grains above the moon with the lunar dust experiment. Geophysical Research Letters 42:5141–5146.

Szalay J.R. and Horányi M. 2016. Lunar meteoritic gardening rate derived from in situ ladee/ldex measurements. Geophysical Research Letters 43:4893–4898.

Tanaka H., Inaba S., and Nakazawa K. 1996. Steady-state size distribution for the self-similar collision cascade. icarus 123:450–455.

Teolis B.D., Perry M.E., Hansen C.J., Waite J.H., Porco C.C., Spencer J.R., and Howett C.J. 2017. Enceladus plume structure and time variability: Comparison of cassini observations. Astrobiology 17:926–940.

Thomas P., Tajeddine R., Tiscareno M., Burns J., Joseph J., Loredo T., Helfenstein P., and Porco C. 2016. Enceladus's measured physical libration requires a global subsurface ocean. Icarus 264:37–47.

Thomas-Keprta K.L., Clemett S.J., Messenger S., Ross D.K., Le L., Rahman Z., McKay D.S., Gibson Jr E.K., Gonzalez C., and Peabody W. 2014. Organic matter on the earth's moon. Geochimica et Cosmochimica Acta 134:1–15.

Tinetti G., Encrenaz T., and Coustenis A. 2013. Spectroscopy of planetary atmospheres in our galaxy. The Astronomy and Astrophysics Review 21:1–65.

Van de Hulst H. 1957. Light scattering by small particle, new york: John wiley & sons. Inc. pages 114–130.

von Paris P., Hedelt P., Selsis F., Schreier F., and Trautmann T. 2013. Characterization of potentially habitable planets: retrieval of atmospheric and planetary properties from emission spectra. arXiv preprint arXiv:1301.0217 .

Waite Jr J.H., Combi M.R., Ip W.H., Cravens T.E., McNutt Jr R.L., Kasprzak W., Yelle R., Luhmann J., Niemann H., Gell D., *et al*. 2006. Cassini ion and neutral mass spectrometer: Enceladus plume composition and structure. science .

Waite Jr J.H., Lewis W., Magee B., Lunine J., McKinnon W., Glein C., Mousis O., Young D., Brockwell T., Westlake J., *et al*. 2009. Liquid water on enceladus from observations of ammonia and 40ar in the plume. Nature 460:487–490.

Wang X., Schwan J., Hsu H.W., Grün E., and Horányi M. 2016. Dust charging and transport on airless planetary bodies. Geophysical Research Letters 43:6103–6110.

Wriedt T. 2012. Mie theory: a review. The Mie theory: Basics and applications pages 53–71.

Wright S.P., Tornabene L.L., Ramsey M.S., Osinski G., and Pierazzo E. 2013. Remote sensing of impact craters. Impact cratering: Processes and products pages 194–210.

Xie H., West R.A., Seignovert B., Jewell J., Kurth W., and Averkamp T. 2021. Compression algorithms for high-data-volume instruments on planetary missions: a case study for the cassini mission. Journal of Astronomical Telescopes, Instruments, and Systems 7:028002–028002.

Yeo L.H., Wang X., Deca J., Hsu H.W., and Horányi M. 2021. Dynamics of electrostatically lofted dust on airless planetary bodies. Icarus 366:114519.

Yeoh S.K., Chapman T.A., Goldstein D.B., Varghese P.L., and Trafton L.M. 2015. On understanding the physics of the enceladus south polar plume via numerical simulation. Icarus 253:205–222.

Yeoh S.K., Li Z., Goldstein D.B., Varghese P.L., Levin D.A., and Trafton L.M. 2017. Constraining the enceladus plume using numerical simulation and cassini data. Icarus 281:357–378.

Zakharov A., Zelenyi L., and Popel' S. 2020. Lunar dust: Properties and potential hazards. Solar System Research 54:455–476.

Zangwill A. 2013. Modern electrodynamics. Cambridge University Press.

Zeng Y. and Jansen M.F. 2021. Ocean circulation on enceladus with a high-versus low-salinity ocean. The Planetary Science Journal 2:151.

Zhang X., Zhang B., Geng X., Tong Q., and Zheng L. 2003. Automatic flat field algorithm for hyperspectral image calibration. *In* Third International Symposium on Multispectral Image Processing and Pattern Recognition, vol. 5286, pages 636–639, SPIE.

Zubko E., Videen G., Zubko N., and Shkuratov Y. 2017. Reflectance of micron-sized dust particles retrieved with the umov law. Journal of Quantitative Spectroscopy and Radiative Transfer 190:1–6.

APPENDIX A

Supplementary Information to Chapter 2: Constraining low-altitude lunar dust using the LADEE-UVS data

A.1 Formulas for computing predicted dust signals

Here we provide additional details about the formulas used to compute the predicted dust spectrum described in Section 2.3.3 above. For this analysis, we use the optical theorem to approximate the scattering law for a dust grain as:

$$\frac{dP}{d\Omega} = \frac{\pi F s^2}{4 sin^2\theta} J_1^2(k\, s\, sin\theta) Q_{ext}^2(k\, s, m) \tag{A.1}$$

where F is the incident flux density, s is the particle size (radius), k is the wave number of the light, θ is the scattering angle, which is 12° for our observations, and the factor of Q_{ext} in Equation A.1 is defined as follows Van de Hulst (1957):

$$Q_{ext} = 2 - 4e^{-\rho tan\beta} \frac{cos\beta}{\rho} \left[sin(\rho - \beta) + \frac{cos\beta}{\rho} cos(\rho - 2\beta) \right] + 4 \frac{cos^2\beta}{\rho^2} cos(2\beta), \tag{A.2}$$

where m is the complex refractive index of the particle ($m = m_r + i m_i$), $\rho = 2ks(m_r - 1)$ and $tan\beta = m_i/(m_r - 1)$. For these observations we assume a refractive index $m = 1.5 + i0.0005$ for a silicate-rich dust particle Zubko *et al.* (2017).

Since the dust above the Moon's surface is a collection of particles of different size ranges, we compute the unitless reflectance of this collection of particles with differential size distribution $\mathcal{N}(s,t)$ for wavelength channel i, with the following formula:

$$\left[\frac{I}{F}(t) \right]_{i,pred} = \frac{1}{F} \int_{s_{min}}^{s_{max}} \frac{dP_i}{d\Omega} \mathcal{N}(s,t) ds. \tag{A.3}$$

For this analysis, we consider both mono-disperse size distributions and power-law size distributions with differential power-law indices of -3 and -4 and limits of 0.3 to 10 μm.

For the specific case where, $\mathcal{N}(s,t) = c_o(t)s^{-3}$, c_o is a dimensionless function of time, but not particle size. The number of particles per unit area (m^{-2}), $N(t)$ is then given by the integral

$$N(t) = c_o(t) \int_{s_{min}}^{s_{max}} s^{-3} ds. \tag{A.4}$$

where $c_o(t)$ can be derived from equation A.3 such that

$$c_o(t) = \frac{[\frac{I}{F}(t)]_{i,pred}}{\frac{1}{F}\int_{s_{min}}^{s_{max}} \frac{dP_i}{d\Omega} s^{-3} ds}. \tag{A.5}$$

For reference, the value of the integral in the denominator for dust size from 0.3 (s_{min}) to 10 μm (s_{max}) for the wavelength range 250 - 300 nm is 21.0. This integral is worked out for all the wavelength ranges from 250 to 700 nm.

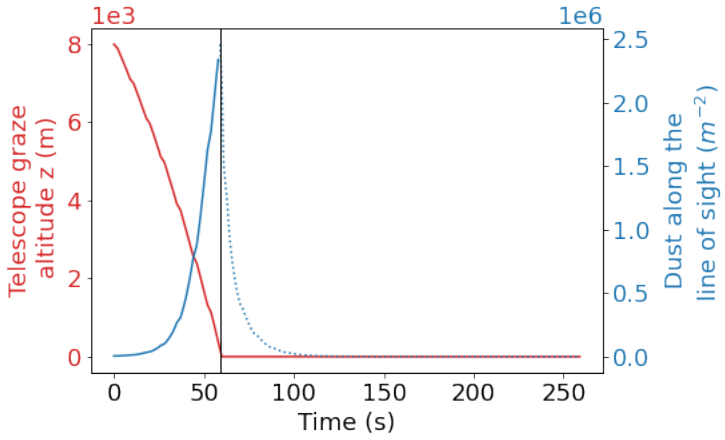

FIGURE A.1: The Telescope graze altitude (z) from Figure 2.1, as height of line of view at the point A (A in Figure 2.1) on the surface is shown by the red line plotted against time for the Almost Limb activity 1969A. This altitude is given in the LBL file associated with each Almost Limb activity. It reduces to zero as the field of view touches the Moon's surface, which is indicated by the vertical line on the plot. The blue line shows the integrated dust density calculated using equation A.6. The amount of dust per unit area does increase as altitude decreases until the line of sight meets the surface.

In order to compute the total amount of lunar dust visible at a given time along the line of sight, we assume an exponential dust profile defined by a nominal surface concentration $n_{o,nom}$ and scale height H. In this case, the total amount of dust along

the line of sight is given by the following integral along the line of sight x:

$$N(t) = n_{o,nom} \int_d^\infty e^{-a(x,t)/H} dx \tag{A.6}$$

where N is the number of particles per unit area and $a(x,t)$ is the altitude above the lunar surface, and d denotes the location where the light of sight crosses into sunlight (see Figure 2.1). Figure A.1 illustrates how this parameter (N) varies over the course of the observation, with a vertical line (t_V) denoting when the field of view hits the Moon's surface.

In order to determine the altitude $a(x,t)$ of the line of sight above the surface as a function of the coordinate x along the line of sight at any given time t, we use the parameters defined in Figure 2.1. The LBL data files associated with each spectrum gives the "telescope graze altitude" above the Moon's surface (denoted as z in Figure 2.1) and the latitude and longitude of points S (the spacecraft's location above the surface of the Moon) and A (the place where the line of sight gets closest to the Lunar surface). Figure A.1 shows how the graze altitude z changes over the course of the observation. It decreases gradually as the line of sight gets closer to the surface and reduced to zero as the line of sight hits the surface shown by the black vertical line on the plot. The terminator position T is calculated based on the sub-solar point on the Moon, which depends on the time at which the activity was performed.

Assuming the Moon to be a sphere, the height of the line of sight above the surface $a(x,t)$ can be written as the following function of x:

$$a(x,t) = \sqrt{x^2 + (z+R)^2} - R \tag{A.7}$$

where R is the radius of Moon (1737.4 km).

The lower limit d is calculated using the geometry shown in Figure 2.1. Considering the small triangle with legs l and d, we see that

$$d = \frac{l}{\tan \epsilon_1} \tag{A.8}$$

where ϵ_1 is equal to the solar elevation angle of point A (Figure 2.1):

$$\epsilon_1 = \sin^{-1}\Big[\sin\delta\sin\phi + \cos\delta\cos\phi\cos(HRA)\Big] \tag{A.9}$$

where δ is the sub-solar latitude angle, which depends on the time of the year and varies from (-0.5 to 0.5 deg for the Moon), ϕ is the latitude and HRA is the hour angle of point A . Meanwhile, the length l in Equation A.8 can be calculated from ϵ_1, z and R as

$$l = \frac{R}{\cos\epsilon_1} - (R+z). \tag{A.10}$$

Note, the values of l, ϵ_1 and d are evaluated separated for each spectra based on data provided in each LBL file.

In Figure A.1, we see how the integrated dust density increases with time as altitude decreases. This indicates that the amount of dust along the line of sight is higher at lower altitude which is what one would expect. The slow decrease in N after the line of view hits the surface (beyond the vertical line) is artificial because at that point the observable material would actually be blocked from view by the Moon.

Combining equation A.4 and A.6, an expressions for predicted signal is obtained:

$$n_{o,nom}\int_d^\infty e^{-a(x,t)/H}dx = c_o(t)\int_{s_{min}}^{s_{max}} s^{-3}ds. \tag{A.11}$$

Substituting in the above expression for $c_o(t)$ (equation A.5) and solving the integral for the size distribution $\mathcal{N}(s,t) \propto s^{-3}$, we find

$$n_{o,nom}\int_d^\infty e^{-(\sqrt{x^2+(z+R)^2}-R)/H}dx = \frac{\left[\frac{I}{F}\right]_{i,pred}}{\frac{1}{F}\int_{s_{min}}^{s_{max}}\frac{dP_i}{d\Omega}s^{-3}ds}\left(\frac{s_{max}^2 - s_{min}^2}{2s_{min}^2 s_{max}^2}\right). \tag{A.12}$$

Solving this equation for $[I/F]_{i,pred}$ gives the predicted signal for a given particle size distribution ($\mathcal{N}(s,t) \propto s^{-3}$) and wavelength channel i:

$$\left[\frac{I}{F}\right]_{i,pred} = n_{o,nom}\left[\frac{2s_{min}^2 s_{max}^2}{s_{max}^2 - s_{min}^2}\right]\left[\frac{1}{F}\int_{s_{min}}^{s_{max}}\frac{dP_i}{d\Omega}s^{-3}ds\right]\int_d^\infty e^{-(\sqrt{x^2+(z+R)^2}-R)/H}dx. \tag{A.13}$$

The above expression determines a predicted signal for a certain value of surface concentration ($n_{o,nom} = 10^3\ m^{-3}$ and scale heights H = 1, 3 and 5 km).

Repeating these calculations for a size distribution proportional to s^{-4}, Equation A.13 becomes

$$\left[\frac{I}{F}\right]_{i,pred} = n_{o,nom}\left[\frac{3s_{min}^3 s_{max}^3}{s_{max}^3 - s_{min}^3}\right]\left[\frac{1}{F}\int_{s_{min}}^{s_{max}} \frac{dP_i}{d\Omega} s^{-4} ds\right]\int_d^\infty e^{-(\sqrt{x^2+(z+R)^2}-R)/H} dx \tag{A.14}$$

and for a mono-disperse size distribution (0.07 to 1 μm) Equation A.13 changes to

$$\left[\frac{I}{F}\right]_{i,pred} = \frac{n_{o,nom}\pi s^2}{4sin^2\theta} J_1^2(k\,s\,sin\theta) Q_{ext}^2(k\,s,m)\int_d^\infty e^{-(\sqrt{x^2+(z+R)^2}-R)/H} dx. \tag{A.15}$$

A.2 PLOTS SHOWING THE MEASURED SIGNALS FOR ALL OBSERVATIONS AFTER SPECTRAL FILTERING

A.3 TABLES OF FIT PARAMETERS FOR ALL OBSERVATIONS

Table A.1 shows the slope between the residual and predicted signal and the standard deviation of this slope is calculated for each wavelength range. A weighted average of these slopes using their respective standard deviation as weights is computed for each observation. The weighted averaged slope with error bars at scale height of 1, 3 and 5 km are shown in this table. The intercept for this case is reduced to zero. Table A.1 and Figure A.10 also provide the Earth-Moon position details for these observations. The observed locations are farther and farther away from Earthshine horizon for the later data sets.

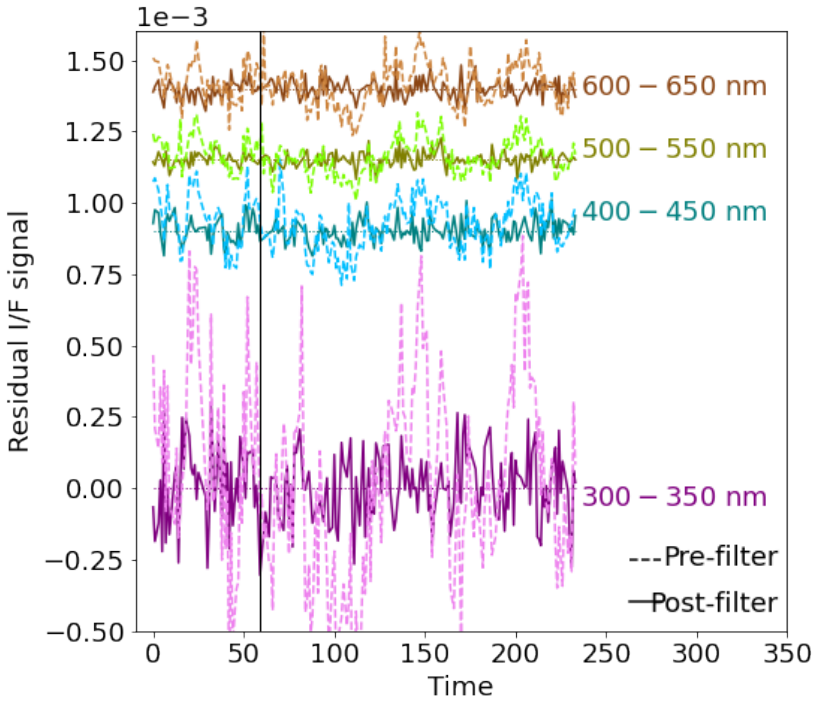

FIGURE A.2: Corrected signal (in solid) for the set "1918A", after spectral filtering has been applied to each wavelength range and the original spectrum (in dotted), plotted against time. An offset has been added here too to view each wavelength range distinctly.

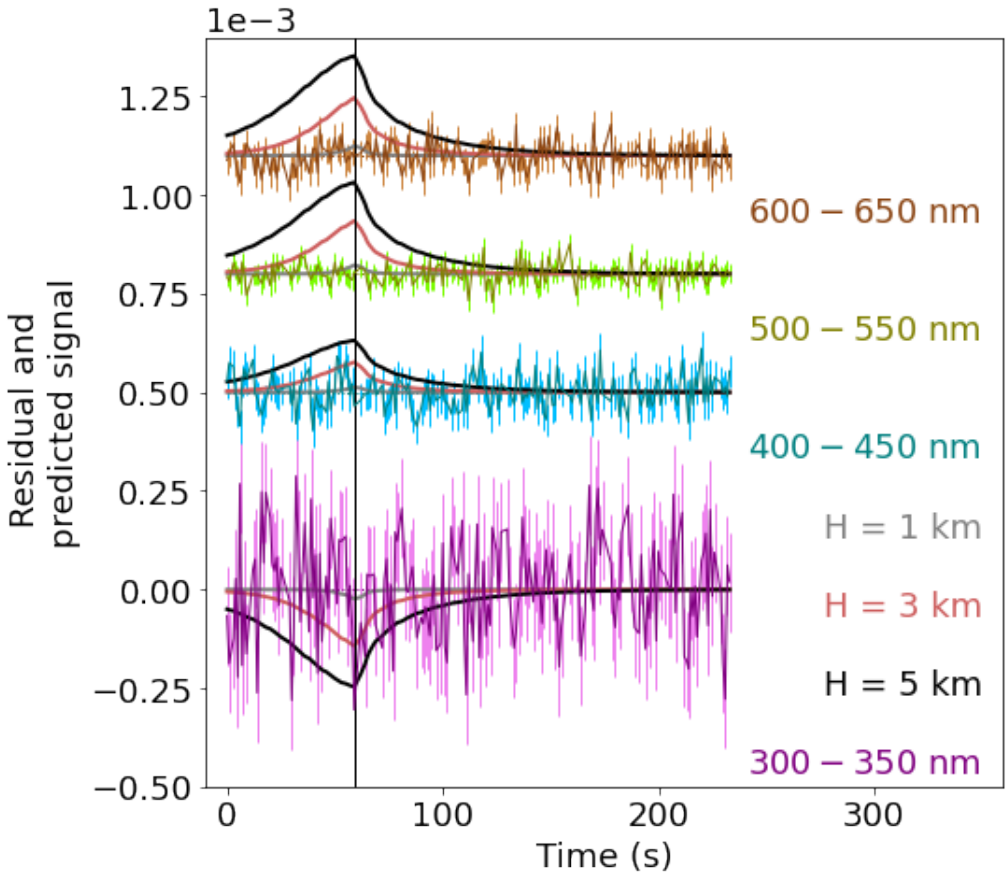

FIGURE A.3: This figure shows the filtered residual signal for "1918A" for each wavelength range. The signal predicted using the Fraunhofer model and the exponential density profile is plotted over the residual signal for a scale heights of 1, 3 and 5 km in grey, lightcoral and black respectively. An offset has been added to view the signals distinctly.

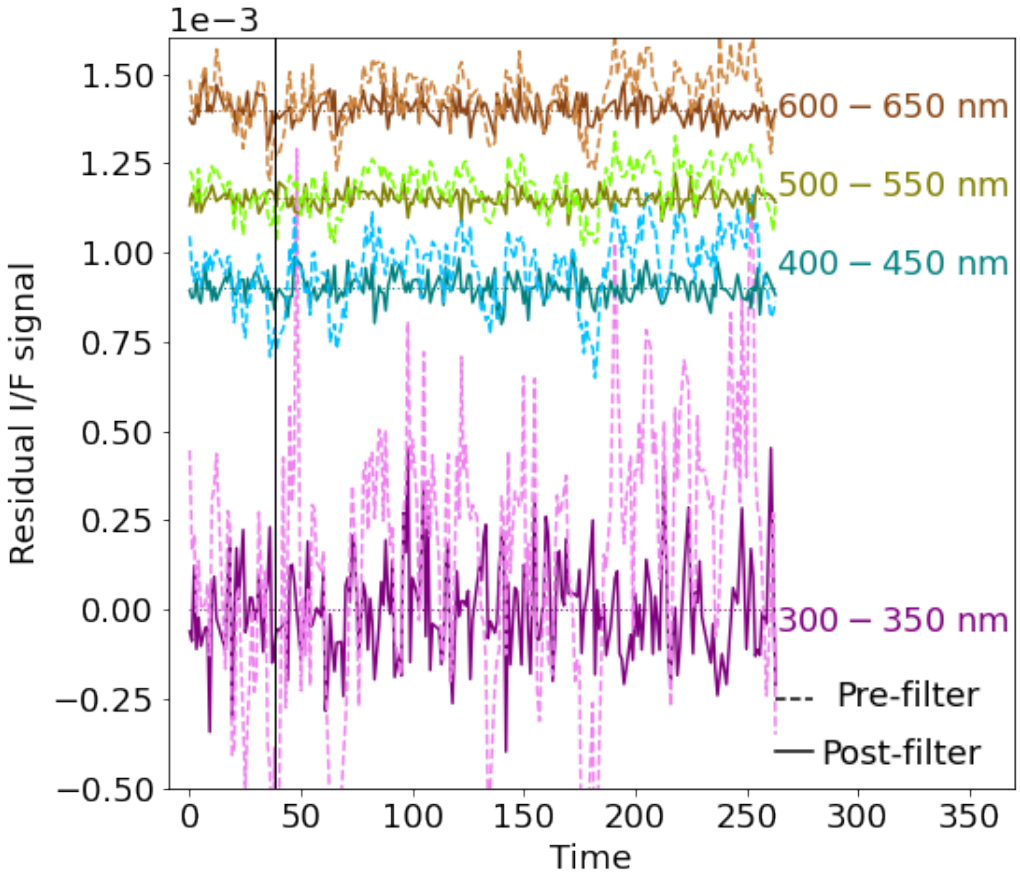

FIGURE A.4: Corrected signal (in solid) for the set "1929A", after spectral filtering has been applied to each wavelength range and the original spectrum(in dotted), plotted against time. An offset has been added here too to view each wavelength range distinctly.

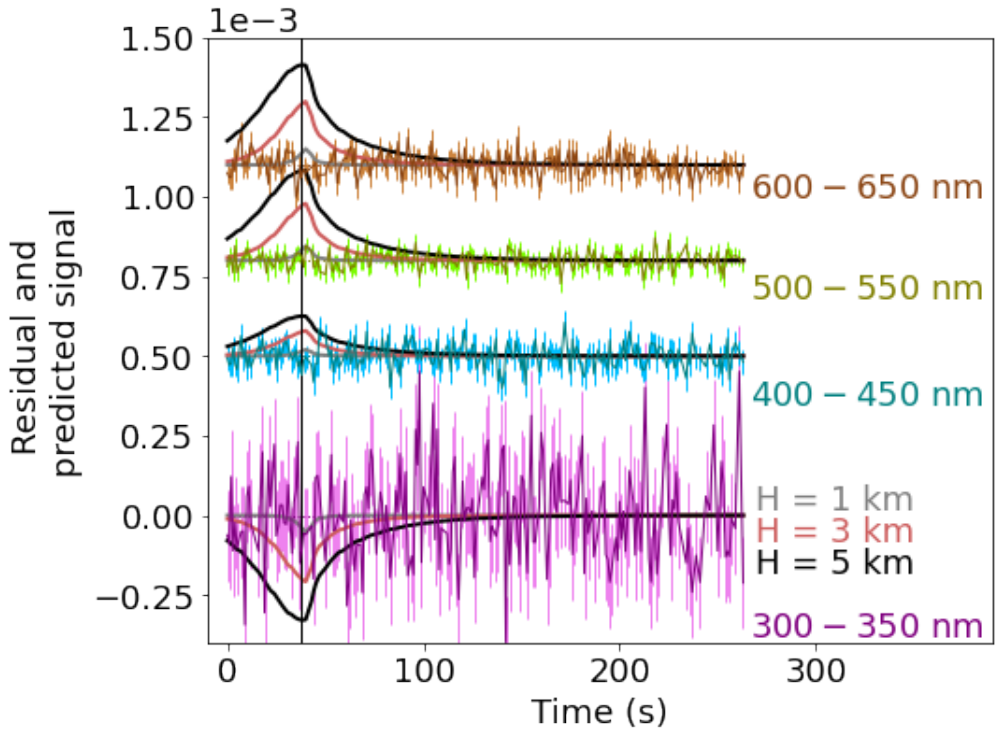

FIGURE A.5: This figure shows the filtered residual signal for "1929A" for each wavelength range. The signal predicted using the Fraunhofer model and the exponential density profile is plotted over the residual signal for a scale heights of 1, 3 and 5 km in grey, lightcoral and black respectively. An offset has been added to view the signals distinctly.

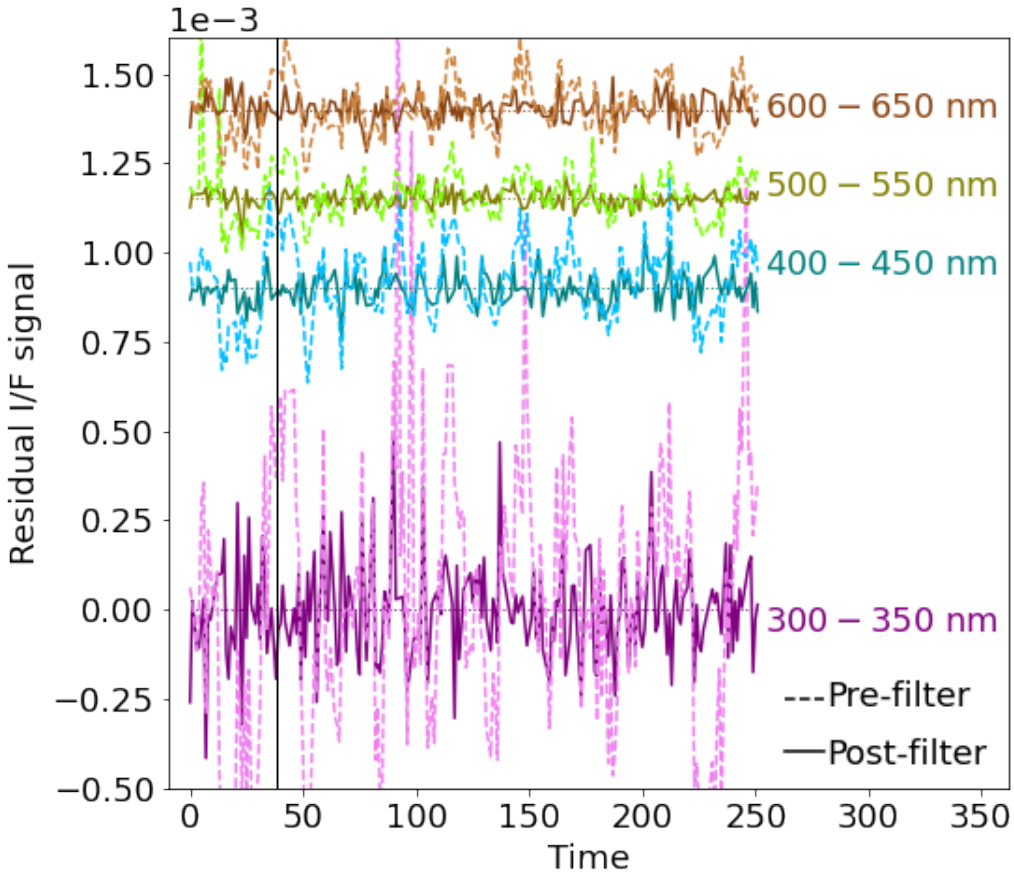

FIGURE A.6: Corrected signal (in solid) for the set "1956A", after spectral filtering has been applied to each wavelength range and the original spectrum(in dotted), plotted against time. An offset has been added here too to view each wavelength range distinctly.

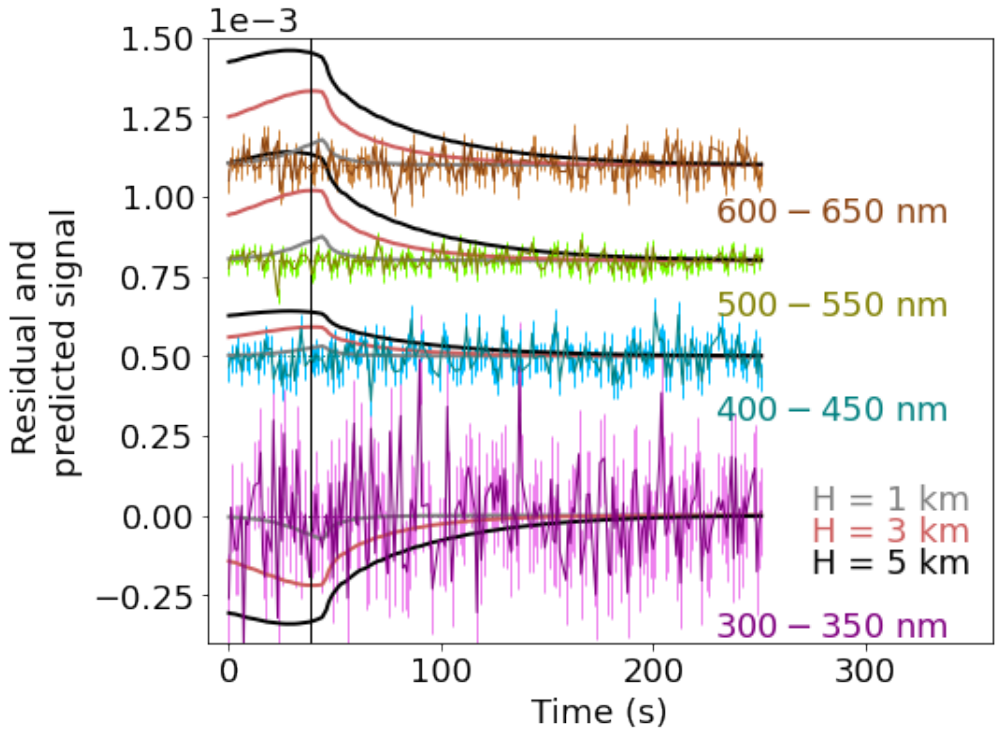

FIGURE A.7: This figure shows the filtered residual signal for "1956A" for each wavelength range. The signal predicted using the Fraunhofer model and the exponential density profile is plotted over the residual signal for a scale heights of 1, 3 and 5 km in grey, lightcoral respectively. An offset has been added to view the signals distinctly.

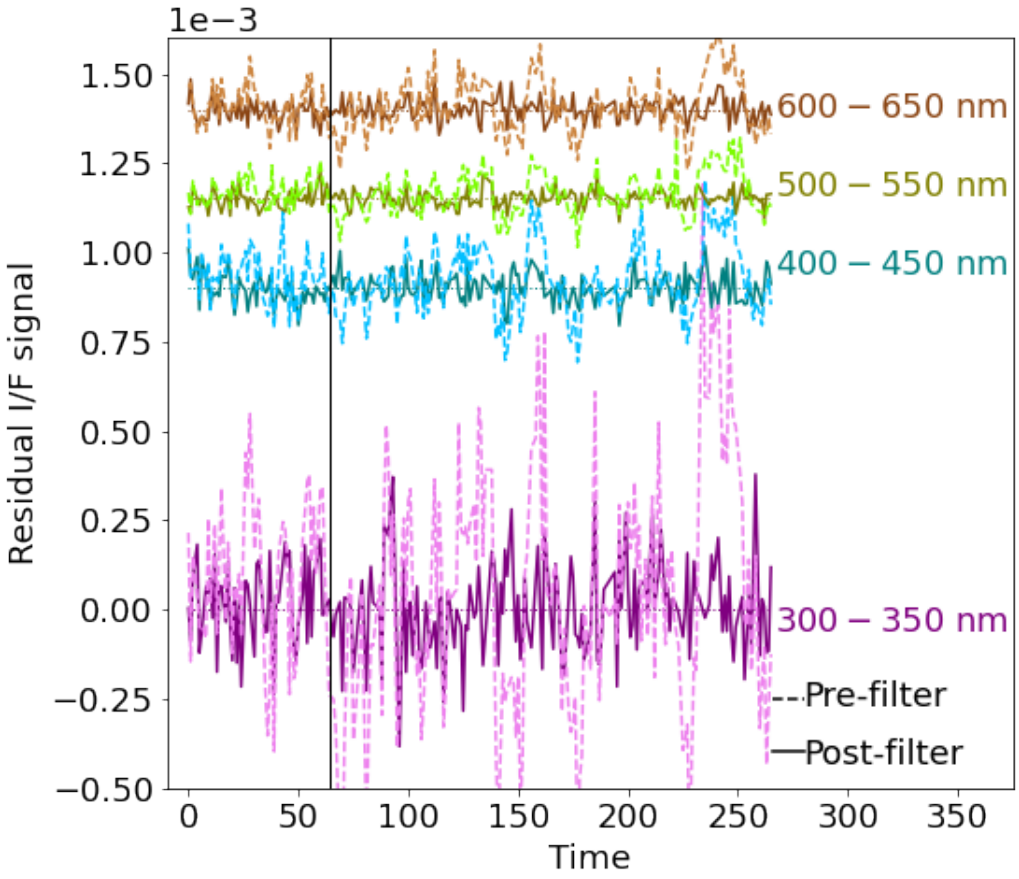

FIGURE A.8: Corrected signal (in solid) for the set "1987A", after spectral filtering has been applied to each wavelength range and the original spectrum(in dotted), plotted against time. An offset has been added here too to view each wavelength range distinctly.

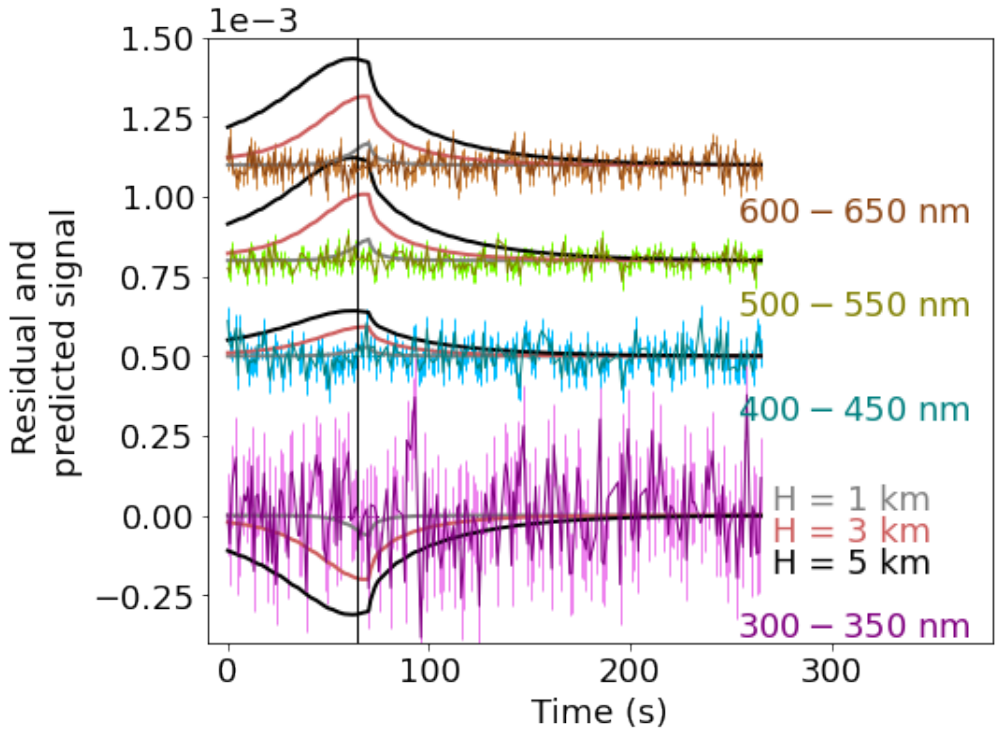

FIGURE A.9: This figure shows the filtered residual signal for "1987A" for each wavelength range. The signal predicted using the Fraunhofer model and the exponential density profile is plotted over the residual signal for a scale heights of 1, 3 and 5 km in grey,lightcoral and black respectively. An offset has been added to view the signals distinctly.

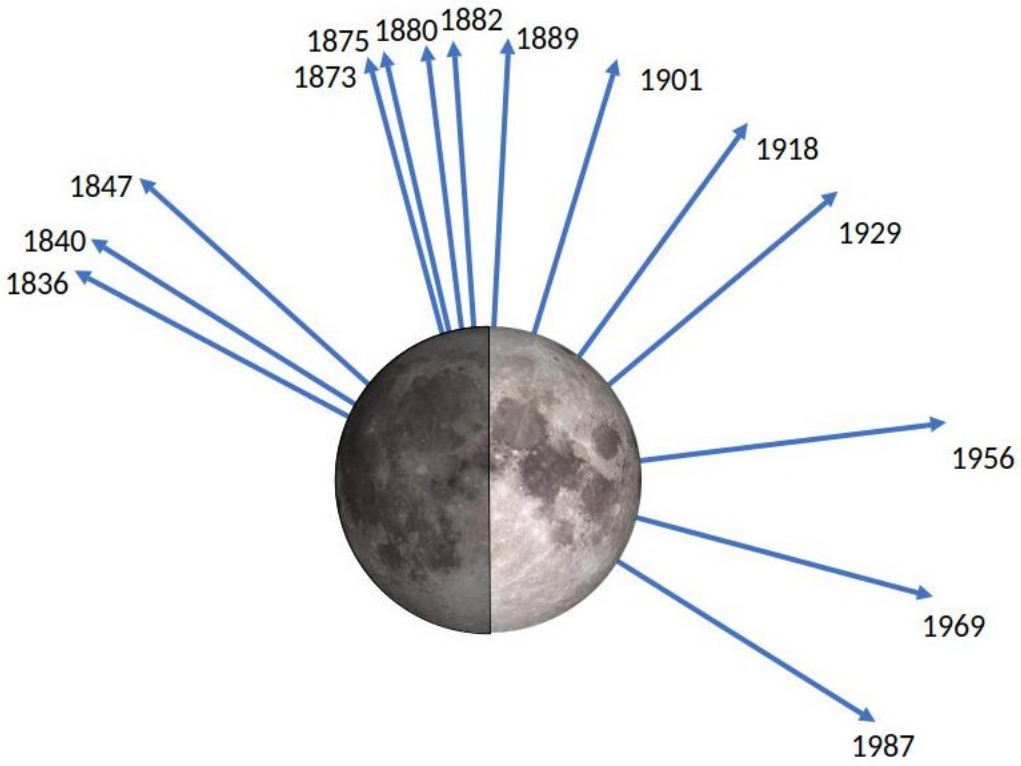

FIGURE A.10: This figure shows the location of Earth (arrows point to Earth) during the month of April 2014 while the Almost Limb activities were recorded by LADEE-UVS. It shows how the first observations are affected due to Earthshine of the dark side of the Moon while the last 5 observations have negligible amount of Earthshine.

Table A.2 shows the slope and intercept between the residual, $D_{i,est}(t)$ and predicted signal, $P_{i,est}(t)$ and the standard deviation of this slope and intercept are calculated for each wavelength range i. Weighted average of these slopes and intercepts using their respective standard deviation as weights is computed for each observation. The weighted averaged slope and intercepts with error bars at scale height of 1, 3 and 5 km are shown in this table. The intercept for this case is not reduced to zero. And the Earth-Moon position details during the course of these observations. The observed locations are farther and farther away from Earthshine horizon for the later data sets.

TABLE A.1: Observation geometry and fitted slopes for all Almost Limb activities

Activity name	H = 1 km	H = 3 km	H = 5 km	Days since Full Earth / New Moon	Difference between Sub-Earth and observed point	Earth-Moon Phase angle
	Slope	Slope	Slope			
1836A	-377.33 ± 61.20	-4.01 ± 0.28	-1.25 ± 0.05	1.72	52.89	20.6
1840A	-585.04 ± 60.39	-4.83 ± 0.33	-1.28 ± 0.08	2.72	48.05	32.6
1847A	-339.02 ± 29.87	-3.27 ± 0.22	-0.92 ± 0.05	3.72	38.59	44.6
1873A	-85.74 ± 13.06	-0.72 ± 0.09	-0.20 ± 0.02	5.72	6.20	68.6
1875A	-25.95 ± 10.67	-0.30 ± 0.11	-0.08 ± 0.36	6.72	3.55	80.6
1880A	-21.75 ± 12.05	-0.48 ± 0.11	-0.15 ± 0.03	6.72	-2.61	80.6
1882A	-84.67 ± 21.45	-0.59 ± 0.12	-0.14 ± 0.03	6.72	-4.36	80.6
1889A	12.72 ± 23.70	0.19 ± 0.13	0.05 ± 0.03	7.72	-12.25	92.6
1901A	-64.00 ± 32.74	-0.60 ± 0.18	-0.16 ± 0.04	8.72	-26.17	104.6
1918A	0.08 ± 0.34	0.03 ± 0.03	0.01 ± 0.01	10.72	-40.18	128.6
1929A	-0.09 ± 0.24	0.02 ± 0.02	0.01 ± 0.01	11.72	-53.23	140.6
1956A	0.02 ± 0.09	-0.01 ± 0.03	0.00 ± 0.02	14.72	-85.51	176.6
1969A	0.81 ± 0.12	0.00 ± 0.01	-0.01 ± 0.01	16.72	-107.27	200.6
1987A	0.20 ± 0.14	0.02 ± 0.02	0.01 ± 0.01	17.72	-124.76	212.6

TABLE A.2: Slopes and Intercepts for all Almost Limb activities

Activity name	H = 1 km		H = 3 km		H = 5 km		H = 1 km	H = 3 km	H = 5 km
	Slope	Intercept x10^{-5}	Slope	Intercept x10^{-5}	Slope	Intercept x10^{-5}	Slope	Slope	Slope
1836A	54.50 ± 35.94	-4.64 ± 0.13	0.59 ± 0.23	-4.83 ± 0.17	0.22 ± 0.08	-5.11 ± 0.25	-377.33 ± 61.20	-4.01 ± 0.28	-1.25 ± 0.05
1840A	225.74 ± 52.45	-4.41 ± 0.13	1.13 ± 0.29	-4.60 ± 0.17	0.34 ± 0.09	-4.88 ± 0.24	-585.04 ± 60.39	-4.83 ± 0.33	-1.28 ± 0.08
1847A	22.19 ± 27.64	-3.49 ± 0.13	0.46 ± 0.22	-3.72 ± 0.18	0.18 ± 0.08	-4.01 ± 0.29	-339.02 ± 29.87	-3.27 ± 0.22	-0.92 ± 0.05
1873A	-26.45 ± 20.21	-0.71 ± 0.25	-0.55 ± 0.45	0.02 ± 0.75	-0.30 ± 0.25	1.04 ± 1.50	-85.74 ± 13.06	-0.72 ± 0.09	-0.20 ± 0.02
1875A	20.93 ± 14.69	-0.78 ± 0.21	0.48 ± 0.36	-1.34 ± 0.59	0.27 ± 0.20	-2.12 ± 1.17	-25.95 ± 10.67	-0.30 ± 0.11	-0.08 ± 0.36
1880A	32.60 ± 14.82	-0.85 ± 0.18	0.61 ± 0.28	-1.44 ± 0.42	0.32 ± 0.15	-2.24 ± 0.81	-21.75 ± 12.05	-0.48 ± 0.11	-0.15 ± 0.03
1882A	-22.79 ± 27.10	-0.70 ± 0.20	-0.25 ± 0.35	-0.45 ± 0.46	-0.12 ± 0.17	-0.10 ± 0.89	-84.67 ± 21.45	-0.59 ± 0.12	-0.14 ± 0.03
1889A	-6.46 ± 26.50	0.23 ± 0.14	0.02 ± 0.25	0.24 ± 0.23	0.02 ± 0.10	0.24 ± 0.40	12.72 ± 23.70	0.19 ± 0.13	0.05 ± 0.03
1901A	-30.75 ± 34.97	-0.34 ± 0.13	-0.39 ± 0.23	-0.22 ± 0.15	-0.14 ± 0.07	-0.06 ± 0.22	-64.00 ± 32.74	-0.60 ± 0.18	-0.16 ± 0.04
1918A	-0.20 ± 0.40	0.18 ± 0.22	0.02 ± 0.05	0.02 ± 0.33	0.02 ± 0.04	-0.12 ± 0.53	0.08 ± 0.34	0.03 ± 0.03	0.01 ± 0.01
1929A	-0.42 ± 0.29	0.41 ± 0.24	-0.06 ± 0.05	0.59 ± 0.39	-0.05 ± 0.04	0.85 ± 0.7	-0.09 ± 0.24	0.02 ± 0.02	0.01 ± 0.01
1956A	0.07 ± 0.19	-0.26 ± 0.55	-0.07 ± 0.15	0.88 ± 2.70	-0.60 ± 0.39	16.1 ± 12.3	0.02 ± 0.09	-0.01 ± 0.03	0.00 ± 0.02
1969A	0.16 ± 0.16	-0.19 ± 0.24	0.03 ± 0.04	-0.37 ± 0.58	0.02 4± 0.05	-0.56 ± 1.33	0.81 ± 0.12	0.00 ± 0.01	-0.01 ± 0.01
1987A	0.13 ± 0.17	0.09 ± 0.20	0.01 ± 0.03	-0.14± 0.34	0.00 ± 0.03	0.23 ± 0.63	0.20 ± 0.14	0.02 ± 0.02	0.01 ± 0.01

APPENDIX B

Supplementary Information to Chapter 3: New Insights into Variations in Enceladus Plume Particle Launch Velocities from Cassini-VIMS spectral data

B.1 CUBES EXCLUDED FROM ANALYSIS

The following cubes were removed from the data on June 18th/Orbit no. 279:
CM_1876443559_1, CM_1876443614_1, CM_1876443669_1, CM_1876443724_1, CM_1876445164_1, CM_1876446029_1, CM_1876446202_1, CM_1876446375_1, CM_1876457449_1, CM_1876470103_1, CM_1876474082_1, CM_1876488640_1, CM_1876493658_1, CM_1876493831_1, CM_1876494004_1, CM_1876494177_1, CM_1876494350_1, CM_1876494523_1, CM_1876494696_1, CM_1876494869_1, CM_1876495042_1, CM_1876495215_1.

The following cubes are removed during background removal from the data on Aug 2nd/Orbit no. 286:
CM_1880355922_1, CM_1880358137_1, CM_1880366306_1, CM_1880369490_1, CM_1880380704_1, CM_1880390533_6, CM_1880391952_6, CM_1880392472_6, CM_1880392610_6, CM_1880392818_6, CM_1880392852_6, CM_1880393025_6, CM_1880393233_6, CM_1880393337_6, CM_1880393441_6, CM_1880393579_6, CM_1880393718_1, CM_1880394687_6, CM_1880394791_6, CM_1880395102_6, CM_1880395241_6, CM_1880395794_6, CM_1880395967_6, CM_1880396071_6.

The following cubes are removed during background removal from the data on Aug 28th/Orbit no. 290:
CM_1882608048_5, CM_1882637326_1, CM_1882640856_1, CM_1882644178_1, CM_1882644386_1, CM_1882645009_1, CM_1882646047_1, CM_1882646255_1, CM_1882646463_1, CM_1882646670_1, CM_1882646878_5.

APPENDIX C

Supplementary Information to Chapter 4: Noisy spectra to Particle properties: A machine learning analysis of Enceladus plume spectral data using VIMS observations

C.1 MACHINE LEARNING MODEL RESULTS

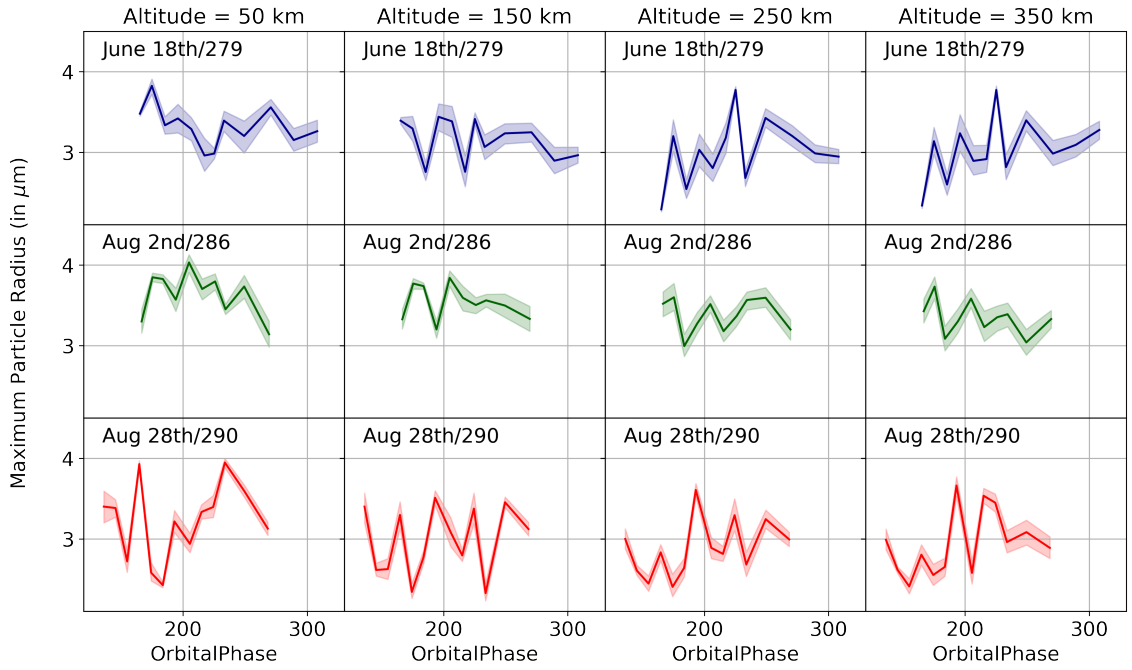

FIGURE C.1: This figure shows one of the outputs from the machine learning model: the maximum radius of value for a power law size distribution of plume particles. One the x-axis of each panel the orbital phase defines the position of Enceladus in its orbit around Saturn and the Y-axis shows the maximum particle radius. The altitude increases horizontally and the orbit no varies vertically.

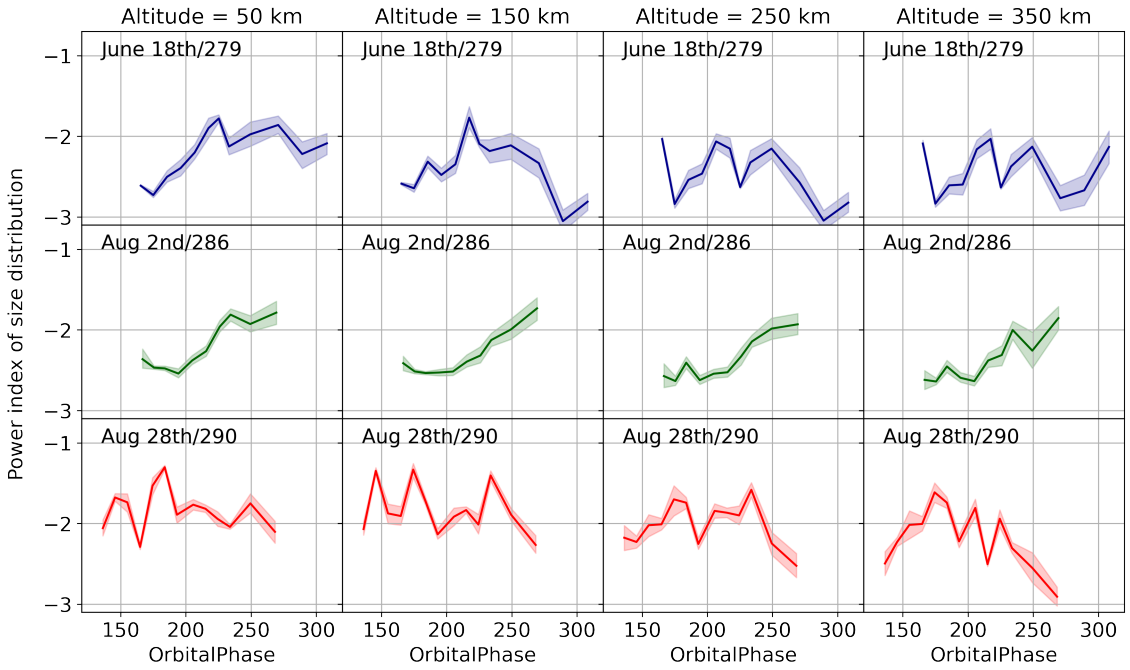

FIGURE C.2: The plots also shows an output of the machine learning model: power index of the power law size distribution for plume particles. Here we can see how the power index varies across orbital phase for different orbits and across altitude. The power law index appears to follow a very similar pattern to the average particle size variations discussed in Section 4.4.